Swansea University

A theoretical and empirical investigation into the growth of ultralong carbon nanotubes

by

Timothy Yick

A thesis submitted

in partial fulfilment for the degree

Doctor of Philosophy

Swansea, United Kingdom

September 2022

This page is intentionally left blank.

Table of contents

Table of Figures

List of tables

Abstract

Carbon nanotubes (CNTs) were first discovered and named as such by Iijima in 1991. Various institutes and researchers have since widely conducted ongoing research on carbon nanotube growth. The exceptional properties of CNTs, including their electrical and mechanical properties, aim to revolutionise the applications of electronics and devices in the future such as transmission power lines and lightweight high-strength carbon nanotube fibres. Therefore, understanding the mechanisms of growing ultra-long carbon nanotubes (UL-CNTs) that can increase the length to more than a centimetre long can unlock the full potential of the CNTs. This PhD project will have three parts:

(I) the growth experiments using different types of monometallic & bimetallic iron based catalysts for growing carbon nanotubes

(II) the computational simulation of flow fields around carbon nanotube geometry in a micro-scale

(III) the applications of carbon nanotubes produced from waste plastics, such as Ethernet & audio cables, and public engagement events about the research.

In the growth experiment topic, the primary objective of this research is to study the catalyst activities on the rate of carbon nanotube growth using monometallic (Fe) & bimetallic catalysts (Fe-Cu, Fe-Co, Fe-Ni, Fe-Sn, Fe-Ga, Fe-Mg & Fe-Al) dissolved in deionised water, and find which catalysts have the potential to grow the longest carbon nanotubes with improved characteristics, such as G/D (graphene/ disorders) ratio. As we know, the carbon source gas flow rate and reactor temperature profiles can affect the length of carbon nanotubes from the literature; an effective way to optimise experimental conditions to grow UL-CNTs is to use computational fluid dynamics (CFD) modelling methods. So far, there has been little research on the growth of ultra-long carbon nanotubes under a non-continuous flow environment on a nanoscale. Most computational modelling studies have only focused on the continuity of flow in a traditional approach. This research uses the BGK-Boltzmann equation and molecular collision models to investigate flow behaviours at the nanoscopic scale. Thus, this study provides an exciting opportunity to advance the knowledge of growing ultra-long carbon nanotubes (UL-CNTs) of centimetre length or higher and may be used in applications including the carbon nanotube Ethernet and audio cables as mentioned in this project.

Declarations and statements

This work has not been previously accepted in substance for any degree and is not being concurrently submitted in candidature for any degree.
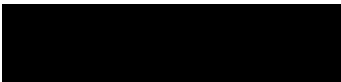
Signed: …█████████████████   (Candidate: Timothy Yick)

Date: …………………………
       5 May 2023

This thesis is the result of my own investigations, except where otherwise stated.

When correction services have been used, the extent and nature of the correction is

clearly marked in a footnote(s). Other sources are acknowledged by footnotes giving

explicit references. A bibliography is appended.

Signed: …█████████████████   (Candidate: Timothy Yick)

Date: …………………………
       5 May 2023

I hereby give consent for my thesis, if accepted, to be available for photocopying

and for inter-library loan and for the title and summary to be made available to

outside organisations.

Signed: █████████████████   (Candidate: Timothy Yick)

Date: …………………………
       5 May 2023

The University's ethical procedures have been followed and, where appropriate, that ethical

approval has been granted.

Signed: █████████████████   (Candidate: Timothy Yick)

Date: …………………………
       5 May 2023

Acknowledgements

Firstly, I would like to thank my primary supervisor, Dr. Alvin Orbaek White, for providing guidance and feedback on the carbon nanotube growth throughout this PhD project. I also thank my secondary supervisor, Dr. Ben Evans, for giving suggestions on various topics regarding molecular gas dynamics modelling on carbon nanotube geometry. Thanks also to the Energy Future Research group members, especially Dr. Varun Shenoy Gangoli and PhD student Thomas Mahy over the years. Little could be achieved without all your support.

I would also like to thank the team in the Advanced Imaging of Materials (AIM) facility at Swansea University for providing training and assistance on the operation of the Scanning Electron Microscopes (SEM). Thanks also for the support from the Welsh Government and the Energy Safety Research Institute (ESRI) for the funding. Most importantly, I want to thank my family and my friends for their support and encouragement when I was undertaking my research- particularly during the hard times of the COVID-19 pandemic over the past two years. My doctorate success wouldn't have been possible without your help.

Chapter 1

Introduction

1.1 The problem statements

Synthesis of ultra-long carbon nanotubes (UL-CNT) has become more prominent; carbon nanotubes' excellent mechanical, electrical, and thermal properties for future applications, such as electrical wires[1], which means that the length of CNTs is the primary consideration in design. However, producing carbon nanotubes that are more than a centimetre long (cm), let alone be kilometres long (km) for future applications, remains challenging. The chemical conditions for growing carbon nanotubes have been widely developed in three decades, for example: modifying the types of catalysts and changing the feeding gases. But understanding the physical parameters to grow ultra-long carbon nanotubes, namely, flow speed & gas dynamics, has become a new topic in the scientific community. The main idea of synthesising centimetre-long carbon nanotubes is to lift off the nanotube from the substrate along the gas flow direction and keep the catalyst active during the Chemical Vapour Deposition (CVD) process. There has been ongoing research to investigate the flow behaviours by molecular dynamics (MD) simulations, with this area of research completed in the computational field by A. Page[2]. Most such studies of carbon nanotube simulation have emphasised the continuum studies based on the Navier-Stokes equation's assumptions. Few research studies have focused on how the non-continuum individual gas molecular collisions affect carbon nanotubes at the atomic scale. The simulation in molecular dynamics and characterisation of ultra-long carbon nanotubes will be represented in this work. Both experimental and theoretical studies of carbon nanotube growth will be included here. It is expected that this combination of computational and theoretical research would bring a better understanding of how to grow centimetre-long carbon nanotubes reliably.

The simulation work of the carbon nanotube geometry is done using the dimensionless discontinuous finite element solution of the Boltzmann BGK equation by a high-performance computer (HPC). In terms of experimental studies, resonant Raman spectroscopy and scanning electron microscopy (SEM) used to investigate the characteristics of carbon nanotubes will be introduced in this work. Different catalyst types will be used for carbon nanotube growth, including monometallic and bimetallic iron-based catalysts. For the experiments, the gases are set to a low flow rate (30 sccm, standard cubic centimetres per minute) and compositions of

gases at a 2:1 ratio of H_2 (20 sccm)/ CH_4 (10 sccm) at 950 °C growth temperature. The following chapter will investigate the Fe, Fe-Cu, Fe-Co, Fe-Ni, Fe-Sn, Fe-Ga, Fe-Mg & Fe-Al catalysts with the activation energies. The final chapter discusses our carbon nanotube cables made from waste plastics and the presentations, impacts, and public engagement events promoting plastic wastes to carbon nanotubes project.

This work's novelty is centred on using a water-based solvent for catalyst dispersion prior to the growth of UL-CNTs. Previously, hydrocarbon solvents were more commonly used as they are both carbon-rich (beneficial to CNT nucleation) and good solvents for typical catalyst salts. However, in using a hydrocarbon solvent, we noted the vast spreading of the solvent on the growth surfaces; although beneficial from the perspective of driving homogeneous distribution of catalysts, it is challenging when correlating catalyst salt to the concentration of CNTs. The water-based solvent, with greater surface tension, made counting CNTs and the correlation of catalyst: CNTs more readily achievable; this methodology can lend itself towards the quantification of catalytic performance of a slew of transition metal catalysts. Moreover, this method can significantly assist with a greater understanding of catalytic performance for the growth of UL-CNTs.

1.2   Experimental studies on the growth of ultralong single-walled carbon nanotubes

The definition of an ultra-long carbon nanotube (UL-CNT) is that the length of the carbon nanotube is more than a centimetre in length[3]. The UL-CNTs are usually grown on a flat Si/ SiO_2 substrate. The catalyst solution is doped at the leading edge of a silicon wafer, with the individual carbon nanotube growth horizontally aligned from the location of the catalyst and parallel to the gas flow (figure 1.1). In figure 1.2, the catalyst is the large lump piece at the centre of the image. The fine lines on top are the individual carbon nanotubes captured by scanning electron microscopy and the figure caption at 12,000x magnification and a working distance (WD) of ~5 mm and 1 kV operating voltage on a JEOL 7800 FE-SEM (JEOL Ltd., Tokyo, Japan).
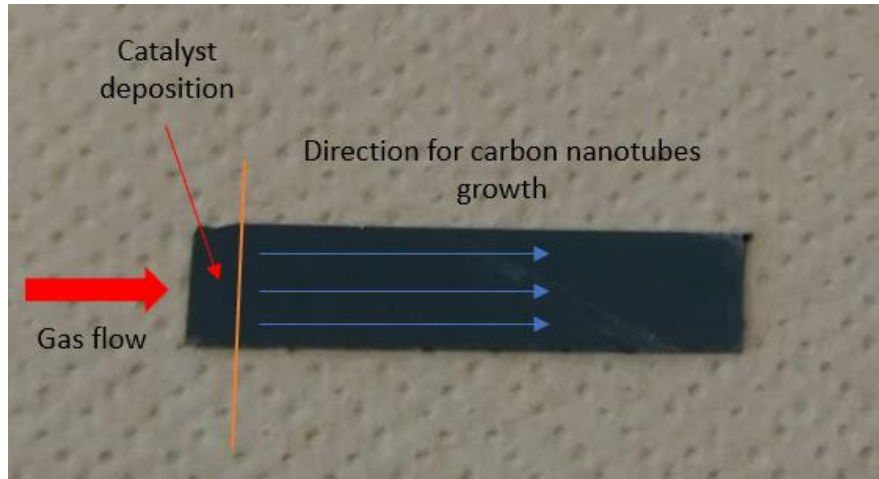
Figure 1.1. Illustration on how carbon nanotubes (CNTs) grow on a silicon substrate.
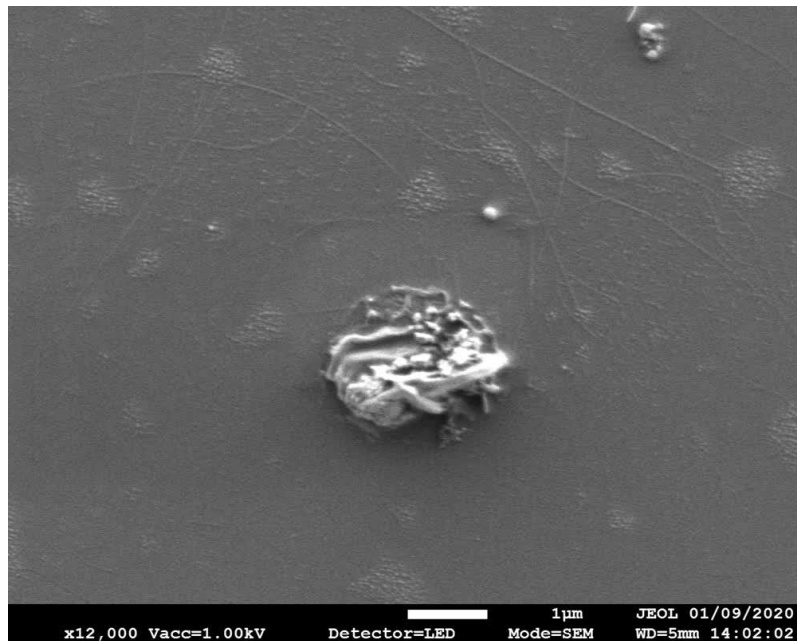
Figure 1.2. Ultra-long carbon nanotubes (UL-CNTs) grown on Si/ SiO2 wafer, captured by scanning electron microscopy.

The growth of UL-CNTs is commonly known to be caused by the temperature differences between the gas flow and the substrates from which the CNT originates. This temperature difference creates a buoyancy force, lifting the tube above the substrate surface in what is known as a "kite mechanism", and the carbon nanotube grows continuously until the termination of the growth either by the deactivation of the catalyst or collision of catalyst particle with the substrate and collapse under its weight in tip growth. The diagram below illustrates typical base growth of a carbon nanotube whereby the catalyst on the base catches

16

the carbon atoms and forms a CNT (figure 1.3). This work describes the methodology of ultra-long carbon nanotubes (UL-CNTs)[4].
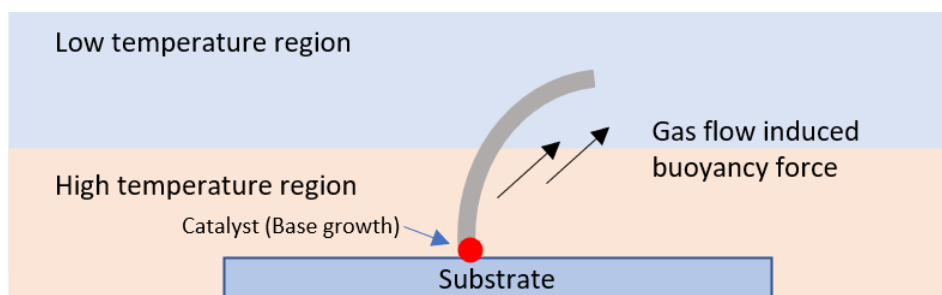
Figure 1.3. Diagram on how carbon nanotubes grown on silicon substrate by buoyancy effect in the real experimental case

Fei Wei's group reported the longest continuous ultra-long carbon nanotube ever made in 2013[5], which conveys a half-meter-long (55 cm) individual carbon nanotube understood by using the Schulz-Flory distribution – a mathematical model calculated by the probability of catalyst activity to grow polymers. The paper outlined the probability of successful long carbon nanotube growth based on the temperature, water content, hydrogen to methane (H_2/CH_4) ratio, and gas flow rates. These parameters can act as reference conditions for ultra-long carbon nanotube growth. (The Japanese Group)

1.2.1 Brief history of carbon nanotubes from discovery to applications, markets and challenges

Before the discovery of carbon nanotubes in 1991, only four allotropes of carbon were known to the scientific community: diamond, fullerene (C_{60} buckyball), graphite and non-crystalline (amorphous) carbon. Sumio Iijima first identified multi-walled carbon nanotubes (MWCNTs) in 1991[6], whereby a needle-like structure was observed using a high-resolution transmission electron microscope (TEM). In 1993, single-walled carbon nanotubes (SWCNTs) were imaged by Iijima and IBM independently[7]. Carbon nanotubes are commonly used for composite materials, microelectronics, energy storage, and other applications in various different industries, including automotive, biomedical, aerospace, defence sector etc[8]. The microelectronics applications for carbon nanotubes are especially promising for the future. Due to their excellent current capacity and thermal conductivity, CNTs may replace silicon for the next generation of semiconductor electronics[9]. Other applications include touch screens and

solar panels where the carbon nanotubes may replace the indium tin oxide (ITO) for touch screens[10]. Carbon nanotube solar panels in photovoltaics applications can also generate high power conversion efficiencies[11]. According to data from Market and Markets in 2018[12], the carbon nanotube market is growing gradually from USD 4.55 billion in 2018 by 0.98 % each year and is predicted to reach USD 9.84 billion by 2023.

The technical challenges associated with the successful synthesis of ultra-long carbon nanotubes (UL-CNTs) centre around the need to keep the catalyst active throughout the entire growth process. The longest individual carbon nanotubes grown was half a meter long by Fei Wei[3]. In his paper, the successful ultra-long carbon nanotubes depend on growth temperature, water content, H_2/CH_4 ratio & gas velocity. In the longest ultra-long carbon nanotube forests, the bundles have achieved an average length of 14 cm[13], with a growth lifetime of 26 hours and an average growth rate of 1.5 μm/s. Their method has easily scaled up the production of carbon nanotubes. The demand for carbon nanotubes' length and quantity is currently in the research phase. The UL-CNTs are grown on a silicon substrate for most UL-CNT growth experiments. The fabrication, removal, and collecting of carbon nanotubes from the silicon wafer is challenging because the individual carbon nanotubes are tiny and hard to handle. The obstacle of producing identical lengths, chirality, and diameter of carbon nanotubes to maximise electrical conductivity is also a demanding situation in the experimental work. There are no precisely laid-out parameters in the field of ultra-long carbon nanotube growth.

1.2.2   How are carbon nanotubes made and characterised?

The synthesis of CNTs has been improved over the years from laser ablation to chemical vapour deposition (CVD). The CVD process is the most common method now for producing high-quality carbon nanotubes in large quantities, especially for the growth of ultra-long single-walled carbon nanotubes (UL-SWCNTs)[14]. The CVD method for producing carbon nanotubes involves the formation of five or six carbon member rings into CNT structure on a growth substrate with a catalyst film, with an inert gas flow carrying the carbon source as well as the eventual carbon nanotubes growing along the flow direction as shown in figure 1.3, with the steps including (I) decomposition of the carbonaceous gas molecule, (II) diffusion of the carbon atom on the catalyst, (III) precipitation of carbon atoms into CNT. Figure 1.4 illustrates an example CVD growth method for producing ultra-long carbon nanotubes (UL-CNTs). Here, the silicon substrate is where the carbon nanotube grows, and the heating zone provides thermal

energy to the quartz tube. The silicon is heated up by radiation and convection. The gas inlet intakes the reacting gases and exhausts out the other side. The influencing factors for the carbon nanotube growth can be gases, growth temperature, flow speed and catalyst, all of which will be discussed.
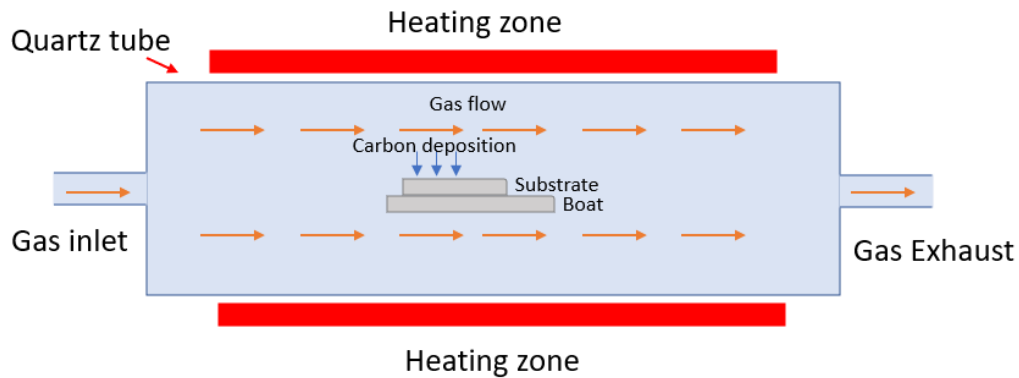
Figure 1.4. Chemical Vapour Deposition (CVD) diagram for ultra-long carbon nanotubes (UL-CNTs) growth.

1.3   Growth mechanisms of carbon nanotubes

The growth of carbon nanotubes includes two mechanisms which depend on where the catalyst particle is located: (I) tip growth and (II) base growth[4]. Tip growth is where the catalyst is attached to the furthest end of the carbon nanotube from the substrate. Base growth is where the catalyst is anchored to the substrate, with carbon atoms precipitating outwards to form the nanotube. Tip growth involves the catalyst particle being lifted from the substrate surface. Still, the CNT remaining on it, and thus tip growth is more favourable for UL-CNT growth in terms of removing any substrate influence, as depictured in figure 1.5. The support material for the substrate is usually made of quartz, silicon, alumina or graphite[15].
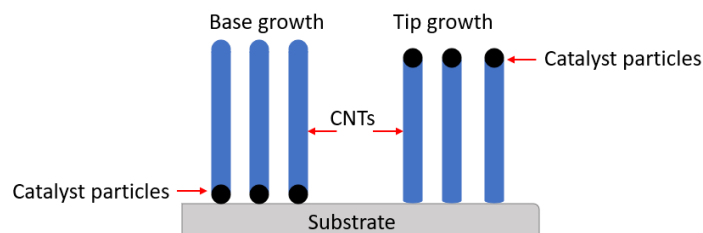
Figure 1.5. Tip growth & base growth mechanisms of carbon nanotube growth.

1.3.1 Feeding gas composition

The carrier gases play a significant role in providing the carbon source to the catalyst sites and forming carbon nanotubes (CNTs). The composition of these gases and operating flow condition helps optimise the CNT growth during the CVD process. For example, the length, diameter, density, and chirality of the CNT can be influenced by the feed gases[16]. The combination of gases for UL-CNTs growth usually consists of (I) a noble gas, (II) a carbon-rich gas, and (III) a reducing gas. In this work, helium (He), methane (CH_4) & hydrogen (H_2) were used for ultra-long carbon nanotube synthesis. The role of helium in carbon nanotube formation is to help with thermal convection, keep the catalysts clean, and remove any contamination out of the quartz tube, while the purpose of hydrogen is to prevent catalyst oxide formation during the precipitation phase of CNT growth. Methane is the carbon source chosen here to form the carbon nanotubes. Previous work conducted has found that hydrogen improves the CNT structure quality[16]. Methane was selected in this work due to its thermodynamic stability[17]; it is stable at operational conditions where other hydrocarbons, such as ethylene, would have cracked and therefore ensures the stability of carbon nanotube grown under continuous gas flow. In other published literature, nitrogen (N_2) and ethylene (C_2H_4) have also been commonly used for carbon nanotube growth, and researchers have also developed different efficient ways for carbon nanotube synthesis with the HiPCO® process being one such example of using higher pressure carbon monoxide (CO)[18].

1.3.2 Operating temperature

As per the Arrhenius reaction in physical chemistry, the operating temperature helps provide the activation energy to the catalyst. The temperature is usually from 500 °C to 1100 °C for carbon nanotube growth, which depends on the types of feedstock gases and catalysts[19]. The optimum temperature reported for the CH_4/ H_2 and iron (III) chloride catalyst for UL-CNT growth performed in this experiment is 950 °C[20, 21]. This defines the activation state of the catalyst in addition to the CNT growth rate, diameter, and density. It was reported that the temperature effects would affect the carbon nanotubes' growth behaviours and the catalysts' activation and carbon deposition from the gases. Some catalysts may trigger require a lower temperature requirement for CNT growth activation; for example, copper (Cu) has a typical activation temperature of 700 °C[22]. The methane (CH_4) cracking temperature is at around 1,200 °C[23].

1.3.3 Flow rate

There are two mechanisms for aligning the UL-CNTs during growth: (I) high gas flow speed and (II) a low gas flow speed for orientating ultra-long growing carbon nanotubes driven by the flow and the buoyancy force. Fast heating under high gas flow rates (> 1000 sccm)[24] and the buoyant effect at low flow sccm (from roughly as low as 1.5 sccm to as high as 500 sccm)[3, 25] due to the temperature differences between the substrate and the wider gas domain (mixture of hydrogen and methane) inside the quartz tube. There remains debate on which mechanism is more prevalent for the synthesis of UL-CNTs, be it fast heating that causes the convection of the gas flow and the carbon nanotubes to flow around it until it is long enough to fall under its weight to the surface and terminate on the substrate, or low flow rate causing a buoyancy force by the temperature differences between the substrate and gas flow.

1.3.4 Catalyst types

The catalysts provide active sites for initialising carbon nanotube growth and increase the chemical reaction rate. Transition metals such as nickel (Ni), iron (Fe), and cobalt (Co) are commonly used metallic catalysts for carbon nanotube growth[26]. The catalyst particles allow the diffusion of the carbon into the molten catalyst phase and act as a cluster for carbon nanotube growth. Based on their types and concentration to facilitate carbon nanotube growth, bimetallic catalysts have also been developed, which will be discussed later in this work. Also, the metallic catalysts usually are present as compounds, for example, iron compounds, including iron chloride and ferrocene, rather than pure iron (which forms iron oxides) to avoid any oxidation state during the CVD process[27]. The metallic compounds have low electronegativity, which avoid attracting electrons toward themselves, which is opposite to pure metallic elements.

1.3.5 Why are carbon nanotubes used?

Carbon nanotubes are lightweight, have extraordinary thermal, mechanical, and electrical properties, and are expected to become a significant material in the future[28]. The tensile strength of carbon nanotubes at ~375 times stronger than steel (see table 1.1)[29], which has been suggested to be a potential material for a space elevator[30]. Other applications of carbon nanotubes include electric shock resistors for NASA's Juno spacecraft mission and Vantablack, among the darkest materials in the world[30, 31]. Pure metallic carbon nanotubes can have an

electric current density of 4×10^9 A/cm^2 [32], which is more than 1000 times greater than copper. The electrical conductivity of carbon nanotubes depends on their chirality angle (n, m), which will further be explained in chapter 2, but suffice it to say there remain a lot of current and future applications for CNTs.

Table 1.1. Tensile strength of steel, Single-walled carbon nanotubes (SWCNTs) & Multiple-walled carbon nanotubes (MWCNTs)

Materials	Young's modulus (GPa)	Tensile Strength (GPa)
Steel	208	0.4
Single-walled carbon nanotubes (SWCNTs)	1054	150
Multiple-walled carbon nanotubes (MWCNTs)	1200	150

1.4   Raman spectroscopy on carbon nanotubes

Raman spectra help identify carbon nanotubes and also give important information on the chirality and any defects of the carbon nanotubes. Raman spectroscopy uses the laser scattering light of the interaction with photons vibration, which happens when materials resonate with a laser beam and provides information on vibration mode to identify the individual molecule structure and chemical bonding, which provides unique identification of the molecules. There are two modes of Raman scattering: Stokes scattering and anti-Stokes scattering[33], Stokes scattering occurs when the emitted radiation is lower than the energy state of incident radiation and whilst anti-Stokes scattering occurs when increasing in photon energy. The effect of Raman spectroscopy was established in 1928 and was named after the discoverer, C.V. Raman [34]. The model of Raman spectroscopy used in this project is Renishaw inVia TM ® Raman spectroscopy (Renishaw plc, Pontyclun, UK) with five available lasers of wavelength 457 nm, 488 nm, 535 nm, 633 nm, and 785 nm.

Figure 1.6. Renishaw inVia^{TM} Raman spectroscopy

1.5   Chirality of SWCNTs

The purity & disorder of the carbon nanotubes (CNTs) is dependent on the intensity of G/ D (Graphene/ Deflect) ratio shown from the Raman spectrum. The G band presents in most of the graphene-like materials by the planar vibrations of carbon atoms, and D band found from the structural defects[35]. The highest G peak with lowest D peak indicates the best quality of carbon nanotubes. The forms of carbon present in G peak and D peak would typically be the sp^2 structure. For example, graphite and fullerenes present with both G and D peaks, whilst the sp^3 structure diamond will predominantly have the D peak presented. The radial breathing mode (RBM) is a unique observation of single walled carbon nanotubes (SWCNTs) in the Raman spectrum[36]. Check the tangential mode (G-band, graphene band, ~1590 cm^{-1}), disorder mode (D-band, defects-induced band, ~1350 cm^{-1}) with a 2D-band occurring at 2600 – 2800 cm^{-1}, and radial breathing modes (RBM, 100 – 350 cm^{-1}) only for SWCNTs. Different lasers with alternating focus lens provide different size of laser spots. The 20x objective lens was used here to observe the characteristics of carbon nanotubes in this project, since it provides a good balance of signal intensity and acquisition area. This provides a laser spot size of 1.0 µm with the 633 nm laser and 1.3 µm with the 785 nm laser (table 1.2).

Table 1.2. Laser spot size with different laser settings as per the instrument manual from Renishaw plc[37]

	Spot size			
	5 x	20 x	50 x	100 x
633 nm	6.4 μm	1.9 μm	1.0 μm	0.9 μm
785 nm	-	-	1.3 μm	-

1.6 Single-walled carbon nanotube (SWCNTs)

Single-walled carbon nanotubes (SWCNTs) consist of one layer of carbon atoms formed in a cylindrical shape. These have an average diameter of approximately 1 nm[38], which is smaller than a typical multi-walled carbon nanotube (MWCNT) at 5 – 20 nm in diameter. SWCNTs are generated to have more promising properties than multi-walled carbon nanotubes (MWCNTs)[39]. The SEM image in figure 1.7 is that of a SWCNT sample from NoPo Nanotechnologies[40]. The technical sheet from the NoPo Ltd company stated that the single-walled carbon nanotubes (SWCNTs) contents are >80 wt %. From figure 1.7, it shown that a large proportion of multi-walled carbon nanotubes (MWCNTs) (> 100 nm) presented and a few of SWCNTs (~1 nm) at the location. The rule of thumb of growing SWCNTs is that the size of catalyst particle has to be on the order of 1 nm diameter, since this is the contact face of cylindrical nanotube diameter. Therefore, a more lower catalyst concentration can help produce
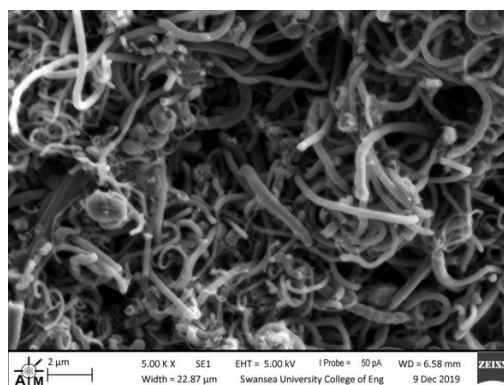
Figure 1.7. SEM image of single-walled carbon nanotubes (SWCNTs) from NoPo Nanotechnologies. The image was captured at a working distance of 6.58 mm, operating voltage of 5 kV, probe current of 50 pA, and 5,000x magnification using an EVO LS 25 SEM (Carl Zeiss AG, Oberkochen, Germany).

a smaller catalyst particle for SWCNT growth and will be discussed in the next chapter, which in this work can be achieved by dilution of the catalyst precursor solution. It must also be noted that the RBM mode observed with one laser, say 633 nm, need not occur at the same Raman shift location for another laser setting such as 785 nm, as these are unique resonance frequencies of individual carbon nanotube as a function of their diameters[41].
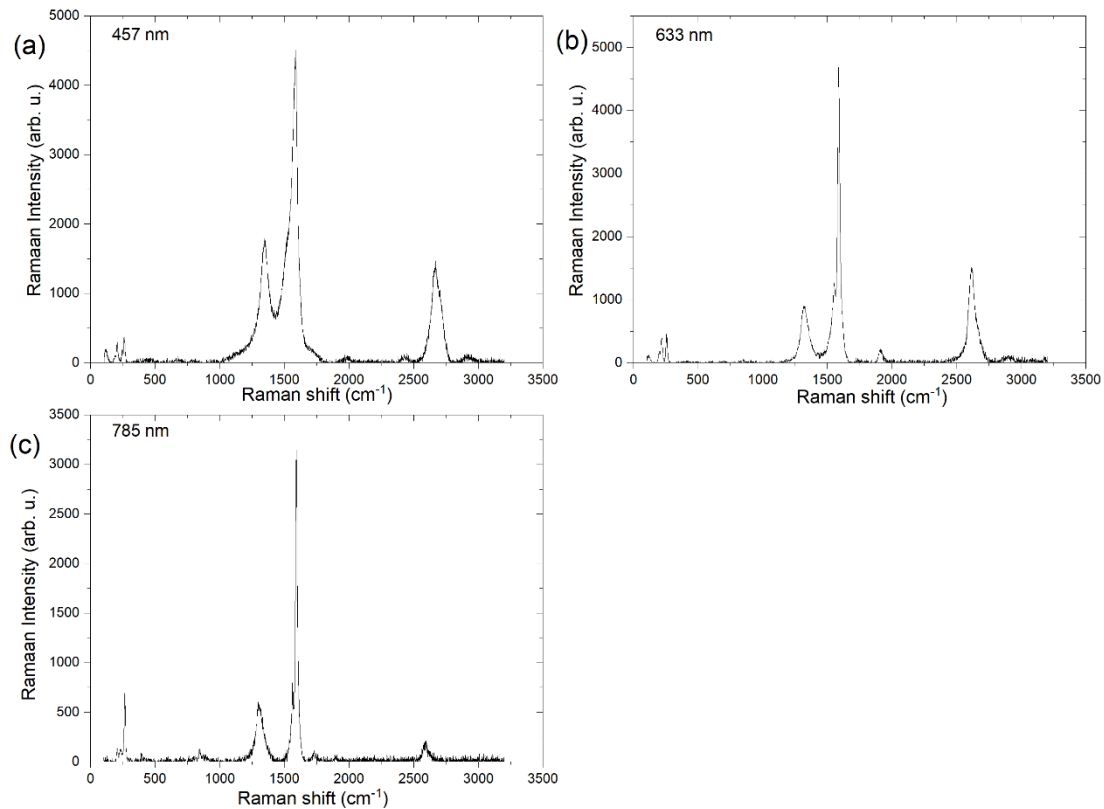
Figure 1.8. Representative Raman spectrum of G-band, D-band & RBM modes at (a) 457 nm, (b) 633 nm & (c) 785 nm wavelength laser for NoPo SWCNT sample

The illustration of these changes is presented in the Raman spectrum for one of the NoPo SWCNT samples (figure 1.8), whereby the RBMs range from 100-350 cm^{-1}. For this sample, (a) the RBM mode was confirmed at 207 cm^{-1} and 260 cm^{-1} by using a 457 nm wavelength laser with 1% laser power setting. Figure 1.8 b shows another RBM peak at 264 cm^{-1} as seen using the 633 nm wavelength laser with 5% power and 1.8 c helps identify RBM peaks at 216 cm^{-1} and 255 cm^{-1} using the 785 nm laser at 5% power. The G-band and D-band were found at 1300 cm^{-1} and 1600 cm^{-1} respectively in both cases with different spectrum

intensities, and the G/D ratio is ~ 5. The intensity of G/D ratio presents the defects present on carbon nanotube structure proportion of graphitic carbon (sp^2 hybridised) to sp^3 hybridised carbon present as impurities and defects. In addition, a slight silicon peak was observed at 520 cm^{-1} Raman shift. To observe a clear RBM mode within the spectrum and reduce the noise signal, the measurements were taken with two accumulations for each acquisition, and the exposure time was set to 15 seconds.

The map acquisition is also a useful function in the Renishaw inVia TM ® that is used to image and collect spectra for larger areas of the sample beyond what is possible under a single spot size area. Firstly, the laser spot was moved to a corner of silicon wafer and set as the origin (0,0) for x, y coordinates. The movement of laser scanning can be chosen as a line, rectangle, zigzag etc, and the number of scanning points can be selected in the Renishaw WiRE software program. Some impurities may be captured in the spectra, which were formed due to the inconsistent chemical reaction during the CVD process. The iron (III) chloride might change to other forms of iron due to oxidation including iron carbide (cementite, Fe_3C) and iron oxide (magnetite, Fe_3O_4). These can show up in the RBM regions too given they have peaks at 120 cm^{-1} and 223 cm^{-1} respectively[42]. For the observation of individual SWCNTs, a fixed laser spot was chosen and moved along the wafer length until a clear signal intensity is observed. Due to the inconsistent focal length as it pertains to samples on the wafer, baseline removal was applied for the spectrum in the software based on the Gaussian mathematic modal.

1.6.1   Introduction and application of the Kataura plot for SWCNTs

The Kataura plot was initially designed by a Japanese scientist, Hiromichi Kataura, in 1999 for a visualization of Raman scattering data into a theoretical graph [43], and provides users with a rapid identification of SWCNT characteristic. The Kataura plot is a chart that reflects the interaction of energy separation (eV) and Raman shift (cm^{-1}), and can determine an individual carbon nanotube diameter down to the Angstrom. SWCNT diameters can range from 0.6 - 5 nm [44], and the Kataura plot can identify the range from 0.6 nm to ~ 2 nm. The chirality (zigzag, armchair, or chiral) configuration helps determine the semiconducting and metallic properties of these nanotubes and is the arrangement of regular hexagonal lattice orientation on the nanotube. For the Raman scattering below (figure 1.9), the red dots represent metallic CNTs and black dots are showing semiconducting CNTs, which in turn are identified by their

chirality (n, m) and diameter. The steps of calculating the diameter of the CNTs are shown below.
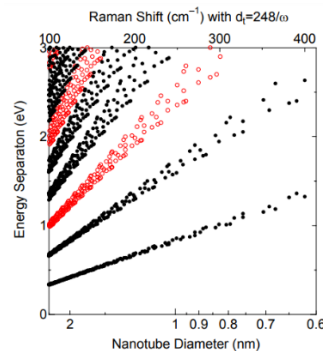
Figure 1.9. Kataura plot for Single-walled carbon nanotubes (SWCNTs) [45]

1) Y axis - The energy separation (eV) = laser power from nm to eV

2) Upper X axis - Raman Shift (cm^{-1}) = This is the radial breathing mode (RBM)) observed from the Raman spectroscopy with $d_t = \frac{248}{\omega}$ (ω is the Raman shift in the RBM mode)

3) Lower X axis – Carbon nanotube diameter (nm) from 0.6 nm to ~2 nm

In terms of the CNT sample, to find its diameter of single-walled carbon nanotube (SWCNT) and chirality (n, m):

1) The RBM mode of Raman shift for 633 nm laser from the Raman spectrum (in figure 1.8)

2) The usual laser setting converted from nanometre (nm) to electron volt (eV) for 5 different laser settings (round up to 2 decimal places)

Table 1.3. The energy (eV) and wavelength (nm) conversion

Wavelength (nm)	Energy (eV)
457	2.71
488	2.54
514	2.41
633	1.96
785	1.58

The energy (eV) and wavelength (nm) conversion from the equation:

$$E = \frac{hc}{\lambda} \qquad (1)$$

E = Energy (eV)

h = Planck's constant = 6.6261 x 10^{-34} (J·s)

c = speed of light = 299,792,458 (m/s)

λ = wavelength (nm)

1.7 Scanning electron microscopy (SEM) of carbon nanotubes

Scanning Electron Microscope (SEM) provides high resolution magnified images by detecting the electrons emitted from the electron gun that are reflected off the surface of a specimen[46]. The imaging process is done under vacuum conditions to ensure the electron beam path length is constant (7 mm working distance). The beams are generated from the electron gun and pass through a series of focus lens, then the electron beam interacts and scan through the surface of a sample in a raster pattern. There are two types of electrons generated from the specimen, backscattered electrons (BSEs) & secondary electrons (SEs)[47]. The secondary electrons (SEs) are the main source of information that provide the surface details of samples, and the lower electron detector (LED) in the SEM will be used for carbon nanotubes imaging. The magnification of a typical SEM can go up to 300,000 times the original image[48], which is much larger to that from an example optical microscope at only ~300x[49].

Figure 1.10. Field Emission Scanning Electron Microscopy (FE-SEM) on JEOL 7800F.

There are two SEMs available for use at the Advance Imaging of Materials Core Facility (AIM), Swansea University – (1) Zeiss EVO LS25 (Carl Zeiss AG, Oberkochen, Germany) & (2) JEOL JSM-7800F (JEOL Ltd., Tokyo, Japan). Higher resolution imaging of isolated carbon nanotubes at low magnification is the aim of this project, so both the SEMs were used initially to determine which one gives the best results. The SEM image acquired below (figure 1.11) from the Zeiss EVO LS25 at 60x magnification, 1 kV, 150 pA, and 6.9 mm working distance appeared to have lower resolution than the one with the same conditions settings on the JEOL SEM. Further testing revealed the best conditions for SWCNT imaging
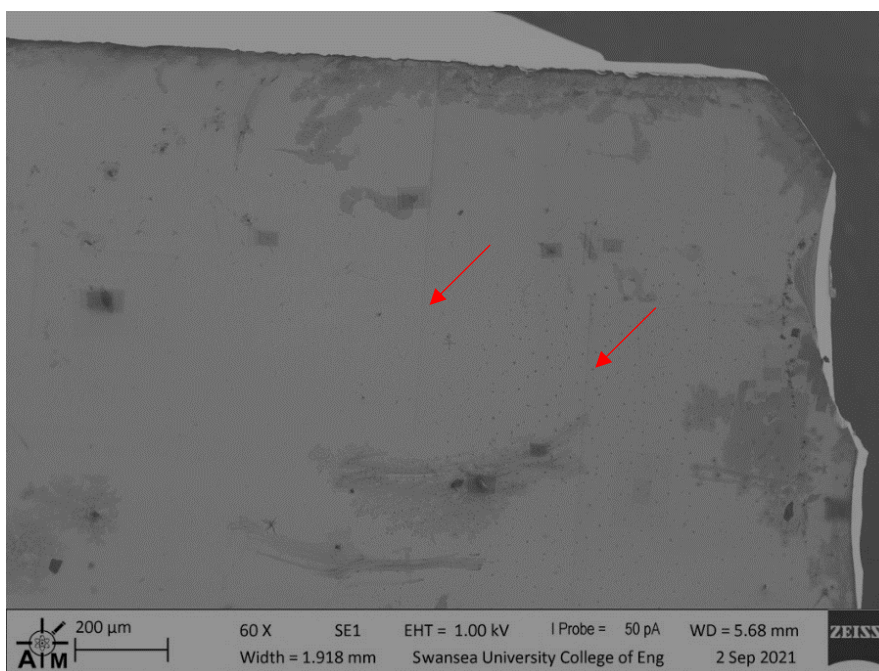
Figure 1.11. SEM image at 60x magnification from EVO LS25 SEM includes the imaging conditions

with the JEOL are at 100x magnification, 1 kV, 150 pA, and 7 mm working distance, as seen in figure 1.12 below. The SEM image captured by the EVO appeared "softer", and the carbon nanotubes are less sharp/contrasting relative to the background. The individual carbon nanotubes extending from the leading edge appeared faded on the silicon surface. As such, most of the stacked UL-CNTs images were captured by the JEOL SEM. This distinction between the two microscopes can be explained by their different configurations, in particular the configuration of the electron guns where the EVO uses a changeable Tungsten/ LaB_6 (Lanthanum hexaboride) thermionic emission gun and the JEOL is a Field emission SEM (FE-

SEM)[50] which consists of a tip made of tungsten wire crystal with high voltage applied. The JEOL SEM also adopts a Schottky emitter whereby the electron gun filament is heated at a lower temperature[51]. The LaB_6 gun on the other hand is operated via thermal energy applied on the surface and the Schottky emitter is made from tungsten at the emission tip by smaller areas of emission and provider higher image quality at a lower magnification. The field emission guns provide a smaller spot size than the thermionic gun. This spreads the energy in a smaller area and the coherency is higher. Therefore, at low magnification (~100x) the UL-CNTs are best viewed by the JEOL SEM.

The SEM used for general CNT imaging is the JEOL 7800F accordingly. Sample preparation is an essential step for SEM processing as it can clean the sample by removing any contamination on the surface. Firstly, the carbon nanotube sample on silicon wafer is placed on an aluminium stage (22 mm diameter). The dust-free sample is then be transferred to a larger brass adapter and the 22 mm diameter copper pin stubs are tightened by a setscrew. For the last step of sample preparation, the dust-free stage with the sample was placed inside the SEM using a loading rod, and the chamber was pumped out to evacuate air and result in a vacuum environment. The liquid nitrogen cooling system prevents the tungsten wire filament from building up heat.
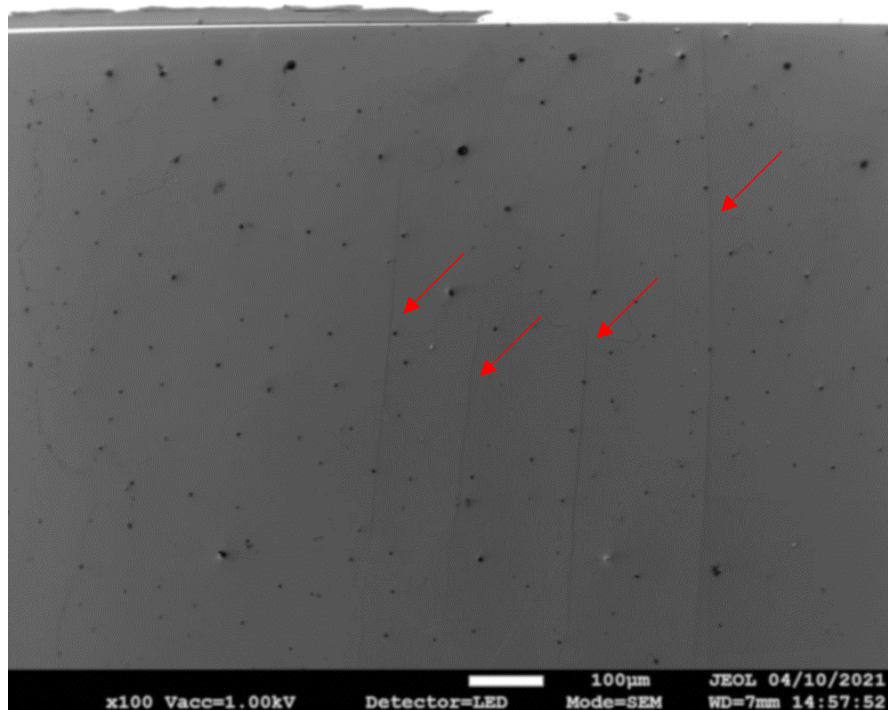
Figure 1.12. SEM image at 100x magnification from JEOL 7800F SEM includes the imaging conditions

The pressure inside the chamber should be kept below 9.6x10^{-5} Pa to ensure good vacuum conditions. The samples z-height is set to 11.9 mm as the clearance is 40 mm, and the working distance (WD) was set to 7 mm from the electron gun to the sample following which the sample was raised to the desired height. There are four basic functions in the JEOL SEM: stigmatism, focus, aperture, and contrast. Aperture alignment is used when the image is moving, while the stigmatism control is to minimise image distortion. Choosing higher magnification, noise, scan speed (fast scan), and a 2360 x 1280 image resolution provides a detailed structure image of the carbon nanotubes. The wobble function is to reduce the scanning area and given a faster scan on the image to correct the image. There are various scanning speeds (1-12) which can be chosen and a faster scan will introduce noise whereas a slower scan speed with lower noise is optimum.

There are four types of settings by varying the scan speed & line average. The "Quick 1" setting was used during the large area imaging at low magnification to find notable features in the beginning, as well as to correct for stigmatism and wobble. The fine default settings can be changed to Scan 1 averaging 12 and was found to be the best setting for SWCNT imaging. The faster scan speed with more noise signal can be compensated for by slow line scanning to give a clear carbon nanotube image [52]. The working distance (WD) has to be set so it is not too close to the back scatter detector (BSD) located on the pole-piece. There is a balance of good contrast and high probe current with working distance. If the probe current is high (~250 pA), there might be build-up of hydrocarbons which will compromise the signal. The lower electron detector (LED) mode was used for most general settings with a scan speed of 10-11 which is equivalent to 10-100 μs. For general SEM imaging at both low and high magnification, the Fine 2 setting was found to work best.

Table 1.4. Default settings of scanning speed/ line average of Jeol SEM 7800F[53]

Settings	Scan speed/ line average
Quick 1	Scan 1 averaging 4
Quick 2	Scan 1 averaging 32
Fine 1	Scan 4 averaging 4
Fine 2	Scan 10 averaging 1

The appearance of a square in the SEM images. It appears when going from higher to lower magnification whereby a layer of hydrocarbons is deposited on the surface and a set of

square boxes is seen. This can be avoided by lowering the probe current with an increased scan time to minimise the effects further. Considering the available time, the settings were set to 10 to find an area to adjust the stigmatism and then focus at high magnification, with the total time spent at any given area to not exceed 15 minutes (figure 1.13).
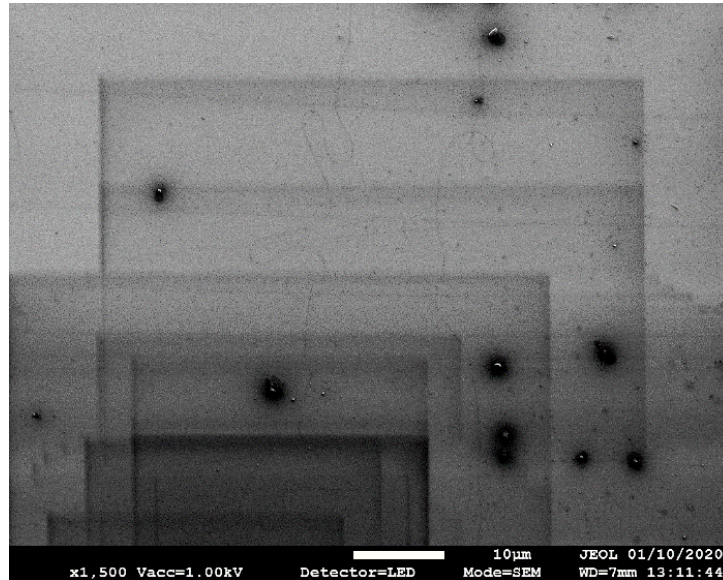
Figure 1.13. Hydrocarbon (black boxes) build-up from the SEM imaging

1.7.1   The use of N-type and P-type silicon wafer for SEM imaging

Silicon wafers are used as the substrate for carbon nanotube growth and for SEM imaging as the background. Due to the nature of the background and its semiconducting characteristic for SEM imaging of carbon nanotubes, the image quality by using N-type silicon is preferred over P-type silicon. P-type silicon wafers are heavily doped with boron or gallium and N-type using phosphorus, with the latter having an extra electron in the outer shell which allows for electric current flow though the silicon substrate compared to the other way round with P-type silicon. There are three relevant effects after the electron beam strikes the sample-1) emitting back-scattered electrons, 2) positive charges of secondary electrons, 3) electron absorption by the sample resulting in a negative charge accumulation in the meteoroid. Since there is no extra positive charge accumulated in the sample, the N-type with a negative charge is ideal for SEM imaging. Therefore, the samples were prepared using N-type silicon wafers[54].

1.7.2 General SEM conditions for carbon nanotube image capturing

The ideal SEM imaging condition is that the quality of electrons (backscatter & secondary electrons) emitted by the specimen are equal to the number of incident electrons with no charging occurring. The charging states are varied from different materials, especially for some less conductive specimens which require a much lower voltage mode, given the fact that the secondary electron emission coefficient is inversely proportional to the accelerating voltage. Thus, choosing the correct accelerating voltage (kV) in the SEM settings is important for image acquisition. In this exercise, the investigation of how both different operational voltage (5 kV, 15 kV, 25 kV & 30 kV) and increasing the z-height of the stage (distance from pole piece to specimen) could compensate the intensity of the electron beam to the secondary electron detector would affect the image quality. All SEM images were captured at the same conditions of 1000x magnification, 1000 pA probe current, scan speed was set at 11 (approximately 100 µs dwell time), and working distance (WD) to 7 – 8 mm. In figure 1.14, the SEM image captured at 5 kV (a) gives the best depth of field, which the z-height was set at 11.9 mm. From 15 kV (b) to 25 kV (c), the depth profiles start compromise by the intense electrons, and some coarse and grainy features were observed on the image. For the last image captured at 30 kV (d), the incident signal reduces by increasing the working distance (WD) to 16 mm. The SEM image becomes brighter due to increasing signal. In conclusion, the incident signal (kV) can be reduced while also increasing the z-height. In the general SEM imaging, at high magnification (> 10,000x), it is usually set at 5 kV and working distance (WD) at 7 mm, as shown in figure 1.15.
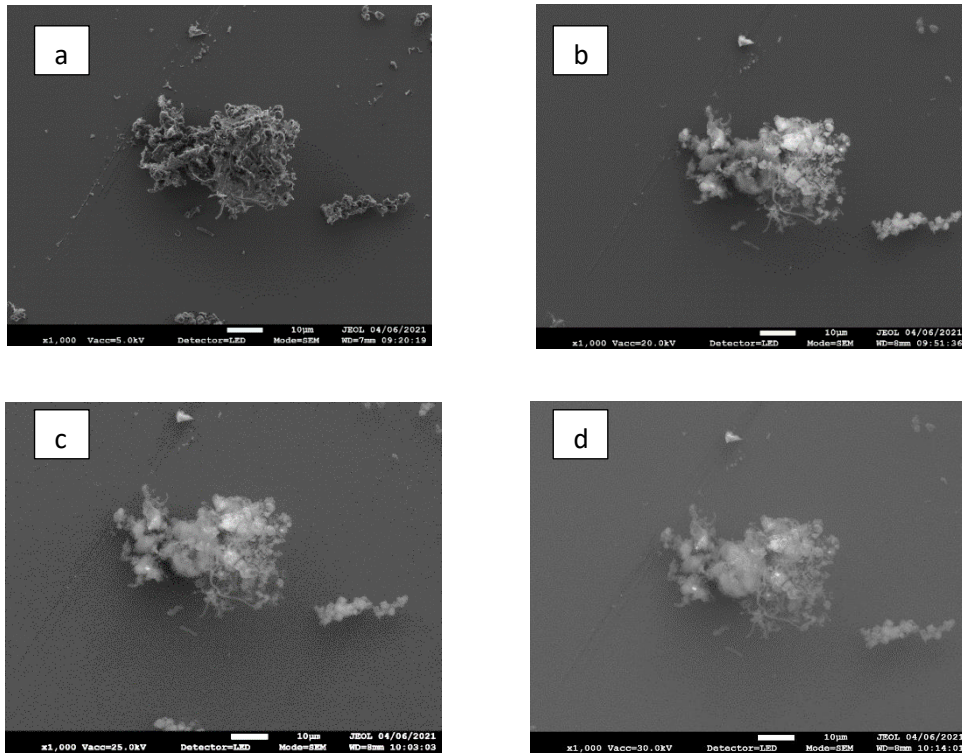
Figure 1.14. Different conditions of the carbon nanotubes in the SEM – (a) 5 kV, (b) 20 kV, (c) 25 kV, (d) 30 kV.
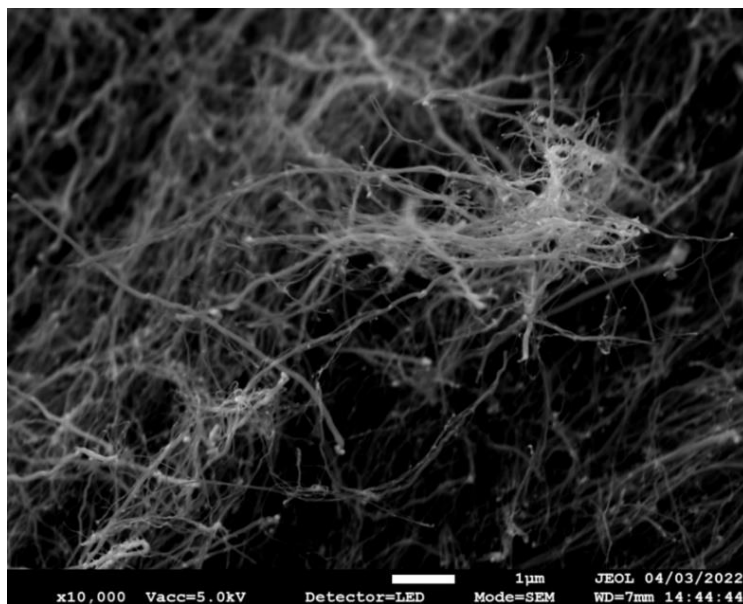
Figure 1.15. Carbon nanotube bundles at high (10,000x) magnification

1.7.3 Technique of Individual carbon nanotube capture at low magnification

For most of the imaging done, the detection of secondary electrons and lower electron mode (LED) is used which provided more surface details than the secondary electron mode

(SE). The low voltage (<5 kV) can result in complications pertaining to the detection and characterization of individual and embedded single walled carbon nanotubes by scanning electron microscopy. An isolated carbon nanotube requires shorter dwell time, and ensembles are set to a longer scan time and averaged for better signal-to-noise ratios at a low acceleration voltage such as 1 kV. The best dwell time for capturing isolated carbon nanotube was reported at 100 μs[55], which is closely matched to our settings (scan speed 11, ~ 100 μs) in the JEOL SEM for individual carbon nanotube capturing. The isolated carbon nanotube set at this level appeared brighter in the image, however, the negative aspect for this would result in decrease in signal-to-noise ratio. To enhance the quality of SEM image by the negative effect of shorter dwell times, ideally the line integration is used for inclusive imaging. Since the absence of line integration in the settings, frame integration was used in alterative. The difference between the line and frame integration is the integration average either by lines or in the entire surface.
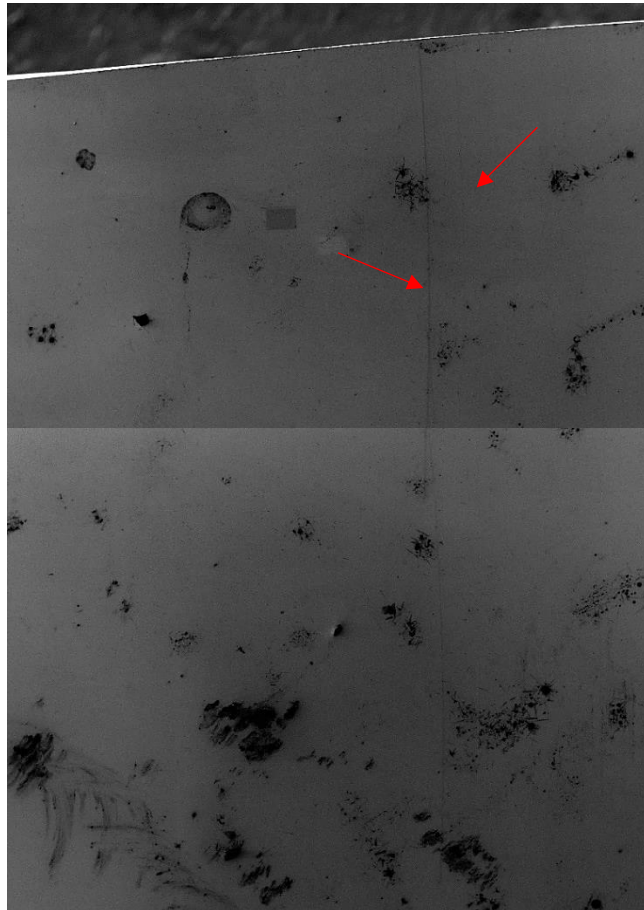
Figure 1.16. Stitched carbon nanotube images using 1kV accelerated voltage

1.8 Conclusion

Carbon nanotubes (CNTs) have many exciting current and potential future applications, and there is a growing market for CNTs globally. Ultralong CNTs are a must to achieve these applications, and the rest of this document discusses various theoretical and experimental work done to optimize the growth of UL-CNTs, characterise them, and even discuss devices made out of CNTs such as CNT cables that where then used for public engagement exercises. This chapter has explored the identification tools used to characterise the CNTs including Raman spectroscopy in conjunction with the Kataura plot to identify the diameter of single-walled carbon nanotubes (SWCNTs). The various techniques of using scanning electron microscopy to image isolated CNTs at low magnification and bundles of CNTs at high magnification was also discussed, with parameters involving varying the operational voltage, z-height, and probe current to improve the image quality.

1.9 References

(1) Lekawa-Raus, A.; Kurzepa, L.; Peng, X.; Koziol, K. Towards the development of carbon nanotube based wires. *Carbon* **2014**, *68*, 597-609.

(2) Page, A. J.; Chandrakumar, K.; Wang, Y.; Irle, S.; Morokuma, K. Mechanisms of single-walled carbon nanotube nucleation, growth and chirality-control: Insights from QM/MD simulations. In *Electronic Properties of Carbon Nanotubes*, IntechOpen, 2011.

(3) Hong, B. H.; Lee, J. Y.; Beetz, T.; Zhu, Y.; Kim, P.; Kim, K. S. Quasi-continuous growth of ultralong carbon nanotube arrays. *Journal of the American Chemical Society* **2005**, *127* (44), 15336-15337.

(4) Zhang, R.; Zhang, Y.; Wei, F. Controlled synthesis of ultralong carbon nanotubes with perfect structures and extraordinary properties. *Accounts of chemical research* **2017**, *50* (2), 179-189.

(5) Zhang, R.; Zhang, Y.; Zhang, Q.; Xie, H.; Qian, W.; Wei, F. Growth of half-meter long carbon nanotubes based on Schulz–Flory distribution. *Acs Nano* **2013**, *7* (7), 6156-6161.

(6) Iijima, S. Helical microtubules of graphitic carbon. *nature* **1991**, *354* (6348), 56-58.

(7) Iijima, S.; Ichihashi, T. Single-shell carbon nanotubes of 1-nm diameter. *nature* **1993**, *363* (6430), 603-605.

(8) Gohardani, O.; Elola, M. C.; Elizetxea, C. Potential and prospective implementation of carbon nanotubes on next generation aircraft and space vehicles: A review of current and expected applications in aerospace sciences. *Progress in Aerospace Sciences* **2014**, *70*, 42-68.

(9) Franklin, A. D. The road to carbon nanotube transistors. *Nature* **2013**, *498* (7455), 443-444.

(10) Gangoli, V. S.; Godwin, M. A.; Reddy, G.; Bradley, R. K.; Barron, A. R. The state of HiPco single-walled carbon nanotubes in 2019. *C* **2019**, *5* (4), 65.

(11) Wieland, L.; Li, H.; Rust, C.; Chen, J.; Flavel, B. S. Carbon nanotubes for photovoltaics: From lab to industry. *Advanced Energy Materials* **2021**, *11* (3), 2002880.

(12) Markets, M. a. Global Carbon Nanotubes (CNT) Market by Type (Single Walled & Multi Walled), End-Use Industry (Electronics & Semiconductors, Chemical Materials & Polymers, Structural Composites, Energy & Storage, Medical), Method, and Region - Forecast to 2026. *Markets and Markets* **2021**.

(13) Sugime, H.; Sato, T.; Nakagawa, R.; Hayashi, T.; Inoue, Y.; Noda, S. Ultra-long carbon nanotube forest via in situ supplements of iron and aluminum vapor sources. Carbon 2021, 172, 772-780.

(14) Ago, H.; Imamura, S.; Okazaki, T.; Saito, T.; Yumura, M.; Tsuji, M. CVD growth of single-walled carbon nanotubes with narrow diameter distribution over Fe/MgO catalyst and their fluorescence spectroscopy. *The Journal of Physical Chemistry B* **2005**, *109* (20), 10035-10041.

(15) Azam, M. A.; Zulkapli, N. N.; Nawi, Z. M.; Azren, N. M. Systematic review of catalyst nanoparticles synthesized by solution process: towards efficient carbon nanotube growth. *Journal of Sol-Gel Science and Technology* **2015**, *73* (2), 484-500.

(16) Cheung, C. L.; Kurtz, A.; Park, H.; Lieber, C. M. Diameter-controlled synthesis of carbon nanotubes. *The Journal of Physical Chemistry B* **2002**, *106* (10), 2429-2433.

(17) Sharma, A. K.; Sharma, R.; Chaudhary, U. Hydrogen-acetylene gas ratio and catalyst thickness effect on the growth of uniform layer of carbon nanotubes. *Fullerenes, Nanotubes and Carbon Nanostructures* **2017**, *25* (7), 397-403. Behr, M. J.; Gaulding, E. A.; Mkhoyan, K. A.; Aydil, E. S. Effect of hydrogen on catalyst nanoparticles in carbon nanotube growth. *Journal of Applied Physics* **2010**, *108* (5), 053303.

(18) Jourdain, V.; Bichara, C. Current understanding of the growth of carbon nanotubes in catalytic chemical vapour deposition. *Carbon* **2013**, *58*, 2-39.

(19) Cinke, M.; Li, J.; Chen, B.; Cassell, A.; Delzeit, L.; Han, J.; Meyyappan, M. Pore structure of raw and purified HiPco single-walled carbon nanotubes. *Chemical Physics Letters* **2002**, *365* (1-2), 69-74.

(20) Lee, C. J.; Park, J.; Kim, J. M.; Huh, Y.; Lee, J. Y.; No, K. S. Low-temperature growth of carbon nanotubes by thermal chemical vapor deposition using Pd, Cr, and Pt as co-catalyst.

Chemical physics letters **2000**, *327* (5-6), 277-283. Lee, Y. T.; Park, J.; Choi, Y. S.; Ryu, H.; Lee, H. J. Temperature-dependent growth of vertically aligned carbon nanotubes in the range 800− 1100 C. *The Journal of Physical Chemistry B* **2002**, *106* (31), 7614-7618.

(20) Huynh, T. M.; Nguyen, S.; Nguyen, N. T. K.; Nguyen, H. M.; Do, N. U. P.; Nguyen, D. C.; Nguyen, L. H.; Nguyen, C. V. Effects of Catalyst Pretreatment on Carbon Nanotube Synthesis from Methane Using Thin Stainless-Steel Foil as Catalyst by Chemical Vapor Deposition Method. *Nanomaterials* **2020**, *11* (1), 50.

(21) Orbaek, A. W.; Barron, A. R. Towards a 'catalyst activity map'regarding the nucleation and growth of single walled carbon nanotubes. *Journal of Experimental Nanoscience* **2015**, *10* (1), 66-76.

(22) Fiedler, H.; Hermann, S.; Schulz, S. E.; Gessner, T. Influence of copper on the catalytic carbon nanotube growth process. In *2011 IEEE International Interconnect Technology Conference*, 2011; IEEE: pp 1-3.

(23) Guizani, C.; Sanz, F. J. E.; Salvador, S. The nature of the deposited carbon at methane cracking over a nickel loaded wood-char. *Comptes Rendus Chimie* **2016**, *19* (4), 423-432.

(24) Huang, S.; Maynor, B.; Cai, X.; Liu, J. Ultralong, Well-Aligned Single-Walled Carbon Nanotube Architectureson Surfaces. *Advanced Materials* **2003**, *15* (19), 1651-1655.

(25) Jin, Z.; Chu, H.; Wang, J.; Hong, J.; Tan, W.; Li, Y. Ultralow feeding gas flow guiding growth of large-scale horizontally aligned single-walled carbon nanotube arrays. *Nano letters* **2007**, *7* (7), 2073-2079.

(26) Jo, S.-I.; Jeong, G.-H. Single-Walled Carbon Nanotube Synthesis Yield Variation in a Horizontal Chemical Vapor Deposition Reactor. *Nanomaterials* **2021**, *11* (12), 3293. Homma, Y.; Kobayashi, Y.; Ogino, T.; Takagi, D.; Ito, R.; Jung, Y. J.; Ajayan, P. M. Role of transition metal catalysts in single-walled carbon nanotube growth in chemical vapor deposition. *The Journal of Physical Chemistry B* **2003**, *107* (44), 12161-12164.

(27) Sato, H.; Hori, Y.; Hata, K.; Seko, K.; Nakahara, H.; Saito, Y. Effect of catalyst oxidation on the growth of carbon nanotubes by thermal chemical vapor deposition. *Journal of applied physics* **2006**, *100* (10), 104321.

(28) Popov, V. N. Carbon nanotubes: properties and application. *Materials Science and Engineering: R: Reports* **2004**, *43* (3), 61-102.

(29) Pugno, N. M. On the strength of the carbon nanotube-based space elevator cable: from nanomechanics to megamechanics. *Journal of Physics: Condensed Matter* **2006**, *18* (33), S1971.

(30) Samareh, J. A.; Siochi, E. J. Systems analysis of carbon nanotubes: opportunities and challenges for space applications. *Nanotechnology* **2017**, *28* (37), 372001.

(31) Patil, A. VANTABLACK: The World's Darkest Material. *Man-Made Textiles in India* **2015**, *43* (1).

(32) Wei, B.; Vajtai, R.; Ajayan, P. Reliability and current carrying capacity of carbon nanotubes. *Applied physics letters* **2001**, *79* (8), 1172-1174.

(33) Krafft, C.; Dietzek, B.; Popp, J.; Schmitt, M. Raman and coherent anti-Stokes Raman scattering microspectroscopy for biomedical applications. *Journal of biomedical optics* **2012**, *17* (4), 040801.

(34) Singh, R. CV Raman and the Discovery of the Raman Effect. *Physics in Perspective* **2002**, *4* (4), 399-420.

(35) Eklund, P.; Holden, J.; Jishi, R. Vibrational modes of carbon nanotubes; spectroscopy and theory. *Carbon* **1995**, *33* (7), 959-972.

(36) Liu, K.; Wang, W.; Wu, M.; Xiao, F.; Hong, X.; Aloni, S.; Bai, X.; Wang, E.; Wang, F. Intrinsic radial breathing oscillation in suspended single-walled carbon nanotubes. *Physical Review B* **2011**, *83* (11), 113404.

(37) Renishaw. TM051 – Laser spot size & mapping. *Spectroscopy Products Division, Renishaw plc* **2019**.

(38) Zorbas, V.; Ortiz-Acevedo, A.; Dalton, A. B.; Yoshida, M. M.; Dieckmann, G. R.; Draper, R. K.; Baughman, R. H.; Jose-Yacaman, M.; Musselman, I. H. Preparation and characterization of individual peptide-wrapped single-walled carbon nanotubes. *Journal of the American Chemical Society* **2004**, *126* (23), 7222-7227.

(39) Ganesh, E. Single walled and multi walled carbon nanotube structure, synthesis and applications. *International Journal of Innovative Technology and Exploring Engineering* **2013**, *2* (4), 311-320.

(40) NoPo. *HiPCO® Single Walled Carbon Nanotube (1Gram)*. 2022. https://nopo.in/web/product/nopo-hipco/ (accessed 16/5/2022).

(41) Dresselhaus, M. S.; Dresselhaus, G.; Saito, R.; Jorio, A. Raman spectroscopy of carbon nanotubes. *Physics reports* **2005**, *409* (2), 47-99.

(42) Wei, Y.; Luo, D.; Zhang, C.; Liu, J.; He, Y.; Wen, X.; Yang, Y.; Li, Y. Precursor controlled synthesis of graphene oxide supported iron catalysts for Fischer–Tropsch synthesis. *Catalysis Science & Technology* **2018**, *8* (11), 2883-2893. Gunawardana, B.; Singhal, N.; Swedlund, P. Dechlorination of pentachlorophenol by zero valent iron and bimetals: effect of surface

characteristics and bimetal preparation procedure. In *Proceedings of the Annual International Conference on Soils, Sediments, Water and Energy*, 2012; Vol. 17, p 8.

(43) Costa, S.; Borowiak-Palen, E.; Kruszynska, M.; Bachmatiuk, A.; Kalenczuk, R. Characterization of carbon nanotubes by Raman spectroscopy. *Materials Science-Poland* **2008**, *26* (2), 433-441.

(44) Jorio, A.; Araujo, P. T.; Doorn, S. K.; Maruyama, S.; Chacham, H.; Pimenta, M. A. The Kataura plot over broad energy and diameter ranges. *physica status solidi (b)* **2006**, *243* (13), 3117-3121.

(45) Kataura-Plot for Resonant Raman, Photon.t.u. Available at: http://www.photon.t.u-tokyo.ac.jp/~maruyama/kataura/kataura.html (Accessed: April 16, 2023).

(46) Mohammed, A.; Abdullah, A. Scanning electron microscopy (SEM): A review. In *Proceedings of the 2018 International Conference on Hydraulics and Pneumatics—HERVEX, Băile Govora, Romania*, 2018; pp 7-9.

(47) Robinson, V. Electron detectors used for imaging in the scanning electron microscope. *Scanning Electron Microscopy* **1984**, *3* (1), 19.

(48) Afanasyev, S.; Kychkina, T.; Savvinova, L. Scanning electron microscope (advantages and disadvantages). In *Colloquium-journal*, 2019; Голопристанський міськрайонний центр зайнятості: pp 25-27.

(49) Chen, X.; Zheng, B.; Liu, H. Optical and digital microscopic imaging techniques and applications in pathology. *Analytical Cellular Pathology* **2011**, *34* (1-2), 5-18.

(50) ZEISS. *ZEISS EVO Scanning Electron Microscope*. 2022. https://www.zeiss.com/microscopy/int/products/scanning-electron-microscopes/evo.html (accessed 16/5/2022).

(51) Jeol. *JSM-7800F Schottky Field Emission Scanning Electron Microscope*. 2022. https://www.jeol.co.jp/en/products/detail/JSM-7800F.html (accessed 16/5/2022).

(52) NanoScience Instruments, *SEM Source Comparison*. 2022. https://www.nanoscience.com/products/scanning-electron-microscopes/sem-source-comparison/ (accessed 16/5/2022).

(53) Jeol. *A Guide to Scanning Microscope Observation*. 2022. https://www.jeol.co.jp/en/applications/pdf/sm/844_en.pdf (accessed 20/5/2022).

(54) Universitywafer. *P-Type Silicon Wafers All Diameters for Research & Production*. 2022. https://www.universitywafer.com/p-type-silicon.html (accessed 16/5/2022).

(55) Orbaek, A. W.; Barron, A. R. Complications pertaining to the detection and characterization of individual and embedded single walled carbon nanotubes by scanning electron microscopy. *Nanoscale* **2013**, *5* (7), 2790-2797.

Chapter 2

Physical growth of Ultra-long Carbon Nanotubes (UL-CNTs)

2.1   Introduction of physical growth of Ultra-long Carbon Nanotubes (UL-CNTs)

An automated control of gas flow was carried out using Mass Flow Controllers (MFCs) for carbon nanotube growth by Chemical Vapour Deposition (CVD). The experimental setup has been developed in the laboratory and will be discussed in this chapter. The system consists of a commercial Raspberry Pi 400 computer controlling the gas flow rate (sccm) by regulating the MFCs and duration of growth, or growth length (min) of the chemical reactions. All the reactions were performed at 950 °C degrees under a mixture of hydrogen (H_2, 20 sccm) and methane (CH_4, 10 sccm) with iron (III) chloride ($FeCl_3$) catalyst, wherein the catalyst was dispersed from a 1 mmol concentration using water solvent. Catalyst samples of $FeCl_3$ control were compared against bi-metallic samples of Fe-Cu, Fe-Ni, Fe-Co, Fe-Sn, Fe-Ga, Fe-Al & Fe-Mg using metal chloride salts in equimolar concentrations. Resulting products were characterised using Scanning Electron Microscopy (SEM) and Raman spectroscopy for each catalyst sample in order to count the number of carbon nanotubes and the length of the CNTs. The longest carbon nanotubes were observed at 1.32 cm (Fe control sample). It was found that the iron monometallic catalyst (Fe) is optimum for the carbon nanotubes growth than the other types of iron based bimetallic catalysts. The results of the longest carbon nanotubes are Fe (1.32 cm in length), Fe-Cu (0.85 cm in length), Fe-Co (0.7 cm in length), Fe-Ni (0.6 cm in length), Fe-Mg (0.29 cm in length) & Fe-Al (0.13 cm in length). The statistical analysis by box plots for CNT length & G/D ratio Raman spectroscopy will be investigated in this study.

2.2   Setup for Chemical Vapour Deposition (CVD) automated desktop using Raspberry Pi microcontroller

For the reliability and reproducibility of the carbon nanotubes growth, a consistent Chemical Vapour Deposition (CVD) system is often required. However, such programmable system may demand expensive installation and maintenance costs. An affordable control system for CNT growth was developed by J. Ahn[1], and the system is controlled by a LabVIEW software for carbon nanotubes growth experiments. For our setup in the laboratory, the Raspberry Pi 400 microcontroller was chosen for controlling the flow rates of the relevant gasses. Given the fact that the Raspberry Pi is simply programmed with a Python language,

low cost, and various interfaces are available (HDMI, USB, Ethernet, Wi-Fi, Bluetooth and GPIOs etc.). The hardware expansions offer the potential for some useful applications, for example: the thermometer for temperature monitoring and moisture meter – which is found that water is attributed to the growth activity[2] and for the real-time monitoring from remote locations. The primary equipment for growing the carbon nanotubes is a hot-walled Chemical Vapour Deposition (CVD) furnace model EST-1200 (Carbolite Gero, Sheffield, UK) in figure 2.1. The quartz tube and silicon substrates are heated by conduction, convection and radiation from the external heat source, the reactor consists of coil heaters as a heat source. And the gas flows through the quartz tube from the opening to the other end and thermal insulators are installed at both ends of the furnace to decrease heat loss by conduction to surroundings. The CVD process allows carbon feedstock to deposit on a silicon wafer with a direction of inert gases at a specified temperature producing carbon nanotubes by introducing reactant gases. A removable quartz tube of 20 mm inner diameter and 1800 mm length (GPE scientific Ltd., Bedfordshire, UK) is installed on the holders. The quartz tube is fixed by the Swagelok fixings (KF40 quick-connect coupling – QF40XVC150, Kurt J. Lesker, East Sussex, UK). One end is attached to a 1/4" (0.635 cm) diameter stainless steel pipe connected to the MFCs, and the other end is attached to a bubbler by PVC tubes inside the fume hood – which is used for checking the presence of flow. The workstation of Raspberry Pi control has been shown in figure 2.2, the opening of the furnace is connected to a few multiple MFCs by steel pipes. The MFCs is Omega ® FMA 5400A (Omega Engineering, Manchester, U.K.). is controlled by the programmed Raspberry Pi micro-controller to control the mass flow rate of various gases. Gases are drawn from the cabinets from the gas tanks. The flow is regulated by the MFCs which are listed in table 2.1.

The workstation of Raspberry Pi control is shown in figure 2.2, which shows the pressure gauge controllers (< 5 bar) above the workbench (labelled with the red square). The pressure gauges act as the safety functions and ensure less than recommended pressure only entering which may cause damage to the MFCs, which is recommended by the manual. and the Raspberry Pi computer attached to the monitor. The feeding gases, hydrogen (H_2), methane, low ethylene grade N3.5 (CH_4) & helium (He) (BOC Ltd, Guildford, UK) were controlled by the mass flow controllers (MFCs). The Mass Flow Controller (MFC) of Helium (He, 500 mL), Hydrogen (H_2, 50 mL) & Methane (CH_4, 50 mL) were in use in the experiments for the low flow cylinders are stored inside the gas cabinets attached with a stainless-steel pipe. The whole PID system diagram for the CVD setup is attached to the additional document).
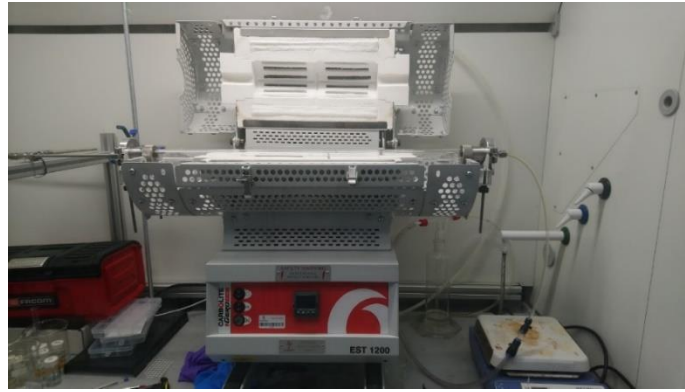
Figure 2.1. Carbonite Gero modal EST-1200 furnace

Figure 2.2. Station setup for Chemical Vapour Deposition (CVD)

Table 2.1. Setup of Mass Flow Controller (MFC) with various gases in the laboratory

Number	Gas types & maximum flow sccm for MFCs
1.	Nitrogen (0 – 500 sccm)
2.	Hydrogen (0 – 500 sccm)
3.	Helium (0 – 50 sccm)
4.	Helium (0 – 500 sccm)
5.	Methane (0 – 50 sccm)
6.	Methane (0 – 500 sccm)

2.3 Using ethanol as a solvent for catalyst preparation

Ethanol is commonly known as a universal solvent for dissolving polar, nonpolar, hydrophilic & hydrophobic compounds[3]. Therefore, it was chosen for the dissolution of iron catalyst at the beginning of this study. And ethanol has a lower surface tension than water, and a liquid form to deposit catalysts solution spreads rapidly on the Si/ SiO_2 surface. Ethanol was used as a suitable solvent for dissolving into polar compounds – which can dilute iron chloride catalyst in a solution effectively. The catalyst, iron chloride (III) solution ($FeCl_3$) – transition metal, is used in the formation of carbon nanotubes growth. The 16.2 mg solid iron (III) chloride catalyst (Sigma Aldrich, Gillingham, UK) was weighted on a digital scale, and the solution was diluted to the final concentration of 1 mmol in ethanol. The original iron chloride (III) was then diluted 10x times and 100x times in vials. The 100x dilute solutions then become a 100 µMol diluted solution.

Before the experiment, the N-type circular silicon disc (PI-KEM Ltd, Tamworth, UK) was cut into multiple silicon substrates (10 mm x 50 mm) and a silicon boat (10 mm x 30 mm) in a rectangle shape using a glass cutter (figure 2.3). The substrates and the boat are then put inside a beaker partially filled with isopropanol alcohol solution and put in a sonication bath for 10 minutes to remove any contamination and scarps on the surface produced manufacturing process. Finally, a droplet of iron chloride solution is dropped on the edge of a substrate with Pasteur pipette. The substrate was put at 45° degree tilted (figure 2.4) which allowed the catalyst concentrates at the edge of the silicon substate and dry by airflow in the fume hood, which overcome the "coffee strain" effect[4] (where most of the catalyst particles concentrate at the circumference of a droplet, rather than at the centre) of catalyst with the uneven catalyst deposition on Si surface[5] allows the carbon nanotubes to grow from the edge of the substrate.

Figure 2.3. Silicon boat and wafers cut from N-type silicon disc by a glass cutter

Figure 2.4. Silicon boat (front) and silicon substrate tilt in angle (back)

2.4 Using deionised water (di-water) as a solvent for catalyst preparation

Although ethanol solvent provides a good dissolving ability for various organics, it was observed from the early results that the dispersion of catalyst is somehow difficult to control on the Si substrate. The catalyst solution spreads rapidly on a Si/SiO_2 due to ethanol has a low surface tension. Therefore, the final surface concentration is not directly proportional to the original concentration because of the non-even and how quickly the solvent spreads on the silicon surface. A higher surface tension medium, such as deionised water (di-water) has a higher tendency to limit the spread of catalyst in combination with hydrophilic or hydrophobic interactions, an experimental work using iron-based material blended with different metallic catalysts (Ni, Co, Cu, Sn, Ga, Al & Mg) by using DI-water has been made to investigate the bimetallic-catalyst activities for UL-CNTs growth. The types of catalytic substances used in the experiments: 1) Iron (III) chloride ($FeCl_3$), 2) Copper (II) chloride dihydrate ($CuCl_2$), 3) Cobalt (II) chloride ($CoCl_2 \cdot 6H2O$) and 4) Nickel (II) chloride hexahydrate ($Cl_2H_{12}NiO_6$), 4) Tin (II) chloride ($SnCl_2$), 5) Gallium (III) nitrate hydrate ($GaH_2N_3O_{10}$), 6) Aluminium chloride ($AlCl_3$) & 7) Magnesium chloride dihydrate ($Cl_2H_4MgO_2$) were all used as received (Sigma-Aldrich, Dorset, UK). The catalyst quantities of 16.2 mg ($FeCl_3$), 13.4 mg ($CuCl_2$), 13 mg ($CoCl_2 \cdot 6H_2O$), 23.8 mg ($Cl_2H_{12}NiO_6$), 19 mg ($SnCl_2$), 27.4 mg ($GaH_2N_3O_{10}$), 13.3 mg ($AlCl_3$) & 13.1 mg ($Cl_2H_4MgO_2$)[5] were calculated from the desired concentrations. To investigate the bimetallic-catalyst activities, the preparation of catalyst solutions was done, the types of catalytic substances used in the experiments and the catalyst salts were combined with distilled water and be stored in multiple 20mL scintillation vials. The 1 mmol diluted catalyst solution from the previous weighted catalysts was placed in a sonication bath for 10 minutes. The

feedstock was then mixed with an equimolar concentration of each individual catalyst salts solutions and were agitated in a sonication bath to become homogeneous solutions.

Before each CNT growth experiment, the bi-catalysts solutions in vials were put in a sonication bath for 10 minutes before the experiment. Then, the clean silicon wafer was put on top of a glass dish using tweezers and catalyst solutions were deposited on the silicon substrate by a Pasteur pipette below the leading edge of the silicon substrate and dried on a 40 °C hotplate. Due to the surface tension of water, it would form a round-shaped droplet on the Si wafer as shown in figure 2.5.
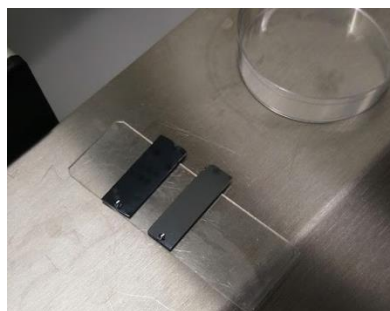
Figure 2.5. Di-water catalyst droplet on the silicon wafer

In order to investigate the composition of the catalysts at an elevated temperature, the dopped catalysts on a silicon wafer was inserted into a quartz tube and heated up to 950 °C and purging with helium gas at 100 sccm (the purpose of this procedure will be explained in chapter 2.5). In figure 2.6, the SEM images of a silicon wafer doped with catalyst droplet (Fe-Cu) was captured by JEOL 7800F SEM (the magnification at 100x). The image reveals some uneven distributed catalyst particles deposited on one area of the catalyst droplet.
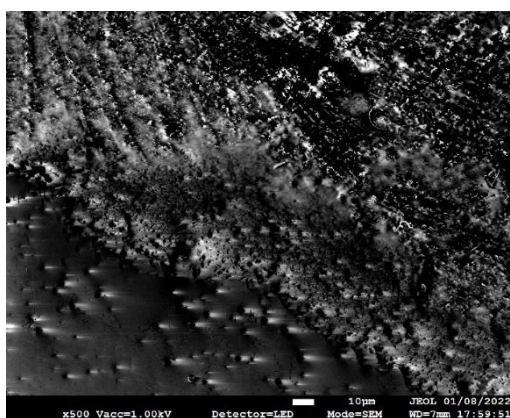
Figure 2.6. SEM image of Fe-Cu catalyst on one area of the catalyst droplet at 100x magnification from JEOL 7800F SEM

To further confirm the composition of the catalyst, the tabletop scanning electron microscope (SEM) (Hitachi TM3030, Hitachi, Tokyo, Japan) with the built-in module of Energy-dispersive X-ray spectroscopy (ESD) analysis - XSTREAM2 (Oxford instrument, Oxford, UK) was used. A zoom-in of the same catalyst area was imaged and be analysed, the SEM image was captured by the Hitachi TM3030 SEM at x10,000 magnification (figure 2.7).
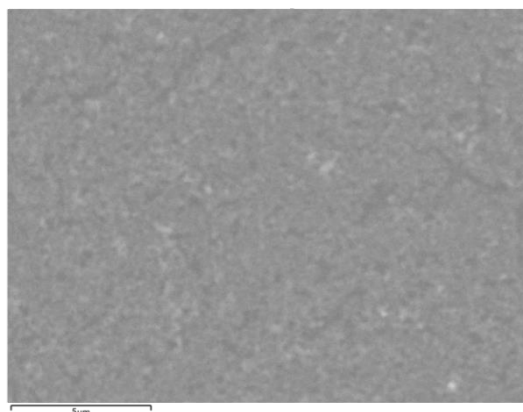
Figure 2.7. SEM images of Fe-Cu catalyst by using the Hitachi TM3030 SEM at x10,000 magnification

The working principle of the energy-dispersive X-ray spectroscopy (ESD) is that the electron beam excites the sample and leads to the X-ray emission due to vacancy formation, K-shell ionization, and following electron relaxation[6]. The differentiation of electrostatic discharge can be used to identify the atomic structure for chemical characterisations. For example: the distribution of the copper (Cu) and iron (Fe) contents from the bimetallic catalysts can be identified by this technique and shown in figure 2.8.
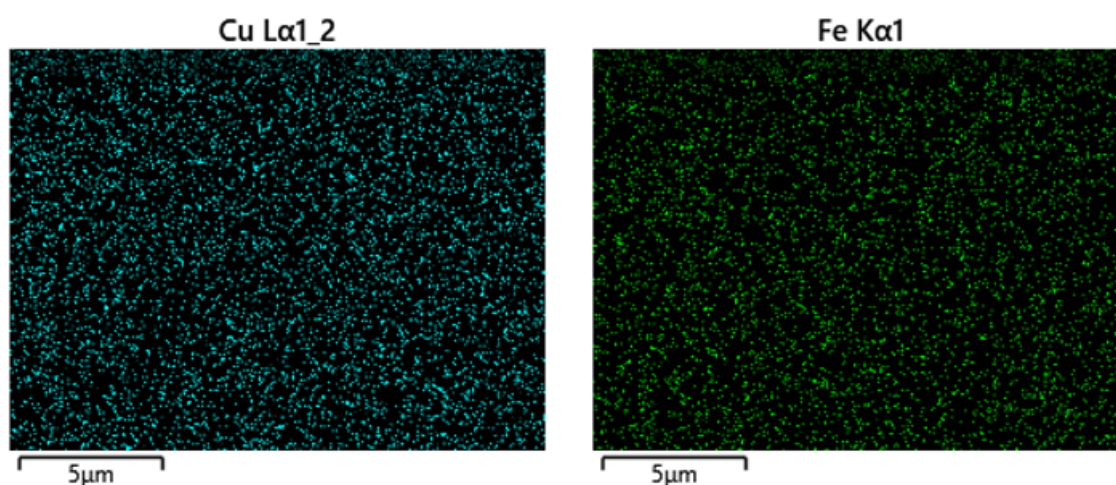
Figure 2.8. Catalyst composition of Cu (left) & Fe (right) using the ESD analysis

Furthermore, the percentage of elements (%) can be determined by the ESD analysis. The iron-copper (Fe-Cu) catalysts sample were found contained of oxygen (O), silicon (Si), carbon (C), iron (Fe) & copper (Cu) elements, with the weight percentage (%) and atomic percentage (%) (which relative to the total number of atoms) are listed in table 2.2. For the weight percentage (%), most of the silicon (Si, 81.58 %) are from the background reflections of the silicon wafer. It is followed by the detection of oxygen (O, 10.36 %) and carbon (C, 5.96 %) contents, which are mainly attributed to the formation of the metallic oxide (for example, iron (III) oxide (Fe_2O_3) & copper (II) oxide (CuO)) at an elevated temperature and the deposition of amorphous carbon from the inner wall of a used quartz tube. The iron (Fe, 1.83 %) and copper (Cu, 0.27 %) contents from the particular location from the analysis have proved that the catalyst droplet is not entirely homogenous with a higher ratio of iron (Fe) than copper (Cu) content.

Table 2.2. Weight and atomic percentage in map sum spectrum

Map Sum Spectrum	Weight %	Atomic %
O	10.36	15.85
Si	81.58	71.10
C	5.96	12.14
Fe	1.83	0.80
Cu	0.27	0.11
Total	100.00	100.00

The mixture of bimetallic catalysts and subsequent alloy formation is subjected to the complex crystallographic structure. It is further reported that the degree of alloy formation depends on the ratio of compositions and the amount of element present[7] and will be discussed in the later section, combined with the investigation of the temperature effects on the carbide formation and the melting temperature which would affect the carbon nanotube growth.

2.5   Ultra-long Carbon nanotubes (UL-CNTs) growth methods and procedure

The silicon substrate is put on the silicon boat at 10 mm back at the leading edge. It was placed at the centre of the quartz tube of 1800 mm length with 20 mm inner diameter (GPE scientific Ltd, Bedfordshire, UK), which is the hottest position of the furnace. The silicon boat is placed at the centre line of the quartz tube horizontally. A thermocouple was used to ensure

the temperature variations were corrected at 950 °C. One droplet of iron chloride is dropped on the edge of the substrate with a pipette. Before the chemical vapour deposition (CVD) process, substrate samples were placed on a separate silicon boat which fit in a quartz tube (figure 2.9). Then using a rod push and the whole apparatus is installed back to the finance fixing with the fittings and cover was closed. The mass flow controllers (MFCs) are controlled by the Raspberry Pi ® 400 microchip controller. The reaction procedure is listed in table 2.3: Wearing gloves and using tweezers for moving the substrate is essential for maintaining the cleanliness of the Si/SiO_2 wafer.
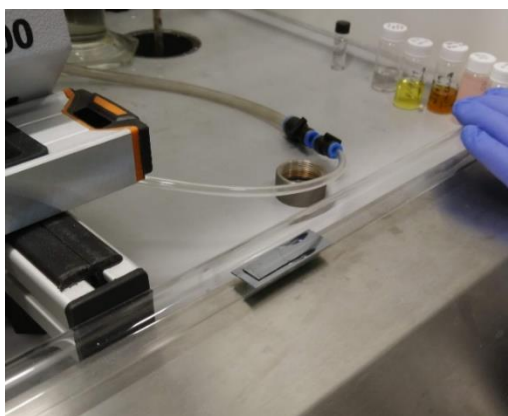
Figure 2.9. Silicon substrate and silicon boat in a quartz tube

Once the silicon boat with the substrate is then placed at the centre of the quartz tube precisely, the furnace cover is then subsequently closed and heated up from room temperature to 950 °C degree with a purging of helium gas (He) at 100 sccm (step 1) to remove residual air and until it reaches to a steady temperature at 950 °C, the helium is paused and an additional 15 minutes of hydrogen (H_2, 30 sccm) to ensure hydrogen is filled inside the quartz tube abundantly (step 2). Then, changing the reaction to hydrogen (H_2, 20 sccm) & methane (CH_4, 10 sccm) mixture (2:1 ratio) keeping at the same temperature for further 30 minutes (step 3) and then the covering of the furnace is opened then subsequently cooled down to room temperature with the change of helium (He, 30 sccm) at the end of the process (step 4).

During the growth phase of carbon nanotube, the methane gas will crack down to carbon atoms and hydrogen, and carbon atoms form the structure of carbon nanotubes. The functions for these feeding gases are as follow: I) Helium (He): a pre-treatment process that keeps the particle stabilised, a noble gas to remove air and impurities inside the quartz tube and assumed the absence of oxygen can prevent the formation of metallic oxide[8], II) Hydrogen (H_2): Activate the carbon source and prevent any oxidation during the reaction, III) Methane (CH_4):

the primary carbon source which allows carbon nanotubes (CNTs) forms. Finally, the exhausted gas was connected to the bubbler filled with mineral oil to ensure a continuous flow in the system.

Table 2.3. Primary setting of temperature and time length for different gases for UL- CNTs

Procedure	Gas types	Temperature	Time length
1	Helium, He (100 sccm)	950 °C	10 minutes
2	Hydrogen, H_2 (30 sccm)	950 °C	15 minutes
3	Hydrogen, H_2 (20 sccm) + Methane, CH_4 (10 sccm)	950 °C	30 minutes
4	Helium, He (30 sccm)	From 950 °C to room temperature	Until temperature reaches to the room temperature

The medium for the annealing phase, the Helium gas (He) was used as the density values for Helium (He) and Argon (Ar) are 0.1785 g/L & 1.78 g/L at Standard Temperature and Pressure (STP)[5]. Regardless of the temperature effect, the carbon nanotubes are deemed to experience a greater uplift in Argon than in Helium, which according to the Archimedes' principle[9]: $F_b = - \rho g V$, where Fb is the buoyancy force (N), ρ is the fluid density (kg/m^3), g is the gravity (m/s^2) & V is the fluid volume (m^3).

It is assumed that the fluid volume and gravitational force are identical from the above equation, the carbon nanotubes would experience higher buoyancy force and greater forced convection due to higher density fluid. Taking the thermal buoyancy into account, the heat capacity (Cp) for Helium (He) and Argon (Ar) are 5.19 J/g K & 0.31 J/g K and nearly 19 times more[5]. Therefore, Helium (He) can store and keep more heat energy to the increment of temperature and create a larger temperature difference and a larger density gradient for the thermal buoyancy. The standard procedure based on the 3D purging simulation from COMSOL, the gas purging for the initial Helium (He) sccm is to shorten the processing time from 30 minutes to 10 minutes, by raising the flow speed from 30 sccm to 100 sccm. The function of helium (He) gas is to moisture the catalyst and to keep meditating. The methane (CH_4) gas is

to provide a deposition of carbon source onto the silicon wafer, while the hydrogen (H_2) gas is to keep activating the catalyst. The purpose of hydrogen is to act as an antioxidant agent. The cooling rate of the CVD chamber is 0.34 °C degree per second without covering opened, measured by a digital timer. And the heating rate of the CVD chamber is 1 degree per second. The H_2/CH_4 ratio was suggested by Orbaek (2011) & VM Sivakumar (2011) [10, 11]. Based on the findings, the 2.1 ratio has been found with the best optimum setting for growing ultra-long carbon nanotubes (UL-CNTs) at 950 °C as a datum.

2.6   Calibration of Mass Flow Controllers (MFCs) for carbon nanotubes growth

The calibration procedure was followed before the start of usage as recommended by the instruction manual from Omega ®[12]. It is an essential process to ensure that the gas input velocity is correct and consistent, for each carbon nanotubes growth is accurately presented by the correct flow rate (sccm). The various points of data were measured by a bubble meter by feeding gas attached from the quartz tube by hose and time taken by a stopwatch. The gas flow drove the soap water bubble until it reaches the recorded level.

The data were recorded and plotted into line charts in Excel. The final value from the equations was obtained from the calculation, then input into the programmer for Raspberry Pi. Due to the settings of the mass flow controller (MFC) used for nitrogen (N_2), the K factor was multiplied according to the instruction manual from Sigma ® (Table 2.4). Since the different settings of mass flow controller (MFC). The equations were contained in the graphs. The substrate and silicon boat were then placed in the middle of the quartz tube and gradually heated up to (aseptically). The results obtained from the preliminary analysis, provide the understanding of the Mass Flow Controller (MFC) is calibrated regularly to ensure the data is corrected. The value is monitored by the mass flow controller. Atmosphere pressure of the gas (y is the sccm, x is the percentage (%)). This is the example of equations from the calibration of Mass Flow Controller (MFC), (the accuracy was done by 10 times for each measured point)

y axis = volume flow rate per minute (sccm), x axis = set point (%) which put into the programming to the Raspberry Pi

Mass Flow Controller (MFC) of Methane (CH4) calibration equation:

$$y = 0.3781x - 0.0565$$

Mass Flow Controller (MFC) of Helium (He) calibration equation:

$$y = 16.324x - 30.296$$

Mass Flow Controller (MFC) of Hydrogen (H2) calibration equation:

$$y = 0.5133x - 1.0695$$

Table 2.4. Gas type with the corresponding K factor from FMA 5400A/FMA 5500A - Omega Engineering's manual

Gas types	K factor
Hydrogen (H$_2$)	1.43
Helium (He)	2.25
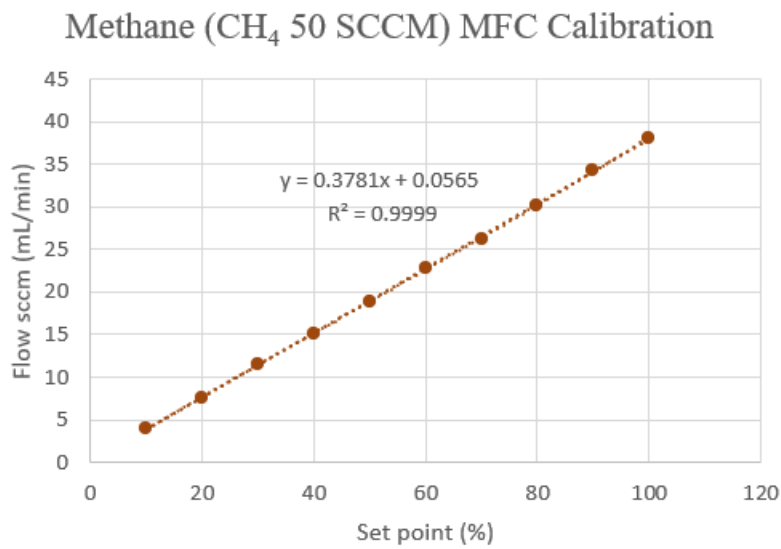
Figure 2.10. Chart of Mass Flow Controller (MFC) for Methane (He) calibration
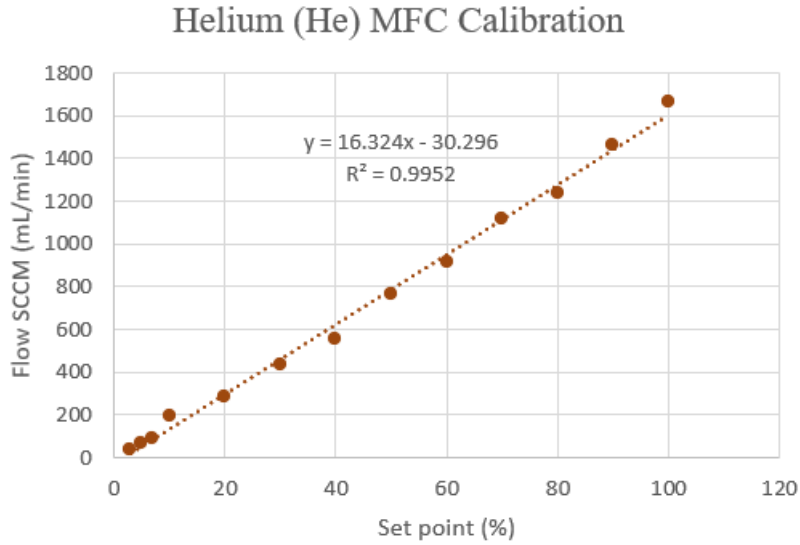
Figure 2.11. Chart of Mass Flow Controller (MFC) for Helium (CH$_4$) - 50 mL/min calibration
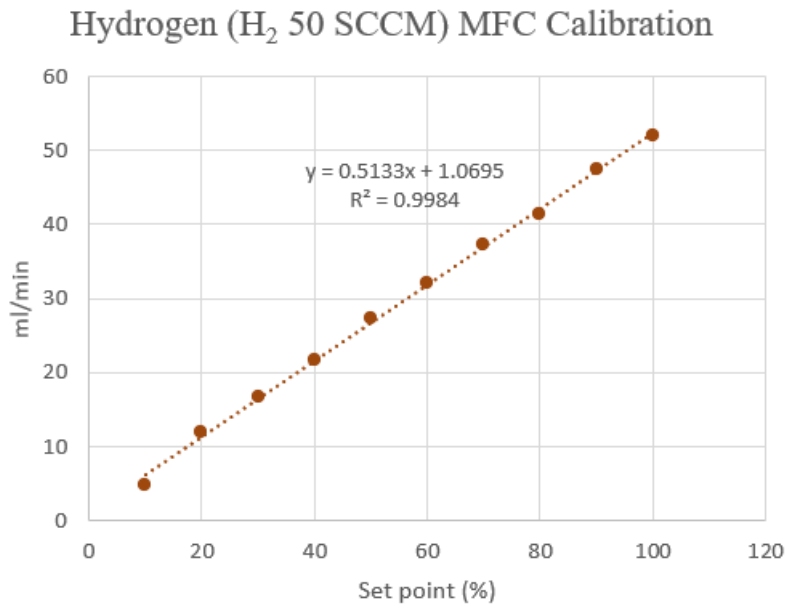
Figure 2.12. Chart of Mass Flow Controller (MFC) for Hydrogen (H$_2$) – 50 mL min calibration

The R-square (R^2) values for methane (CH$_4$), helium (He) and hydrogen (H$_2$) are 0.9999, 0.9952 and 0.9984. The values present how well the data fitted to the regression line. According to Cohen (1992)[13], r-square value 0.12 or below indicates low accuracy, between 0.13 to 0.25 values indicate medium, 0.26 accuracy or above and above values indicate high effect size. Therefore, the R^2 deem to above 0.26 and be acceptable in this case.

2.7   Temperature distribution of Carbonite Gero modal EST-1200 furnace

The temperature distribution along the quartz tube in the Chemical Vapour Deposition (CVD) at Carbolite Gero modal EST-1200 was measured by a thermocouple. The thermocouple is calibrated by the external furnace from carbolite regularly to ensure the most accurate temperature. The highest temperature of the system was measured 6 degrees higher than the default set point at 950 °C degree. The significant drop in temperature is occurred at the between the insulation blocks and surrounding to the atmosphere, which is 15 °C degree from 360 °C degree to 22 °C degree. A thermocouple is inserted inside the quartz tube at 950 °C degree. It is found that the temperature distribution is not consistent. The graph of the temperature distribution is below, the hot centre is + 6 °C degree higher than the indicator stated. Model of the thermocouple until it reaches a stable temperature. The thermocouple probe was placed in the centre in symmetric pulled out approximately 3cm each time and recorded 27 data points. The value is monitoring by the mass flow controller (MFC). Atmosphere pressure of the gas. The substrate and silicon boat were then placed in the middle of the quartz tube and gradually heated up to the default set point. The results obtained from the preliminary analysis, provide the understanding of the Mass Flow Controller (MFC) is calibrated regularly. Therefore, the silicon substrate at the centre to avoid any temperature variations that affects the carbon nanotube growth.
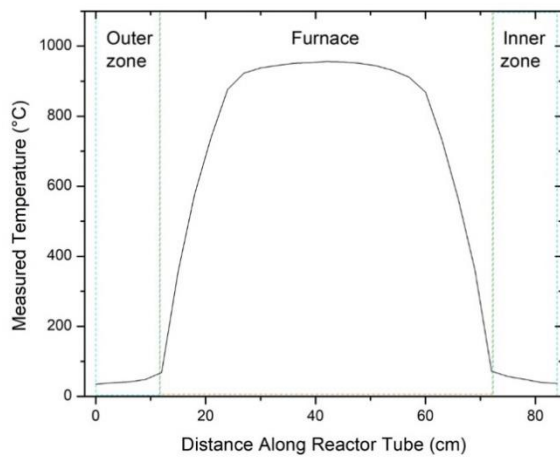
(a)   (b)

Figure 2.13. (a) Plot graph of temperature distribution over Chemical Vapour Distribution (CVD) device, (b) photo from actual experimental setup

It is observed that there is a significant drop of temperature at the entering of the insulation blocks and quartz tube and a graduate temperature fall symmetry on both sides for 20 °C degree. It may contribute to the fact that temperature differences in the unsteady flow due to a large sudden temperature drop (the isobaric effects – change in pressure fields due to work loss by temperature fall), regarding the thermal buoyancy force[14]. The carbon nanotubes cannot grow continuously, some exceptional become ultralong ones. Therefore, the silicon substrate is usually put at the centre of the quartz tube.

2.8   Ultra-long carbon nanotubes (UL-CNTs) by deionised water (di-water)

Since the disperse of an organic solvent such as ethanol has not related to the origin concentration due to how quickly the solvent disperses on the Si surface. Also, the allocation of the carbon nanotubes is also a time-consuming process by SEM imaging. Thus, the deionised water (di-water) method was adopted in this study, and another purpose is to investigate the behaviours of bimetallic catalysts (Fe-Cu, Fe-Co, Fe-Ni, Fe-Sn, Fe-Ga, Fe-Mg & Fe-Al) samples and a controlled sample of monometallic iron catalyst were performed under CH_4/ H_2 carrying gases (2:1 ratio, 30sccm) at 950°C in the CVD process. These instruments, scanning electron microscope (SEM), Raman spectroscopy and optical microscope will be used to check the characteristics of carbon nanotubes. For each type of catalyst sample, these samples were reproduced 3 times to ensure consistency. The SEM images captured in the columns under the catalysts until the end frame. Due to the surface tension, the catalyst droplet is holding on the silicon substrate. As for the iron-gallium (Fe-Ga) samples, the evidence suggests that the mixing catalyst ratio (1:1) seem to be relatively high in preventing UL-CNTs growth. Therefore, in the subsequent experiments the content of gallium (III) nitrate hydrate was reduced to minimum to 9:1 ratio. The sample Raman spectrum by three different lasers, 457 nm, 633 nm & 785nm are shown in figure 2.14 (a), (b) & (c). The sample of stacked SEM images are shown in figure 2.15 & 2.16 (Fe, Fe-Cu). The settings of the Jeol SEM were 1kV operating voltage, 1,000 pA and x 500 magnification with the low electron detector (LED) mode. The SEM images for each column until the whole carbon nanotubes were captured and stacked the images using GIMP software.
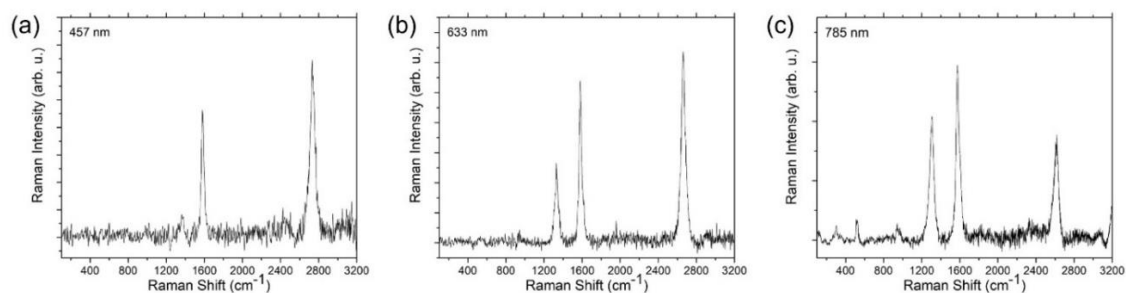
Figure 2.14. Raman spectroscopy data of CNTs grown from FeCl$_3$ measured using various lasers of a) 457 nm b) 633 nm and c) 785 nm wavelengths.

Figure 2.14 shows the resonant Raman spectra collected for CNTs grown from Iron (III) chloride (FeCl$_3$) as a control example at three different lasers (457 nm, 633 nm & 785 nm) to help represent the entire ensemble of graphitic carbon on the silicon wafer. The differing wavelengths can excite CNTs of different diameters and chirality's[15], which helps given it is otherwise non-trivial to estimate the nature of the CNTs and associated number of walls with the currently available data. The absence of a G-band at 457 nm, as seen in figure 2.14 a, indicates that the samples being characterised were multi-walled carbon nanotubes (SWCNTs) and unlikely to have smaller diameter CNTs than 5.3 nanometre (nm) – which is the lowest possible diameter for single-walled carbon nanotubes (SWCNTs) at 457 nm wavelength from Kataura plot and beyond this diameter are more likely belonged to MWCNTs. Proceeding further, we see definite graphitic carbon in addition to 2D-bands with the other two lasers, which helps indicate the presence of CNTs.
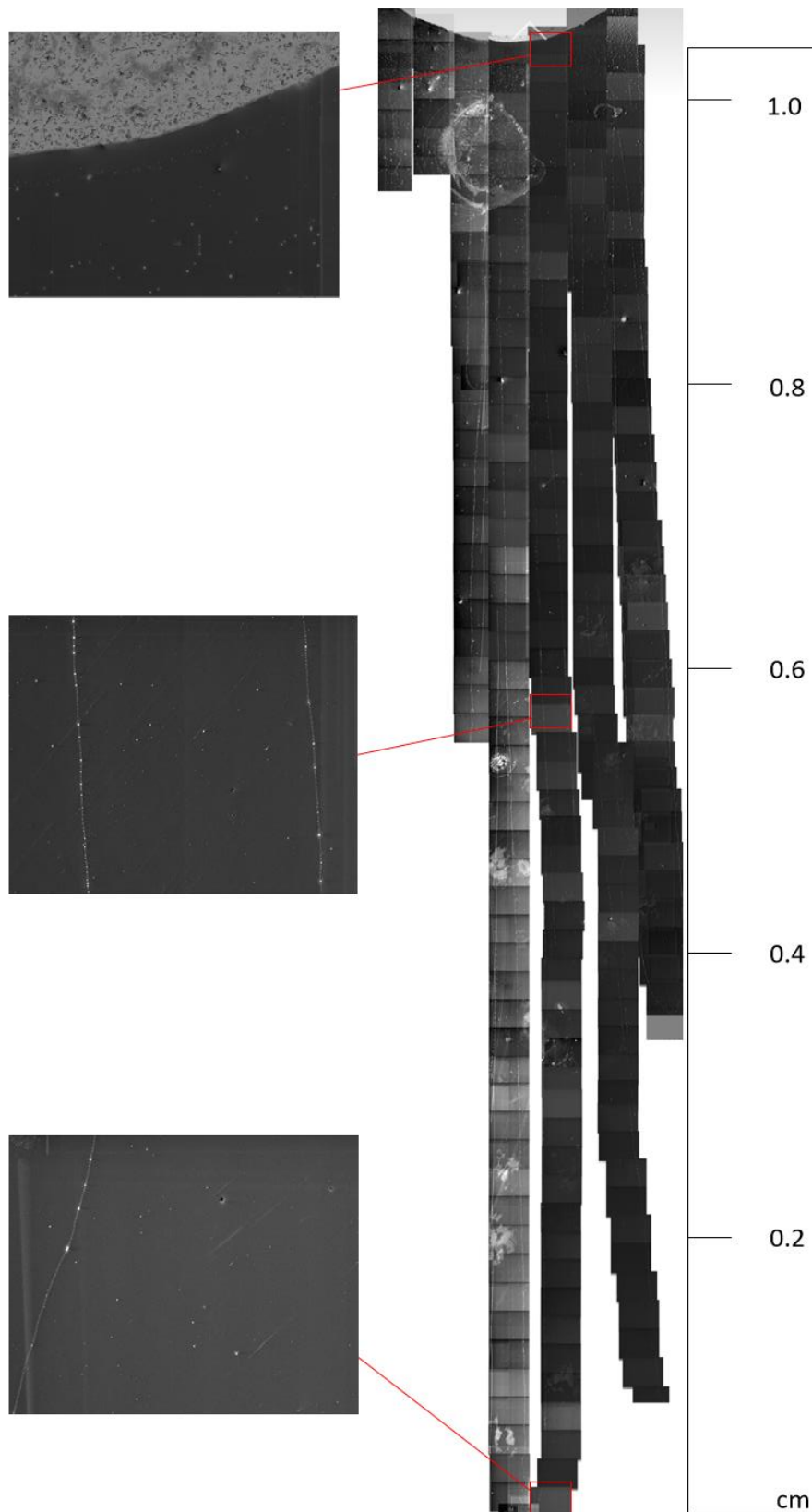
Figure 2.15. Stitched SEM images of example ultralong CNTs grown from Fe with top, middle, and bottom images
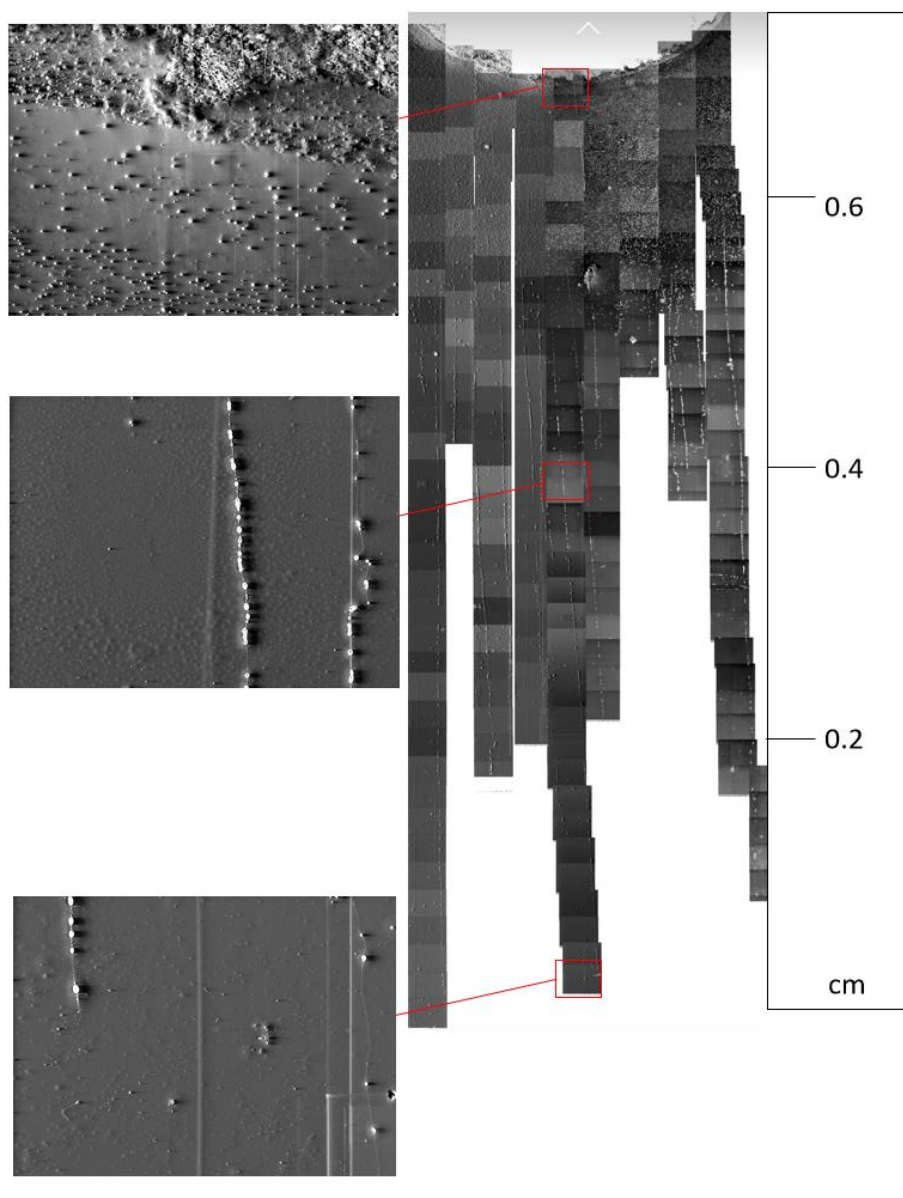
Figure 2.16. Stitched SEM images of example ultralong CNTs grown from Fe-Cu catalyst with top, middle, and bottom images

From the information provided in figure 2.15 and 2.16, the carbon nanotubes grown by one of the iron catalysts samples (figure 2.15) are generally longer than those produced by the bimetallic catalysts such as iron-copper (Fe-Cu) catalyst (figure 2.16) in this case. Further evidence proved by the data presented in table 2.5, the longest CNT observed for iron (Fe) & iron (Fe-Cu) catalyst was 1.32 cm & 0.85 cm respectively. In addition, iron-tin (Fe-Sn), iron-gallium (Fe-Ga), iron-aluminium (Fe-Al) & iron-magnesium (Fe-Mg) catalysts were produced and used for carbon nanotubes growth. From the SEM images observed, there are some short

and wriggle CNTs formed on the catalyst island for iron-tin (Fe-Sn) samples (figure 2.17), and the absence of UL-CNTs. The yield of the carbon nanotubes growth is excessively high for the iron-gallium (Fe-Ga) and iron-aluminium (Fe-Al) samples, the SEM images in figures 2.18 (Fe-Ga) & 2.19 (Fe-Al) have shown that some abundant nanotubes formed adjacent to the catalyst island and therefore hinder the UL-CNTs growth. The iron-aluminium (Fe-Al) catalyst has some marginally lower density than iron-gallium (Fe-Ga) catalyst, with a few and shorter UL-CNTs growth escaping from the catalyst island and the area of CNTs bundles.
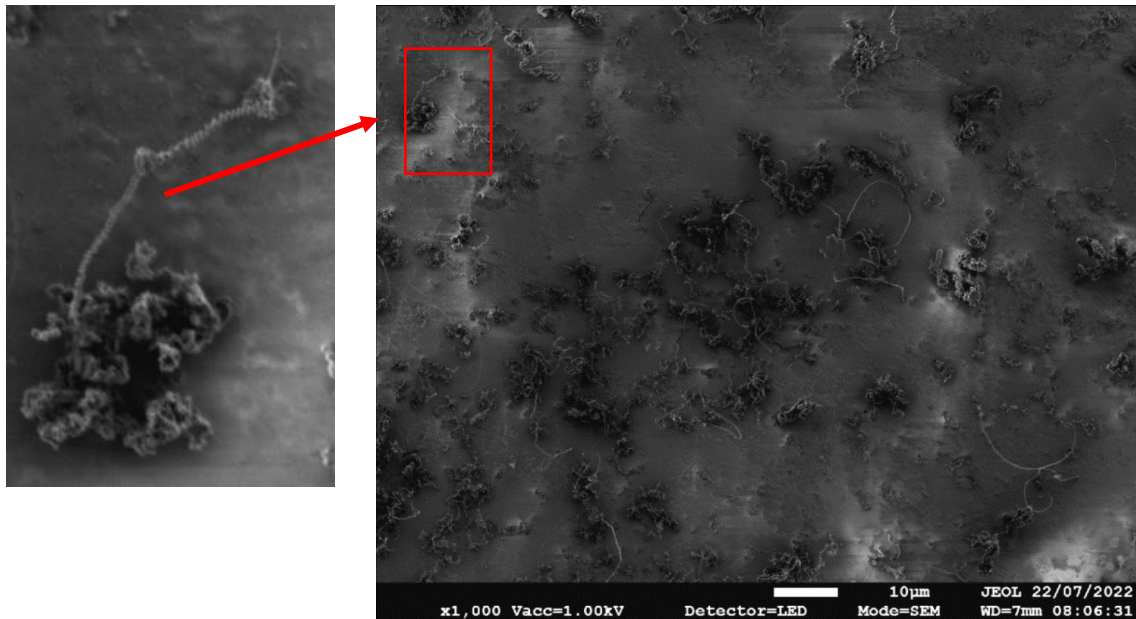
Figure 2.17. SEM image of Fe-Sn sample, captured at 1,000x magnification

After the modification of the iron-gallium (Fe-Ga) catalyst solution with gallium to a minimum content, some UL-CNTs were observed, and the longest CNT length is 0.13 cm. For the iron-aluminium (Fe-Al), there are some UL-CNTs extended from the catalyst island. Interestingly, it was observed that the abundant CNTs of on the adjacent of catalyst island for the iron-magnesium (Fe-Mg, figure 2.17) & iron-gallium samples (Fe-Ga, figure 2.18).
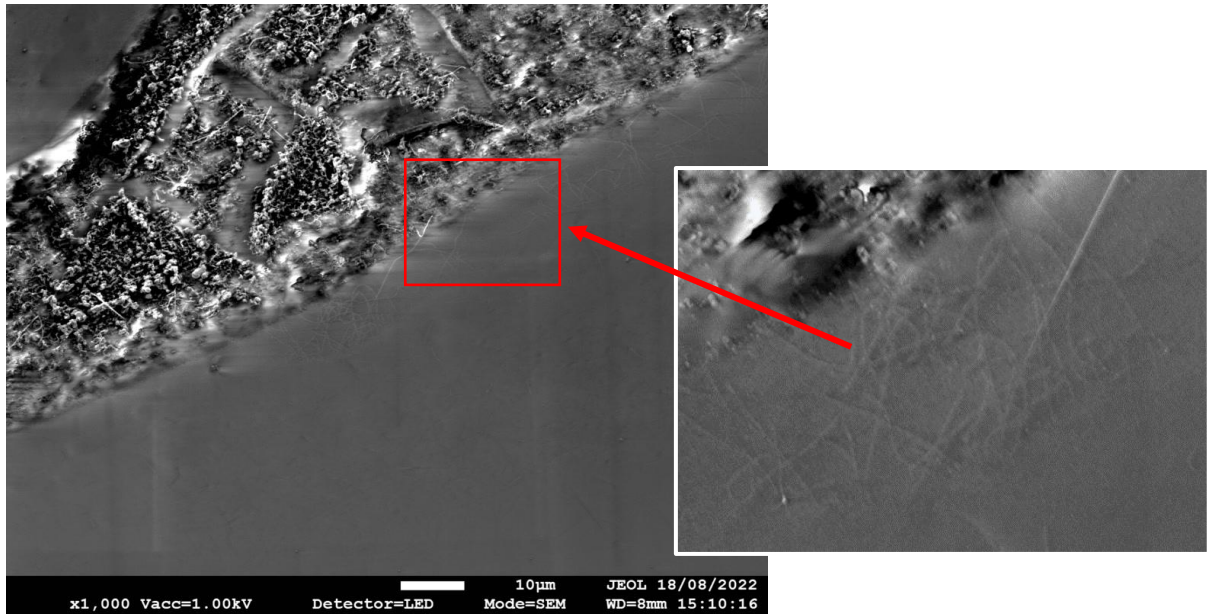
Figure 2.18. SEM image of Fe-Ga sample, captured at 1,000 x magnification
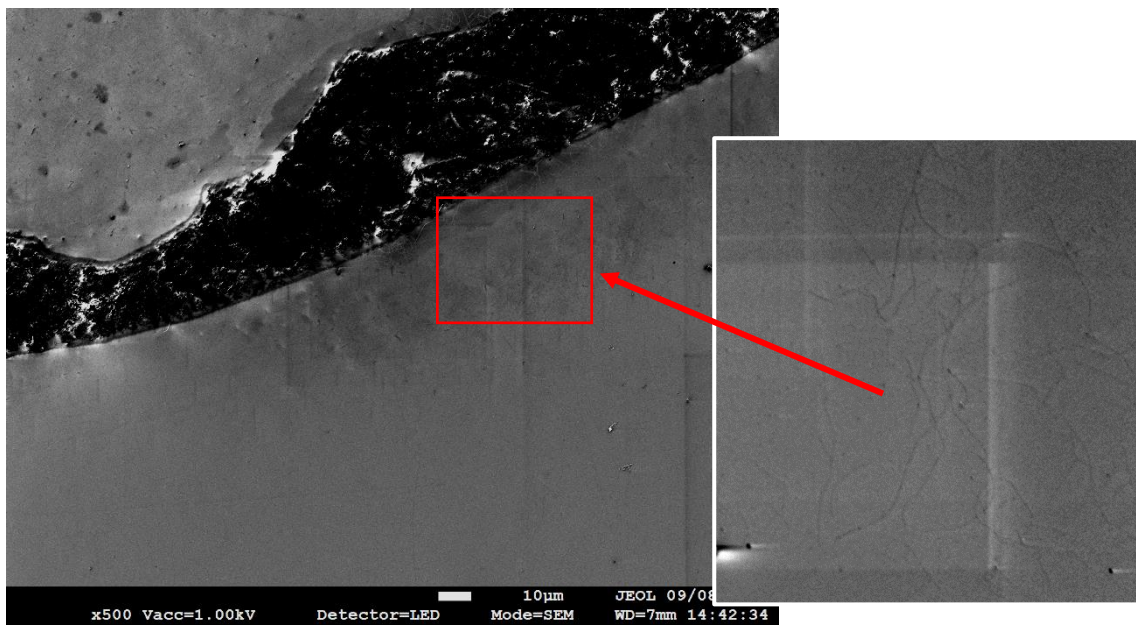
Figure 2.19. SEM image of Fe-Al sample, captured at 500 x magnification

Table 2.5. Longest CNTs length and the calculated growth rate

Type of catalyst	Longest CNT observed (cm)	Calculated growth velocity (μm/s)
Fe	1.32	7.33
Fe-Cu	0.85	4.72
Fe-Co	0.65	3.61
Fe-Ni	0.55	3.06
Fe-Sn	-	-
Fe-Ga	-	-
Fe-Mg	0.29	1.61
Fe-Al	0.13	0.72
Fe-Ga (9:1 ratio)	0.11	0.61
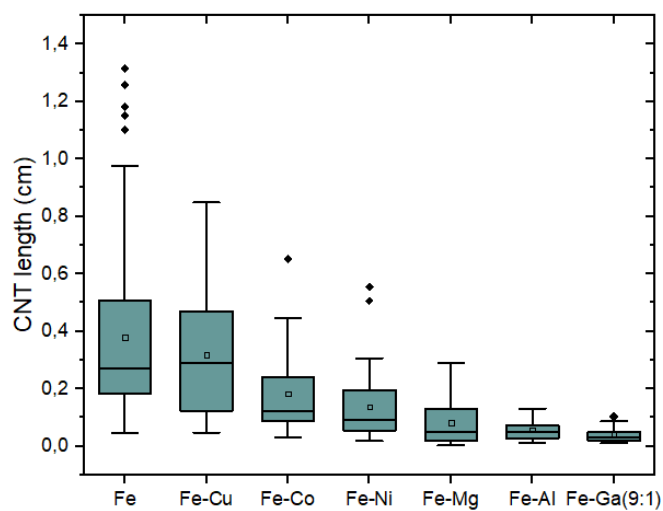
Figure 2.20. (a) Box plot of CNT length for Fe, Fe-Cu, Fe-Co, Fe-Ni, Fe-Mg, Fe-Al & Fe-Ga (9:1 ratio) catalysts
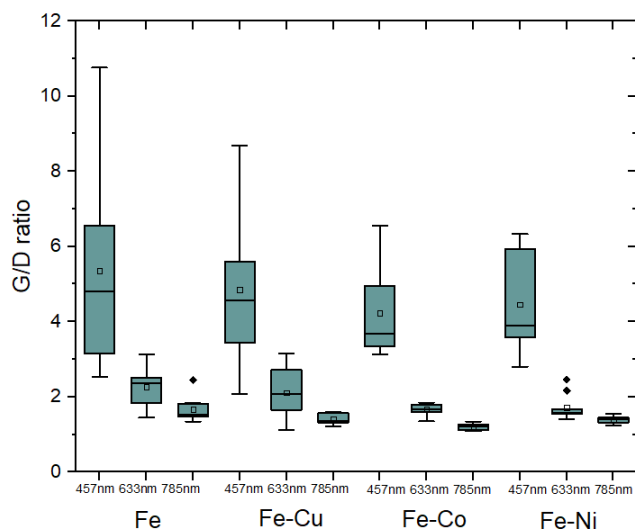
Figure 2.21. Box plot of the G/D ratio for at 457 nm, 633 nm, and 785 nm Raman laser excitation wavelengths for Fe, Fe-Cu, Fe-Co & Fe-Ni catalysts
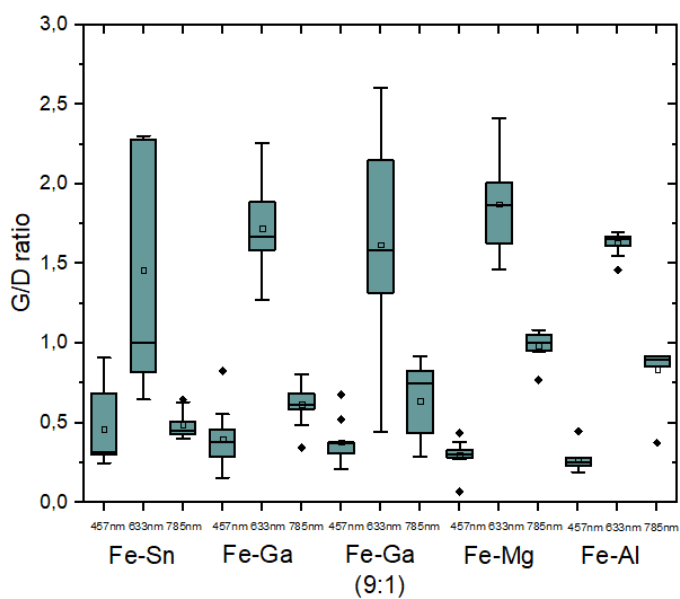
Figure 2.22. Box plot of the G/D ratio for at 457 nm, 633 nm, and 785 nm Raman laser excitation wavelengths for Fe-Sn, Fe-Ga, Fe-Ga (9:1 ratio), Fe-Al & Fe-Mg catalysts

It is noted that the iron-tin (Fe-Sn), iron-gallium (Fe-Ga) & iron-magnesium (Fe-Mg) have no UL-CNTs produced, the longest carbon nanotubes observed in this work were iron (Fe, 1.32 cm), iron-copper (Fe-Cu, 0.85 cm), followed by iron-cobalt (Fe-Co, 0.65 cm), iron-nickel (Fe-Ni, 0.55 cm), iron-gallium (9:1 ratio) (Fe-Ga, 0.11 cm), iron-magnesium (Fe-Mg, 0.29 cm) & iron-aluminium (Fe-Al, 0.13 cm) from table 2.5. In statistics from the boxplot (figure 2.20), the iron catalyst (Fe) has a wider range of CNTs length (from 0.05 - 1.32 cm) and the second place for iron-copper catalyst (Fe-Cu, from 0.05 – 0.85 cm). The iron-cobalt (Fe-Co, from 0.02 – 0.65 cm), iron-nickel (Fe-Ni, from 0.02 – 0.55 cm), iron-gallium (9:1 ratio) (Fe-Ga, from 0.01 – 0.11 cm), iron-magnesium (Fe-Mg, from 0.01 – 0.29 cm) & iron-aluminium (Fe-Al, from 0.01 – 0.13 cm). In the outliners from iron (Fe), iron-cobalt (Fe-Co) & iron-nickel (Fe-Ni) samples, there are few exceptional long UL-CNTs from the rest of the growing carbon nanotubes.

Given the fact that the growth conditions were consistent within 30 minutes timeframe, the growth rate (μm/s) can be calculated by dividing the CNT growth length (μm) by the total growth time (s). Hence, the rate of growth for the various catalysts are Fe (7.33 μm/s), Fe-Cu (4.72 μm/s), Fe-Ni (3.61 μm/s), Fe-Co (3.06 μm/s), Fe-Ga (9:1 ratio) (1.61 μm/s) & Fe-Al (0.72 μm/s). It is apparent that Fe-Co & Fe-Ni have a narrower range and shorter. The median is Fe (0.27 cm), Fe-Cu (0.29 cm), Fe-Co (0.12 cm), Fe-Ni (0.09 cm), Fe-Ga (9:1 ratio) (0.03 cm), Fe-Mg (0.05 cm) & Fe-Al (0.04 cm). The outliners indicate a particular longer one than the average and justify UL-CNTs. The iron catalyst (Fe) has a higher chance of growing UL-CNTs.

The outliners for iron (Fe), iron-copper (Fe-Co) and iron-nickel (Fe-Ni) system (figure 2.20) indicates there are some individual long carbon nanotubes are particular longer than the average length of carbon nanotubes. In figures 2.21 & 2.22, some randomly higher G/D ratio presented.

The qualitative analysis of carbon nanotubes using three separate lasers of 633 nm (1.96 eV), 785 nm (1.58 eV), 457 nm (2.71 eV) wavelength laser with a 5x magnification lens. In figure 2.14, one of the measurements, is the distinct graphene peak (G-peak), deflection peak (D-peak) & 2D peak. The Si peak at 520 cm^{-1} was removed. The average G/D ratio across all three wavelengths (457 nm, 633 nm & 785 nm) for the iron catalyst (Fe) was 3.09, the iron-copper catalyst (Fe-Cu) with 2.79, iron-cobalt catalyst (Fe-Co) at 2.17 and the iron-nickel (Fe-Ni) with 2.79. It is found that the iron-cobalt (Fe-Co) has the narrowest range of G/D ratio. For the 457 nm laser they were found to follow the order: Fe> Fe-Cu> Fe-Co> Fe-Ni, for the 633

nm laser they were found to follow the order: Fe> Fe-Co> Fe-Cu> Fe-Ni and for the 785 nm laser they were found to follow the order: Fe> Fe-Cu> Fe-Ni> Fe-Co. The iron-tin (Fe-Sn), iron-gallium (Fe-Ga), iron-gallium (Fe-Ga, 9:1 ratio), iron-magnesium (Fe-Mg) & iron-aluminium (Fe-Al) catalysts have the lowest range of G/D ratio from 0.15 to 2.60. The descending G/D ratio Raman intensities from 457 nm to 785 nm laser, may be attributed to the fact that the light source would influence the sensitivity of detecting the Raman signals. The 457 nm wavelength is in ultraviolet (UV) region, 633 nm in the visible light and the 785 nm in the near-infrared (near-IR) region. The Raman signal would gradually reduce as the source wavelength become longer, as the intensity of the Raman scattering is inversely proportional to the wavelength and the fourth power[16]. Therefore, the longer wavelength can avoid fluorescence, which is the emission of absorbed light and is commonly used for solely identifying inorganic materials, such as carbon nanotubes. And therefore, the longer wavelength produced less resolution, hence the 785 nm has a lower G/D ratio intensity than 457 nm. Another contributing factor is the spot size of the laser, the presence of a carbon nanotube inside the circumference will show the acquired G/D signal. Different laser wavelengths were performed and the excitation with carbon nanotubes can identify the chirality and diameters. The absence of G-band at 457 nm indicated that no more than a smaller diameter beyond.

In table 2.6, the catalyst values were calculated by radius ($r^2\pi$) and the density values can be calculated using the CNT count by dividing the catalyst area (mm^2).

Table 2.6. Catalyst diameter, CNT count and density from catalyst island and Raman G/D values

Type of catalyst	Sample No.	Catalyst area (mm^2)	CNT count	Density (CNT count. per mm^2)	Average Raman G/D intensity	Maximum Raman G/D intensity
Fe	Sample 1	5.31	46	8.66	3.10	7.85
	Sample 2	6.16	27	4.38	2.33	4.00
	Sample 3	7.07	23	3.25	3.85	10.76
Fe-Cu	Sample 4	3.80	19	5.00	2.21	4.57
	Sample 5	5.31	12	2.26	3.10	4.32
	Sample 6	4.15	20	4.82	3.06	5.59

Fe-Co	Sample 7	5.31	23	4.33	2.09	3.68
	Sample 8	6.16	11	1.79	2.14	4.18
	Sample 9	3.80	16	4.21	2.17	3.67
Fe-Ni	Sample 10	3.14	9	2.87	2.41	4.32
	Sample 11	6.16	11	1.79	2.36	6.33
	Sample 12	3.80	15	3.95	2.79	6.32
Fe-Sn	Sample 13	2.01	-	-	1.01	2.28
	Sample 14	3.80	-	-	0.67	2.28
	Sample 15	4.91	-	-	0.73	2.30
Fe-Ga	Sample 16	4.91	-	-	0.89	2.06
	Sample 17	3.80	-	-	0.85	0.88
	Sample 18	2.54	-	-	1.00	1.10
Fe-Ga	Sample 19	2.27	15	6.61	0.88	2.15
(9:1 ratio)	Sample 20	2.01	19	9.45	1.17	2.60
	Sample 21	2.83	15	5.29	0.58	1.50
Fe-Mg	Sample 22	2.27	62	27.3	1.06	2.41
	Sample 23	1.13	60	53.1	1.06	2.20
	Sample 24	1.33	65	48.9	1.03	2.01
Fe-Al	Sample 25	3.46	5	1.44	0.86	1.67
	Sample 26	1.54	17	11.05	0.93	1.70
	Sample 27	4.52	20	4.42	0.94	1.70
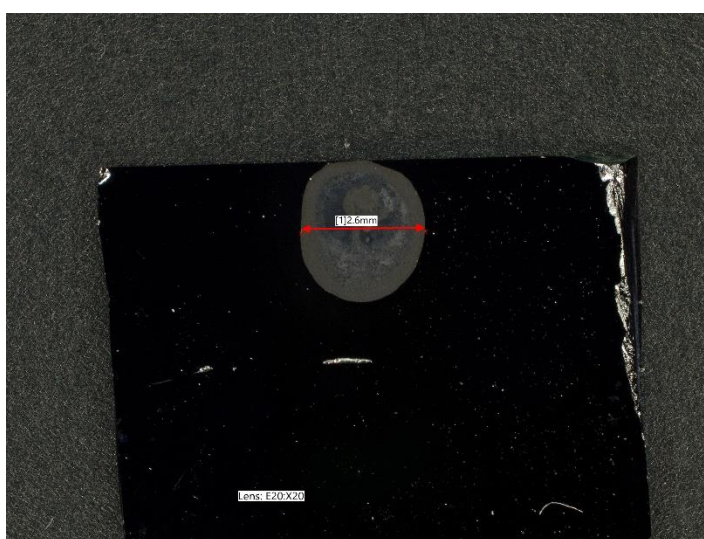
Figure 2.23. Catalyst droplet on silicon wafer under optical microscope
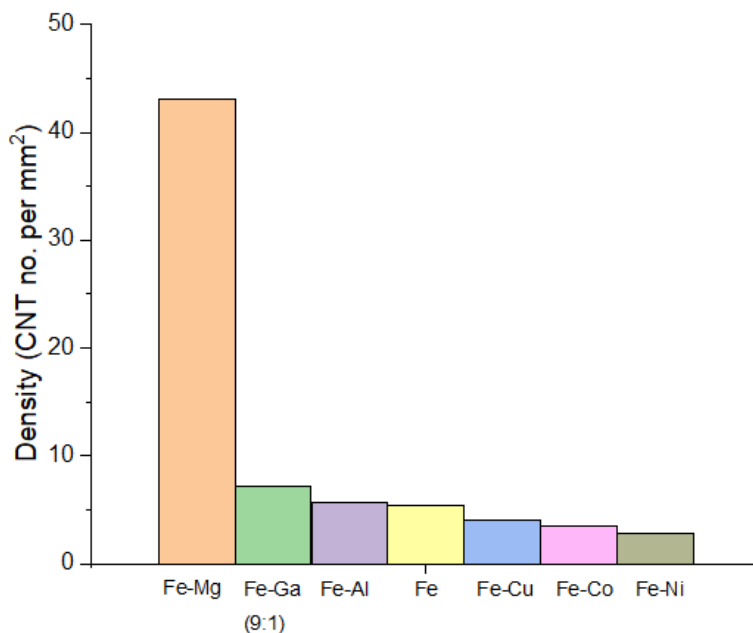
Figure 2.24. Density distribution of UL-CNTs per catalyst deposition location for each metal system (Fe-Ga (9:1), Fe-Al, Fe, Fe-Cu, Fe-Co & Fe-Ni)

A Keyence VHX-7000 microscope (Keyence Corporation, Osaka, Japan) was used to determine the size of the catalyst droplet and captured at 20x magnification to give general details on the diameter of the catalyst droplet. The data will be compared with the SEM images and Raman in the latter section. The count of CNTs from the SEM images & the size of the catalyst droplet from the optical microscope will be compared. The assumptions for the correlations between the catalyst concentration and density of UL-CNTs can be made. From the data from table 2.6, the diameters of the catalysts are ranged from 1.13 mm^2 to 7.07 mm^2, and the density is from 1.44 – 43.1 CNT no. per mm^2.

2.9   Discussion

The mechanism of growing carbon nanotubes can be used to understand how to produce CNTs with the control of diameter and helicity. A paper outlined some comprehensive steps for growing carbon nanotubes, mainly involving carbon diffusion, nucleation on catalyst particles and nanotube growth[17]. As the temperature has an essential role on the carbide formation and phase change of the catalyst particles, which eventually leads to carbon nanotube growth. The bimetallic catalysts can generally lower the growth temperature and provide higher

catalytic activities, thus enhancing the growth rate of carbon nanotubes. The formation of metal carbide acts as a precursor of forming carbon nanotube structure; the catalyst phase transition would reduce the catalyst lifetime and impact the growth of carbon nanotubes. For that reason, melting and carbide formation temperatures are important to evaluate the quality of carbon nanotube among different catalysts.

In the primary study, the plot of melting point and carbide formation temperature for iron (Fe), iron-copper (Fe-Cu), iron-nickel (Fe-Ni), iron-copper (Fe-Co), iron-tin (Fe-Sn), iron-gallium (Fe-Ga), iron-aluminium (Fe-Al) & iron-magnesium (Fe-Mg) catalysts in degree Celsius (°C). The gathered information from the tertiary diagram and various works of literature. The iron catalyst (Fe) has a melting temperature of 1,538 °C [18], followed by 1,485 °C (Fe-Cu)[19], 1,432 °C (Fe-Ni)[20] , 1,476 °C (Fe-Co)[21], 513 °C (Fe-Sn) [22], 908 °C (Fe-Ga)[23], 1,518 °C (Fe-Mg) [24] & 1,160 °C (Fe-Al)[25] and assumed 50% of element content referring to the tertiary diagram. And with the carbide formation temperature, the iron (Fe) has the temperature of 1,147 °C (Chipman)[26], and temperatures for Fe-Cu, Fe-Ni & Fe-Co from various sources: 1,300, 1,350 & 1,400 °C (Sheldudyakow)[27], 1,450 °C (Fuwa)[28], 1,550 °C (Mori)[29] & 1,600 °C (Koros and Chipman)[30] for Fe-Cu, 1,350 °C (Kramer)[31], 1,375 °C (Daniels & Pehlke)[32], 1,450 °C (Fuwa)[28] & 1,550 °C (Turkdogan)[33] for Fe-Co and 1,305, 1,405 & 1,485 °C (Miller & Elliot)[34], 1,350 °C (Turkdogan, Ward & Wright)[33,35], 1,550 °C (Mori)[36] & 1,600 °C (Schenck)[37] or Fe-Ni. And the decomposition of the iron carbide phase for Fe-Sn has been found at above 650 °C[38] and Fe-Al reported at the carbide formation temperature of 1,200 °C (Schneider)[39]. However, the availability of sources of carbide formation in the Fe-Ga-C and Fe-Mg-C are limited, and little is known. It is commonly accepted that Gallium (Ga) and Magnesium (Mg) are soft metals at room temperature. A reliable source has mentioned that the magnesium carbide is formed at temperatures of 450 °C (400 – 600 °C)[40]. All the temperature variables (Fe, Fe-Cu, Fe-Ni, Fe-Co, Fe-Sn, Fe-Ga, Fe-Mg & Fe-Al) were listed in the column scatter plot (figure 2.25).

Using iron catalyst as a datum (which has a melting temperature (1,538 °C) and carbide formation temperature (1,147 °C)). There are two types of catalysts: the iron-aluminium (Fe-Al) catalyst has a lower melting temperature (1,160 °C) and a higher temperature (1,200 °C) than iron catalyst, and the opposite catalyst has roughly the same melting temperature (1,518 °C) as the iron catalyst (Fe) and a lower carbide formation temperature (650 °C) than the iron catalyst (Fe) is iron-magnesium (Fe-Mg). Other types of bimetallic catalysts, such as iron-tin (Fe-Sn) & iron-gallium (Fe-Ga), have a lower carbide formation temperature and melting

temperature than the iron catalyst. By testing different catalysts and attempting to distinguish the effects of melting point and carbide formation temperature which would affect the overall quality of carbon nanotube growth.
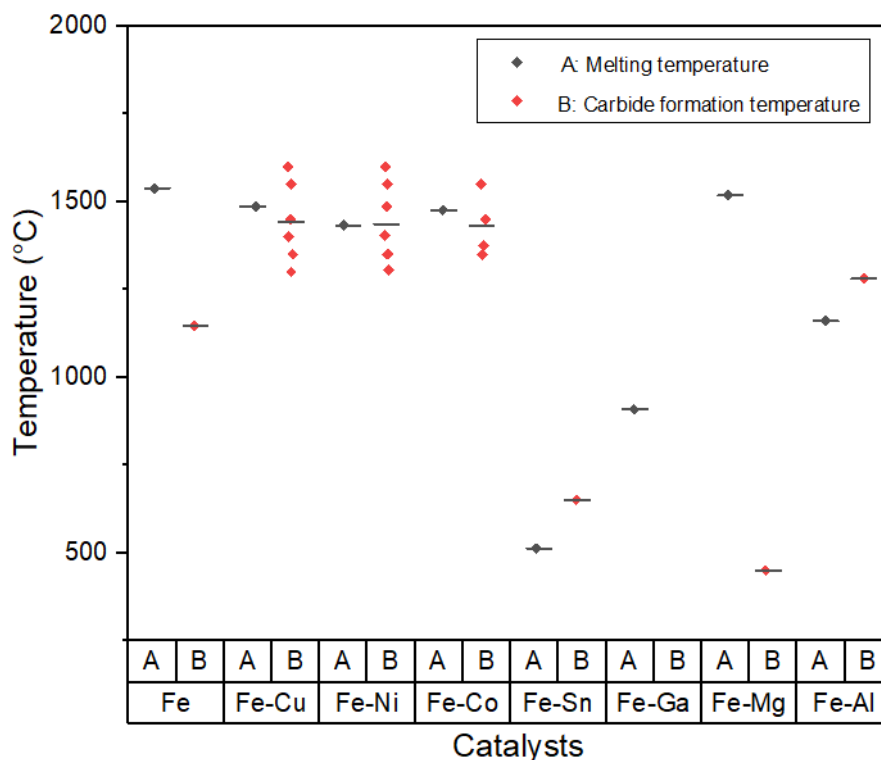
Figure 2.25. Temperature (melting temperature & carbide formation temperature) against different catalysts (Fe, Fe-Cu, Fe-Ni, Fe-Co, Fe-Sn, Fe-Ga, Fe-Mg & Fe-Al) in column box plot

The fundamental question of whether the formation of nanoalloy predominantly influences the carbon nanotube growth on a catalyst cluster is subject to the composition of the contents and the reaction temperature. For the degree of alloy formation, for example, in the iron-copper system (Fe-Cu) & iron-aluminium system (Fe-Al), we suggest that uniform metal particles form small crystals called "grains" for immiscible metals (Fe-Cu) and lattices for metals which have limited miscibility (Fe-Al) in equilibrium conditions[41].

The iron-copper system (Fe-Cu), consists of the immiscible phases of body-centred cubic (BCC) and face centred cubic (FCC) structure. The Fe (BCC) + Cu (FCC) structure forms at 600 – 850 ºC with the iron content <60 at % and the Fe (FCC) + Cu (FCC) structure found at 850 – 1050 ºC with the iron content between 60 – 80 at % [42]. In terms of the limited miscibility iron-aluminium system (Fe-Al), the formation of metallic compounds, for examples: Fe_3Al, $FeAl$, $FeAl_2$, Fe_2Al_5 & $FeAl_3$ formed from different weight percent of aluminium and

temperature range[43]. The recrystallisation of atoms are formed in a specific lattice arrangement. The iron aluminides are formed at the range of aluminium contents (35 – 50 at. %) between 400 – 1310 °C for FeAl and at around 25 at. % Al between 400 – 600 °C for Fe_3Al respectively[44].

As observed from the previous SEM image (figure 2.6) and the further EDS analysis (figure 2.8) in section 2.4, the catalyst particle distributions of iron (1.83 at.%) and copper (0.27 at.%) elements resulted in a heterogeneous deposition on a silicon substrate and given that the temperature was held at a constant 950 °C for a short timeframe in 30 minutes for particle aggregation. Due to the stoichiometry of the catalyst compositions, the findings of this study have suggested that the casually deposited catalyst droplet on a silicon wafer are more likely to be the blending of bimetallic catalysts than the formation of alloy.

Also, the addition of a second catalyst can change the crystal lattice and increase the diffusion process due to the deduction of energy between the carbon atom and catalyst. In this parametric study, methane is the main carbon source, and the carbon nanotubes were grown at 950 °C. The methane (CH_4) cracking temperature is higher than 1200 °C[45]. Thus, the bimetallic catalysts can lower the range of temperature in methane decomposition.

This study has shown that the monometallic catalyst (Fe) produces the longest (1.32 cm) and the highest G/D ratio (10.8) and densest CNTs (12/ mm^2) than other results of iron-based bimetallic catalysts as shown, such as iron-copper (Fe-Cu), iron-nickel (Fe-Ni) & iron-cobalt (Fe-Co). The principle of CNT growth can be explained using a vapour-liquid-solid method (VLS model)[46]. The decomposition of solid carbon species from vaporised methane gases are dissolved on the surface of a liquid-phase catalyst. The precursor (carbon atoms) is continuously dissolved until saturated and promotes carbon nanotubes growth. Iron is commonly used because of its high catalytic efficiency[47]. The activation energy of catalyst particle is equal to the diffusion energy of carbon atoms at the given temperature (950 °C) in this study[48]. The adherent iron particles (Fe) are mostly in a liquid state throughout the heating process, and the melting point is lower than that the bulk solid iron cluster. The coupling of carbon atoms onto the molten catalyst particles surface simultaneously would promote longer carbon nanotubes growth. And importantly, the formation of iron carbide (Fe_3C), which usually occurred at 1173 – 1100 K (900 – 1100 °C)[49]. This is a vital transition phase of amorphous carbon transform to the carbon nanotube, which with the evidence from our results shows the highest maximum G/D ratio.

The bimetallic catalyst of iron-copper (Fe-Cu) has the second overall maximum length of 0.85 cm, the highest G/D ratio (5.59), and the density (9 CNTs/mm^2). A small quantity of Cu additive in a rich iron catalyst has been previously shown to create longer CNT growth on average[50]. The miscibility of Cu particles into iron clusters leads to a stable condition to form carbon nanotubes, which may explain a greater diameter control from these results. However, given the fact that the higher concentration of iron-copper (Fe-Cu) catalysts in equ-molar as the excessive Cu may hinder the CNT growth[51]. Therefore, the additive of Cu is most likely to decrease the carbon solubility and consequently hinder the CNT growth in this study, which compared to the same results of iron monometallic catalysts.

The iron-cobalt (Fe-Co) catalyst has the third most active catalyst among other catalysts (Fe, Fe-Cu & Fe-Ni) in this study. The common growth temperature for Fe-Co was found at the range of 650 – 800 °C[52], which the associated with the reduced performance when the growth temperature at 950 °C. It is reported that iron-copper (Fe-Cu) catalyst can promote MWCNTs growth[53]. For the constrained carbon diffusion energy, the shorter CNTs may be attributed to the addition walls instead of forming longer CNTs.

The narrow range of CNT length (0.02 to 0.55 cm) for the iron-nickel (Fe-Ni) catalyst in this study, has been further proved by the previous study of the carbon nanotube growth using iron-nickel (Fe-Ni) bimetallic system in creating consistent CNT lengths[54]. The typical feeding gases used for iron-cobalt (Fe-Co) are methane and ethylene[55], which the ethylene is used for a much lower temperature (500 – 700 °C)[56]. It is commonly known that an active transition metal for graphitization reactions, which lower quality CNTs may be due to the excessive graphitic formation at the growth temperature[57] with the evidence from our results with the lowest G/D ratios. With the shortest average CNTs length of iron-nickel (Fe-Ni) catalyst (0.09 cm), it is possible that the activation energy is relatively high at this elevated activation temperature, and it would lower the carbon diffusion rate. The competition of growing longer CNTs with the chance of additional wall formation is similar to the iron-cobalt (Fe-Co) system.

The iron-tin (Fe-Sn) and iron-gallium (Fe-Ga) are deemed to have a far lower melting temperature and a carbide formation temperature than the iron catalyst below 1,000 °C[58,59]. These characteristics mean that more carbon nucleation occurred in the first place at a lower temperature and the subsequent distortion of the catalyst lattice as the catalyst particle appeared in a molten state before the growth temperature reached to 950 °C. The evidence suggested

that abundant and tangled CNTs were produced by iron-tin (Fe-Sn) & iron-gallium (Fe-Ga) catalysts due to their low carbide formation temperature. The shorter length of nanotubes is because of the phase change of the catalyst also at a lower temperature. Given an instability of coupling surface in a complete liquid phase, and therefore terminated the continues growth. And the nano coils were observed in the iron-tin (Fe-Sn) sample could be attributed to the five-membered rings systems[60]. These results match those observed in earlier studies by Li[61].

To investigate the interchange effects of melting temperature and a carbide formation temperature how would affect the carbon nanotube growth, iron-aluminium (Fe-Al, with a higher carbide temp and a lower melting temp than Fe catalyst) & iron-magnesium (Fe-Mg, with a lower carbide temp and an approximate the same melting temp than iron catalyst). For example, due to the restricted timeframe from increasing from the melting point (1,160 °C) to carbide formation temperature (1,200 °C) for iron-aluminium (Fe-Al) sample. A partially molten catalyst with some successful UL-CNTs growth was observed. As a result of the mobility of liquified catalyst on the surface, some growing nanotubes shifted from the original positions, more carbon diffusions replenished the sites and become more nanotubes. For the iron-magnesium (Fe-Mg) catalyst, which is particularly true that carbide formation happened at a lower temperature (650 °C), and a longer timeframe to reach the phase change temperature (1,518 °C). Therefore, carbon diffusion happened at multiple locations across the catalyst surface and in a stable condition for participation. Although the carbon yield is high for iron-magnesium (Fe-Mg) catalysts, the dense carbon nanotubes may prevent the growth of UL-CNTs due to collisions. Therefore, the iron-magnesium (Fe-Mg) has the far densest carbon nanotube growth, and the fifth place of longest carbon nanotubes after iron (Fe), iron-copper (Fe-Cu), iron-nickel (Fe-Ni) & iron-copper (Fe-Co) catalysts.

- Iron-gallium (Fe-Ga), iron-aluminium (Fe-Al) have many CNTs (Fe-Ga: Although some literature states no carbide formation – we found in our data – both has lower melting temperature than Fe, Fe-Al has slightly higher melting temp than Fe)
- Iron-magnesium (Fe-Mg) has the densest among other catalysts and average shorter UL-CNTs than iron – has lower carbide formation temperatures and approximately the same the melting temperature – the catalyst is not softened enough and few carbon diffusion until the temperature is reached – with a few locations

2.10   Conclusion

In conclusion, the iron catalyst was found to have the higher catalyst activity amongst the other catalysts[62] to increase the reaction rate to grow ultra-long carbon nanotubes. Ni is more efficient, and it shows higher activity at lower temperatures, 500- 600 °C[63]. Co is the least common due to its lower activity among these common catalysts[64]. A study has reported that the copper catalyst has found the least adhesive on silicon substrate than the iron catalyst[65], which means the catalyst would easily be lifted out and is better for tip growth. Previous work has found that the pure iron leads to bended and iron-copper (Fe-Cu) by a small addition of copper become uniform and slender CNTs[50], reducing the chance of CNT-CNT interaction and UL-CNTs. However, the high ratio of Cu may lead to a barrier due to its large particle. This work further proved that 1:1 ratio of iron-copper (Fe-Cu) may adversely affect the catalyst activity. The iron-tin (Fe-Sn), iron-gallium (Fe-Ga), iron-magnesium (Fe-Mg) & iron-aluminium (Fe-Al) catalysts have generally denser nanotubes growth than the iron (Fe), iron-copper (Fe-Cu), iron-nickel (Fe-Ni) & iron-cobalt (Fe-Co) catalysts. For the iron-tin (Fe-Sn) and iron-gallium (Fe-Ga) catalyst, the melting temperature and carbide formation temperatures are lower than the ones for the iron catalyst. This is certainly true in the case of these catalysts having a high yield of carbon nanotubes growth. Furthermore, the iron-aluminium (Fe-Al) and iron-magnesium (Fe-Mg) catalysts have a higher or lower melting temperature and carbide temperature than the iron catalyst. The differences between these two types of catalysts (iron-aluminium & iron-magnesium, Fe-Al & Fe-Mg) are that the aluminium one produced uncountable nanotube with a few UL-CNTs, and the magnesium one has the densest individual UL-CNTs.

The results have proved that the deionised water (di-water) can help contain the spread of a catalyst droplet on the silicon substrate. All the carbon nanotubes were grown downstream from the leading edge facing the inflow. For the di-water samples with iron-based bimetallic catalysts, the amount of random shorter CNTs indicates that the concentration may be too high, preventing the nanotubes from escaping the island, and CNT-CNT interaction due to Van der Waals force may prevent the escape of carbon nanotubes from the catalyst island. The results obtained by the SEM imaging and Raman spectroscopy have shown that iron catalyst has the longest CNT growth (1.32 cm), followed by iron-copper (Fe-Cu, 0.85 cm), iron-copper (Fe-Cu, 0.65 cm) & the shortest of iron-nickel (Fe-Ni, 0.55 cm), iron-magnesium (Fe-Mg, 0.29 cm) & the shortest iron-aluminium (Fe-Al, 0.13 cm). The data implies that the monometallic catalyst (Fe) using $FeCl_3$ has grown longer carbon nanotubes followed by the bimetallic

catalysts of Fe-Cu, Fe-Ni, Fe-Co, Fe-Al & Fe-Mg. With the combination of results, the iron catalyst, I) the second densest UL-CNTs among other catalysts, II) the maximum G/D intensity ratio & widest ranges of G/D values, which have suggested that the quality of the CNTs varied notably compared to the other bimetallic catalysts. It is important to note that iron-gallium (Fe-Ga) produces far densest carbon nanotubes with UL-CNTs. The future work includes lowering the catalyst concentration further and establishing a ratio of bimetallic catalysts which may work the best for UL-CNTs growth.

2.11   Additional information

Table 2.7. CNT length for catalysts in centimeter (cm)

CNT length for catalysts in centimeter (cm)							
Iron	Copper	Nickel	Cobalt	Tin	Fe-Ga (9:1)	Fe-Al	Fe-Mg
0.20	0.23	0.05	0.03	0.05	0.02	0.12	0.01
0.32	0.53	0.04	0.10	0.06	0.03	0.02	0.01
0.20	0.23	0.09	0.07	0.12	0.03	0.02	0.02
0.25	0.44	0.05	0.20	0.06	0.02	0.02	0.02
0.22	0.11	0.02	0.22	0.25	0.03	0.02	0.02
0.29	0.38	0.55	0.10	0.10	0.03	0.06	0.02
0.33	0.45	0.31	0.22	0.10	0.05	0.09	0.02
0.38	0.29	0.28	0.10	0.24	0.02	0.13	0.02
0.18	0.29	0.09	0.24	0.04	0.03	0.03	0.00
0.18	0.54	0.25	0.19	0.02	0.02	0.04	0.03
0.58	0.30	0.11	0.38	0.13	0.03	0.12	0.04
0.52	0.37	0.20	0.07	0.05	0.02	0.02	0.01
0.51	0.47	0.11	0.40	0.23	0.01	0.04	0.01
0.52	0.23	0.11	0.08	0.03	0.04	0.13	0.06
0.24	0.36	0.05	0.24	0.04	0.04	0.06	0.04
0.35	0.21	0.08	0.35	0.13	0.03	0.03	0.03
0.17	0.17	0.07	0.30	0.10	0.03	0.12	0.03
0.21	0.29	0.09	0.20	0.28	0.03	0.03	0.02
0.21	0.28	0.05	0.10	0.16	0.03	0.03	0.02
0.21	0.27	0.15	0.10	0.26	0.03	0.03	0.01
0.17	0.43	0.06	0.38	0.11	0.08	0.01	0.01
0.21	0.38	0.09	0.08	0.08	0.02	0.01	0.04
0.17	0.32	0.07	0.38	0.06	0.02	0.03	0.06
0.16	0.51	0.03	0.11		0.08	0.03	0.02
0.17	0.70	0.12	0.23		0.02	0.03	0.06
0.14	0.53	0.25	0.22		0.05	0.03	0.04
0.14	0.61	0.20	0.13		0.10	0.04	0.01
0.11	0.58	0.25	0.28		0.04	0.07	0.01

0.11	0.82	0.05	0.41		0.09	0.06	0.01
0.20	0.59	0.06	0.36		0.11	0.07	0.01
0.27	0.32	0.06	0.45		0.05	0.08	0.06
0.30	0.68	0.08	0.18		0.06	0.07	0.01
0.28	0.70	0.15	0.09		0.04	0.05	0.01
0.37	0.07	0.10	0.11		0.08	0.07	0.02
0.20	0.06	0.51	0.06		0.04	0.07	0.07
0.17	0.14		0.05		0.06	0.07	0.04
0.15	0.06		0.09		0.03	0.08	0.03
0.22	0.12		0.04		0.05	0.05	0.20
0.50	0.10		0.09		0.04	0.12	0.11
0.21	0.07		0.03		0.01	0.05	0.03
0.35	0.11		0.13		0.02	0.05	0.01
0.23	0.07		0.12		0.01	0.11	0.02
0.38	0.08		0.28		0.02		0.02
0.25	0.18		0.06		0.02		0.03
0.19	0.10		0.06		0.09		0.03
0.29	0.85		0.15		0.10		0.05
0.22	0.11		0.10		0.02		0.13
0.07	0.15		0.11		0.02		0.12
0.05	0.59		0.65		0.02		0.13
0.10	0.06		0.09				0.05
0.08	0.05						0.01
0.08	0.15						0.01
0.05	0.16						0.13
0.10							0.11
0.21							0.09
0.41							0.09
0.19							0.05
0.08							0.02
0.84							0.02
0.33							0.01
0.83							0.01
0.33							0.01
0.83							0.01
0.63							0.01
0.20							0.02
0.47							0.01
0.52							0.01
0.20							0.01
0.17							0.04
0.21							0.14
0.18							0.01
0.13							0.02
0.11							0.01
0.67							0.02

0.98							0.03
0.50							0.03
1.26							0.06
0.27							0.01
1.18							0.02
1.15							0.03
1.10							0.07
0.82							0.10
0.66							0.13
0.60							0.10
0.43							0.13
0.53							0.13
0.97							0.13
1.32							0.05
0.95							0.05
0.71							0.01
0.43							0.07
0.81							0.01
0.37							0.01
0.40							0.12
0.39							0.02
0.39							0.15
							0.15
							0.07
							0.05
							0.05
							0.17
							0.13
							0.01
							0.16
							0.13
							0.12
							0.11
							0.11
							0.10
							0.20
							0.19
							0.10
							0.11
							0.01
							0.02
							0.04
							0.04
							0.03
							0.03
							0.02

						0.01
						0.01
						0.01
						0.03
						0.00
						0.07
						0.05
						0.09
						0.07
						0.05
						0.04
						0.11
						0.09
						0.08
						0.22
						0.22
						0.22
						0.21
						0.21
						0.10
						0.04
						0.13
						0.28
						0.28
						0.28
						0.25
						0.29
						0.29
						0.27
						0.24
						0.22
						0.19
						0.18
						0.17
						0.17
						0.16
						0.16
						0.14
						0.13
						0.12
						0.12
						0.12
						0.10
						0.13
						0.19
						0.19

							0.20
							0.19
							0.20
							0.20
							0.13
							0.11
							0.21
							0.19
							0.19
							0.12
							0.12
							0.12
							0.10
							0.05
							0.04
							0.04
							0.04
							0.04
							0.02
							0.03
							0.05

Table 2.8. Raman intensity at 457 nm, 633 nm, and 785 nm wavelength

Type of catalyst		Location	G/D ratio at 457 nm	G/D ratio at 633 nm	G/D ratio at 785 nm
Fe	Sample 1	Location 1	4.82	1.45	1.83
		Location 2	7.85	3.12	2.44
		Location 3	2.71	2.35	1.34
	Sample 2	Location 4	3.14	1.79	1.63
		Location 5	2.53	2.47	1.37
		Location 6	4.00	2.53	1.49
	Sample 3	Location 7	10.76	2.51	1.53
		Location 8	6.56	1.83	1.53
		Location 9	5.79	2.30	1.80

Fe-Cu	Sample 1	Location 1	2.08	1.64	1.32
		Location 2	3.44	1.92	1.59
		Location 3	4.57	2.09	1.26
	Sample 2	Location 4	2.23	1.49	1.43
		Location 5	7.41	2.75	1.59
		Location 6	8.68	1.11	1.22
	Sample 3	Location 7	5.59	2.72	1.33
		Location 8	5.45	2.12	1.35
		Location 9	4.24	3.15	1.56
Fe-Co	Sample 1	Location 1	3.68	1.35	1.34
		Location 2	3.35	1.66	1.25
		Location 3	3.35	1.71	1.12
	Sample 2	Location 4	3.31	1.59	1.22
		Location 5	3.13	1.78	1.29
		Location 6	4.18	1.66	1.09
	Sample 3	Location 7	4.95	1.78	1.25
		Location 8	5.54	1.59	1.21
		Location 9	6.56	1.84	1.12
Fe-Ni	Sample 1	Location 1	3.67	2.16	1.45
		Location 2	3.24	1.59	1.24
		Location 3	4.32	2.46	1.52
	Sample 2	Location 4	3.58	1.55	1.32
		Location 5	2.80	1.40	1.31
		Location 6	6.33	1.54	1.41

		Location 7	3.90	1.46	1.41
	Sample 3	Location 8	6.32	1.67	1.55
		Location 9	5.94	1.58	1.29
Fe-Sn	Sample 1	Location 1	0.91	1.00	0.63
		Location 2	0.31	2.28	0.65
		Location 3	0.68	2.18	0.43
	Sample 2	Location 4	0.25	0.74	0.49
		Location 5	0.29	0.82	0.43
		Location 6	0.32	2.28	0.45
	Sample 3	Location 7	0.38	0.65	0.51
		Location 8	0.72	2.30	0.40
		Location 9	0.31	0.89	0.42
Fe-Ga	Sample 1	Location 1	0.28	1.37	0.68
		Location 2	0.38	1.62	0.66
		Location 3	0.38	2.06	0.59
	Sample 2	Location 4	0.46	1.58	0.59
		Location 5	0.25	1.67	0.61
		Location 6	0.83	1.27	0.34
	Sample 3	Location 7	0.15	1.79	0.80
		Location 8	0.30	1.89	0.78
		Location 9	0.55	2.26	0.48
Fe-Ga (9:1)	Sample 1	Location 1	0.52	1.31	0.29
		Location 2	0.21	1.59	0.83
		Location 3	0.68	2.15	0.37

	Sample 2	Location 4	0.38	2.60	0.92
		Location 5	0.37	2.10	0.81
		Location 6	0.38	2.22	0.75
	Sample 3	Location 7	0.31	0.44	0.43
		Location 8	0.36	0.65	0.49
		Location 9	0.21	1.50	0.85
Fe-Al	Sample 1	Location 1	0.45	1.46	0.37
		Location 2	0.23	1.67	0.92
		Location 3	0.22	1.55	0.89
	Sample 2	Location 4	0.25	1.70	0.85
		Location 5	0.28	1.66	0.89
		Location 6	0.19	1.61	0.92
	Sample 3	Location 7	0.23	1.67	0.92
		Location 8	0.28	1.66	0.89
		Location 9	0.25	1.70	0.85
Fe-Mg	Sample 1	Location 1	0.07	2.41	1.01
		Location 2	0.33	1.88	0.77
		Location 3	0.29	1.86	0.95
	Sample 2	Location 4	0.32	1.62	1.05
		Location 5	0.28	1.86	0.96
		Location 6	0.28	2.20	0.95
	Sample 3	Location 7	0.44	1.46	1.08
		Location 8	0.38	1.56	1.08
		Location 9	0.30	2.01	1.00

2.12   References

(1) Ahn, J. H.; Na, M.; Koo, S.; Chun, H.; Kim, I.; Hur, J. W.; Lee, J. H.; Ok, J. G. Development of a fully automated desktop chemical vapor deposition system for programmable and controlled carbon nanotube growth. *Micro and Nano Systems Letters* **2019**, *7* (1), 1-8.

(2) Yoshihara, N.; Ago, H.; Tsuji, M. Chemistry of Water-Assisted Carbon Nanotube Growth over Fe− Mo/Mgo Catalyst. *The Journal of Physical Chemistry C* **2007**, *111* (31), 11577-11582.

(3) Mohsen-Nia, M.; Amiri, H.; Jazi, B. Dielectric constants of water, methanol, ethanol, butanol and acetone: measurement and computational study. *Journal of Solution Chemistry* **2010**, *39* (5), 701-708.

(4) Majumder, M.; Rendall, C. S.; Eukel, J. A.; Wang, J. Y.; Behabtu, N.; Pint, C. L.; Liu, T.-Y.; Orbaek, A. W.; Mirri, F.; Nam, J. Overcoming the "coffee-stain" effect by compositional Marangoni-flow-assisted drop-drying. *The Journal of Physical Chemistry B* **2012**, *116* (22), 6536-6542.

(5) Lide, D. R. *CRC handbook of chemistry and physics*; CRC press, 2004.

(6) d'Alfonso, A.; Freitag, B.; Klenov, D.; Allen, L. Atomic-resolution chemical mapping using energy-dispersive x-ray spectroscopy. Physical Review B 2010, 81 (10), 100101.

(7) Couves, J. W.; Meehan, P. Combined XANES and EXAFS analysis of supported bimetallic catalysts. Physica B: Condensed Matter 1995, 208, 665-667.

(8) Sato, H.; Hori, Y.; Hata, K.; Seko, K.; Nakahara, H.; Saito, Y. Effect of catalyst oxidation on the growth of carbon nanotubes by thermal chemical vapor deposition. *Journal of applied physics* **2006**, *100* (10), 104321.

(9) Kireš, M. Archimedes' principle in action. Physics education 2007, 42 (5), 484.

(10) Orbaek, A. W.; Owens, A. C.; Barron, A. R. Increasing the efficiency of single walled carbon nanotube amplification by Fe–Co catalysts through the optimization of CH4/H2 partial pressures. *Nano letters* **2011**, *11* (7), 2871-2874.

(11) VM, S.; Mohamed, A. R.; Abdullah, A. Z.; Chai, S.-P. Role of reaction and factors of carbon nanotubes growth in chemical vapour decomposition process using Methane—a highlight. *Journal of Nanomaterials* **2010**, *2010*.

(12) Omega. Users guide - FMA 5400/FMA 5500 Mass Flow Controllers. **2022**.

(13) Rousson, V.; Goşoniu, N. F. An R-square coefficient based on final prediction error. Statistical Methodology 2007, 4 (3), 331-340.

(14) Tsuji, T.; Hata, K.; Futaba, D. N.; Sakurai, S. Additional obstacles in carbon nanotube growth by gas-flow directed chemical vapour deposition unveiled through improving growth density. *Nanoscale Advances* **2019**, *1* (10), 4076-4081.

(15) Dresselhaus, M. S.; Dresselhaus, G.; Saito, R.; Jorio, A. Raman spectroscopy of carbon nanotubes. Physics reports 2005, 409 (2), 47-99.

(16) Albrecht, A. C. On the theory of Raman intensities. *The Journal of chemical physics* **1961**, *34* (5), 1476-1484.

(17) Little, R. B. Mechanistic aspects of carbon nanotube nucleation and growth. *Journal of Cluster Science* **2003**, *14* (2), 135-185.

(18) Swartzendruber, L. The Fe (iron) system. *Bulletin of Alloy Phase Diagrams* **1982**, *3* (2), 161-165.

(19) Shi, R.; Wang, C.; Wheeler, D.; Liu, X.; Wang, Y. Formation mechanisms of self-organized core/shell and core/shell/corona microstructures in liquid droplets of immiscible alloys. *Acta materialia* **2013**, *61* (4), 1229-1243.

(20) Wei-Su, C.; Yang, W.; Jun-Ming, G.; Feng-Jiao, H. Thermal stability of Ni-Fe alloy foils continuously electrodeposited in a fluorborate bath. *Open Journal of metal* **2012**, *2012*.

(21) Turgut, Z.; Huang, M.-Q.; Gallagher, K.; McHenry, M.; Majetich, S. Magnetic evidence for structural-phase transformations in Fe-Co alloy nanocrystals produced by a carbon arc. *Journal of applied physics* **1997**, *81* (8), 4039-4041.

(22) Zhao, Y.; Guan, J.; Liu, F.; Cheng, C.; Zhao, J. Effect of Surface Fe-Sn Intermetallics on Oxide Films Formation of Stainless Steel in High Temperature Water. *High Temperature Materials and Processes* **2018**, *37* (4), 387-395.

(23) Grigorieva, T.; Kovaleva, S.; Senyut, V.; Vityaz, P.; Lyakhov, N. Thermobaric Sintering of Mechanocomposites of the System Fe-Ga.

(24) Wang, P.; Zhao, J.; Du, Y.; Xu, H.; Gang, T.; Fen, J.; Zhang, L.; He, C.; Liu, S.; Ouyang, H. Experimental investigation and thermodynamic calculation of the Fe–Mg–Mn and Fe–Mg–Ni systems. *International Journal of Materials Research* **2011**, *102* (1), 6-16.

(25) Sina, H.; Corneliusson, J.; Turba, K.; Iyengar, S. A study on the formation of iron aluminide (FeAl) from elemental powders. *Journal of Alloys and Compounds* **2015**, *636*, 261-269.

(26) Chipman, J. Thermodynamics and phase diagram of the Fe-C system. *Metallurgical and Materials Transactions B* **1972**, *3* (1), 55-64.

(27) Sheludyakov L.N., Y. K. y. G., & Lyubimova L.S. **Izv. Akad. Nauk Kaz. SSSR, Ser. Khim**. **1961**, *1* (60-62).

(28) Fuwa, T.; Fujikura, M.; Matoba, S. Effect of elements on the solubility of graphite in liquid iron. *Tetsu to Hagane (J. Iron Steel Inst. Jpn.)* **1960**, *46*, 235-237.

(29) Mori, T.; Aketa, K.; Ono, H.; Sugita, H. Effect of elements on the solubility of graphite in liquid iron. *Tetsu to Hagane (J. Iron Steel Inst. Jpn.)* **1960**, *46*, 1429-1437.

(30) J., K. P.; J., C. *Trans. AIME* **1956**, *206*, 1102-1111,1104.

(31) E., S.; D., K. *Giessereijorschung* **1969**, *21, (1)*, 33-47.

(32) Daines, W. L.; Pehlke, R. D. *The influence of temperature and alloying elements on the solubility of graphite in liquid cobalt*; 1964.

(33) Turkdogan, E. Thermodynamics of carbon dissolved in iron alloys. *J. Iron and Steel Inst.* **1956**, *5*, 69-72.

(34) Miller, K. O.; Elliot, J. F. *Trans. AIME* **1960**, *218* (900-910).

(35) Ward, R. G.; Wright, J. A. *J. Iron Steel Inst.* **1960**, *194* (304-306).

(36) Mori, T.; Ogasawara, T.; Hasegawa, H.; Yamada, T. The effects of nickel, phosphor and tin on the solubility of graphite in liquid iron. *Suiyokwai-shi* **1962**, *14*, 387-392.

(37) Schenck, H.; Frohberg, M. G.; Steinmetz, E. *Arch. Eisenhiittenwes.* **1963**, *34 (1)*, 37-42.

(38) Gupta, V.; Patra, M. K.; Shukla, A.; Saini, L.; Songara, S.; Jani, R.; Vadera, S. R.; Kumar, N. Synthesis of core–shell iron nanoparticles from decomposition of Fe–Sn nanocomposite and

studies on their microwave absorption properties. *Journal of Nanoparticle Research* **2012**, *14* (12), 1-10.

(39) Schneider, A.; Sauthoff, G. Iron Aluminium Alloys with Strengthening Carbides and Intermetallic Phases for High-Temperature Applications. *Steel research international* **2004**, *75* (1), 55-61.

(40) Blanchard, E. R.; Mckenna, F. E. Production of carbide product and methylacetylene. Google Patents: 1956.

(41) Zhang, R.; Kong, X.; Wang, H.; Zhang, S.; Legut, D.; Sheng, S.; Srinivasan, S.; Rajan, K.; Germann, T. C. An informatics guided classification of miscible and immiscible binary alloy systems. Scientific reports 2017, 7 (1), 1-12.

(42) Zhang, R.; Kong, X.; Wang, H.; Zhang, S.; Legut, D.; Sheng, S.; Srinivasan, S.; Rajan, K.; Germann, T. C. An informatics guided classification of miscible and immiscible binary alloy systems. Scientific reports 2017, 7 (1), 1-12. Chen, Y.; Liu, F.; Yang, G.; Xu, X.; Zhou, Y. Rapid solidification of bulk undercooled hypoperitectic Fe–Cu alloy. Journal of Alloys and Compounds 2007, 427 (1-2), L1-L5.

(43) Sina, H.; Corneliusson, J.; Turba, K.; Iyengar, S. A study on the formation of iron aluminide (FeAl) from elemental powders. Journal of Alloys and Compounds 2015, 636, 261-269.

(44) Khoshhal, R.; Hossein Zadeh, A. The formation mechanism of iron aluminide phases in Fe-Al system with different raw materials ratio. AUT Journal of Mechanical Engineering 2020, 4 (3), 407-414.

(45) Guizani, C.; Sanz, F. J. E.; Salvador, S. The nature of the deposited carbon at methane cracking over a nickel loaded wood-char. *Comptes Rendus Chimie* **2016**, *19* (4), 423-432.

(46) Kukovitsky, E.; L'vov, S.; Sainov, N. VLS-growth of carbon nanotubes from the vapor. *Chemical Physics Letters* **2000**, *317* (1-2), 65-70.

(47) Wirth, C. T.; Bayer, B. C.; Gamalski, A. D.; Esconjauregui, S.; Weatherup, R. S.; Ducati, C.; Baehtz, C.; Robertson, J.; Hofmann, S. The phase of iron catalyst nanoparticles during carbon nanotube growth. *Chemistry of Materials* **2012**, *24* (24), 4633-4640.

(48) Hofmann, S.; Csanyi, G.; Ferrari, A.; Payne, M.; Robertson, J. Surface diffusion: the low activation energy path for nanotube growth. *Physical review letters* **2005**, *95* (3), 036101.

(49) Levchenko, E. V.; Evteev, A. V.; Belova, I. V.; Murch, G. E. Carbon diffusion in cementite: a molecular dynamics study. In *Defect and Diffusion Forum*, 2009; Trans Tech Publ: Vol. 283, pp 24-29.

(50) Orbaek, A. W.; Owens, A. C.; Crouse, C. C.; Pint, C. L.; Hauge, R. H.; Barron, A. R. Single walled carbon nanotube growth and chirality dependence on catalyst composition. *Nanoscale* **2013**, *5* (20), 9848-9859.

(51) He, M.; Chernov, A. I.; Fedotov, P. V.; Obraztsova, E. D.; Sainio, J.; Rikkinen, E.; Jiang, H.; Zhu, Z.; Tian, Y.; Kauppinen, E. I. Predominant (6, 5) single-walled carbon nanotube growth on a copper-promoted iron catalyst. *Journal of the American Chemical Society* **2010**, *132* (40), 13994-13996.

(52) Shahi, F.; M.A., P. The Effect of Growth Temperature on Characteristics of Carbon nanotubes Catalyzed by Sol–gel Prepared Fe–Co/TiO2 Catalysts via TCVD. In 3th International Engineering Materials & Metallurgy Conference, Shahid Beheshti Conference Center, Tehran, Iran; 2014.

(53) Rezaee, S.; Ghaderi, A.; Boochani, A.; Solaymani, S. Synthesis of multiwalled carbon nanotubes on Cu-Fe nano-catalyst substrate. *Results in physics* **2017**, *7*, 3640-3644.

(54) Sengupta, J.; Jacob, C. The effect of Fe and Ni catalysts on the growth of multiwalled carbon nanotubes using chemical vapor deposition. *Journal of Nanoparticle Research* **2010**, *12* (2), 457-465.

(55) Tran, K. Y.; Heinrichs, B.; Colomer, J.-F.; Pirard, J.-P.; Lambert, S. Carbon nanotubes synthesis by the ethylene chemical catalytic vapour deposition (CCVD) process on Fe, Co, and Fe–Co/Al2O3 sol–gel catalysts. *Applied Catalysis A: General* **2007**, *318*, 63-69.

(56) Kathyayini, H.; Nagaraju, N.; Fonseca, A.; Nagy, J. Catalytic activity of Fe, Co and Fe/Co supported on Ca and Mg oxides, hydroxides and carbonates in the synthesis of carbon nanotubes. *Journal of Molecular Catalysis A: Chemical* **2004**, *223* (1-2), 129-136.

(57) Pham, Q. N.; Larkin, L. S.; Lisboa, C. C.; Saltonstall, C. B.; Qiu, L.; Schuler, J. D.; Rupert, T. J.; Norris, P. M. Effect of growth temperature on the synthesis of carbon nanotube arrays and amorphous carbon for thermal applications. *physica status solidi (a)* **2017**, *214* (7), 1600852.

(58) Crichton, T.; Farr, J. The Effect of Heat Treatment on the Fe—Sn Alloy System. *Transactions of the IMF* **2004**, *82* (5-6), 169-173.

(59) Turkevych, V.; Rumiantseva, Y. Y.; Hnatenko, I.; Hladkyi, I.; Sadova, Y. I. Thermodynamic Calculation of Fe–N and Fe–Ga Melting Diagrams at Pressures from 0.1 MPa to 7 GPa. *Progress in Physics* **2021**, (4), 531-538.

(60) Eleya, N.; Appiah, C.; Lork, E.; Gogolin, M.; Gesing, T. M.; Stauch, T.; Staubitz, A. Synthesis and Thermal Investigations of Eleven-Membered Ring Systems Containing One of the Heavier Group 14 Element Atoms Si, Ge, and Sn. *Molecules* **2020**, *25* (2), 283.

(61) Li, D.; Pan, L. Growth of carbon nanocoils using Fe–Sn–O catalyst film prepared by a spin-coating method. *Journal of Materials Research* **2011**, *26* (16), 2024-2032.

(62) Kaneko, A.; Yamada, K.; Kumahara, R.; Kato, H.; Homma, Y. Comparative study of catalytic activity of iron and cobalt for growing carbon nanotubes on alumina and silicon oxide. *The Journal of Physical Chemistry C* **2012**, *116* (49), 26060-26065.

(63) Fazle Kibria, A.; Mo, Y.; Nahm, K. Synthesis of carbon nanotubes over nickel–iron catalysts supported on alumina under controlled conditions. *Catalysis letters* **2001**, *71* (3), 229-236.

(64) Akbarzadeh, O.; Mohd Zabidi, N. A.; Abdul Wahab, Y.; Hamizi, N. A.; Chowdhury, Z. Z.; Merican Aljunid Merican, Z.; Ab Rahman, M.; Akhter, S.; Rasouli, E.; Johan, M. R. Effect of cobalt catalyst confinement in carbon nanotubes support on fischer-tropsch synthesis performance. *Symmetry* **2018**, *10* (11), 572.

(65) Li, Y.; Cui, R.; Ding, L.; Liu, Y.; Zhou, W.; Zhang, Y.; Jin, Z.; Peng, F.; Liu, J. How catalysts affect the growth of single-walled carbon nanotubes on substrates. *Advanced Materials* **2010**, *22* (13), 1508-1515.

Chapter 3

Theoretical analysis of growth environment using Boltzmann BGK model

3.1   Introduction of the BGK simulation of carbon nanotube geometry

Computational Fluid Dynamics (CFD) is a branch of computer-aid engineering that utilises numerical analysis to solve complex gaseous problems in fluid dynamics[1]. The ambitious goal for this project is to grow ultra-long carbon nanotubes (UL-CNTs) from centimetre (cm) to kilometre long (km) in the actual experiments, for the applications such as long-range electricity transmission and high-strength carbon nanotube cables in the future. The chemical aspects of growing carbon nanotubes, such as using monometallic and bimetallic catalysts to grow UL-CNTs mentioned in the previous section, have been in existence for a long time and proved successful in the scientific community[2,3]. The further study of this work is to advance the use of bimetallic catalysts to grow ultra-long carbon nanotubes. The study of computational modelling of carbon nanotube, such as the molecular dynamics (MD) of continuous carbon nanotubes structure by the diffusion of carbon atoms to form carbon nanotube[4] and investigate the flow arrangement on CNT growth using commercial CFD simulation package, such as COMSOL[5], have become a level of resource availability in the recent research. However, such findings have mainly focused on the formation of carbon molecules and mostly dealt with the fluid-solid interactions in the continuum physics. It is unclear how the non-continuum approach such as molecular collisions and physical arrangements in microscale such as the variations of velocity and temperature, would affect the ultra-long carbon nanotubes (UL-CNTs) growth in the computational modelling. Along with the conducted experimental work, this project would offer some important insights into ultra-long carbon nanotube growth. The flow simulations were calculated using the Boltzmann-BGK equation by the approach of Taylor-Galerkin method. In this simulation study, various flow sccm from 1 to 1000 (1, 10, 30, 100 & 1000 sccm) and the commonly reaction temperatures for the CNT growth of 850, 950 & 1012 °C (1123 K, 1223 K & 1285 K) will be studied. The geometry of the two-dimensional space, a 1 nm width UL-CNT of ~3 mm length is connected at one end on a 2 mm height substrate of 1.5 cm length will be used for the simulation study. The average ratio of the gas molecules, hydrogen (H_2) and methane (CH_4) pass by a carbon nanotube geometry and the model simulates how the gas molecules act on the wall of carbon nanotube, the Knudsen number (Kn) is ranged from 343 to 392 in the collisionless region. This project investigates the drag force of microfluid under the microscale modelling around the

geometry of a carbon nanotube at a static state. The microfluidic modelling capabilities were completed by the high-performance computer (HPC) at Swansea University. The achievement of this work is to find the critical velocity magnitudes and temperature conditions for the UL-CNTs growth, and the objective of this project is to optimise the gas flow and temperature and apply the settings to the actual experiment grow ultra-long Carbon Nanotubes (UL-CNTs). In conclusion, it is found that high flow sccm is more desirable over low flow sccm for UL-CNTs growth as a more uniform distributed pressure imparted on either wall of the nanotube.

3.2   Background information and governing equations

The BGK-Boltzmann equation described the non-equilibrium state of distribution of molecules and particles collisions in an enclosed system[6]. The equation describes the rarefied gases and a non-equilibrium state of a thermostatic system by using the discontinued Taylor Galerkin method for unstructured grids[7], which the discretisation solution is achieved by incrementing a step-by-step steady state to reach a full-steady state solution. The molecule-surface and intermolecular interactions can be simulated using this discontinuous method. In this gas molecular collision model, the fluid phase is regarded as individuals' particles rather than a continuous fluid at the molecular dynamic level. The microscopic force acting on a particle are commonly known as thermal, mechanical, and chemical force, whilst the first two forces (thermal, mechanical) will be examined in this simulation. The mechanical force, also the viscous force describes the diffusion in a closed system whereas the thermal force is the molecular collisions with each particle. In conclusion, the Boltzmann equation allows without establishing a complicated relationship as a direct method in the continuum approach. The definition of Boltzmann-BGK equation can be explained by the following equation[8]:

$$\frac{\delta(nf)}{\delta t} + c.\frac{\delta(nf)}{\delta r} + F.\frac{\delta(nf)}{\delta c} = v\,(r,t)((nf_0) - (nf)) \qquad (1)$$

$V = f\,(r\,,c\,,t)$ is the molecular velocity distribution function across physical space, in which r represents the two-dimensional position of vector, c represents the two-dimensional molecular velocity vector, n is the molecular number density and t is the time. The modelling method only focuses on mechanical and thermal method in a low Reynolds (Re) number region, F describes the force that might be present in the system, for example: gravitational force. Since it is assumed that there is no additional force in the system, this force is ignored. $v\,(r\,,t)$ is the molecular collision frequency and f_0 is the local Maxwellian equilibrium distribution function

Knudsen number (Kn) is the parameter that describes mean free path of molecule to a characteristic length determining the degree of rarefaction of the gas[9]. In this modelling, the Knudsen number is based on the width of the nanotube as the reference length scale. The gas stream was modelled in a microscopic scale.:

$$Kn = \frac{\lambda}{L} \qquad (2)$$

λ= mean free path of molecules in the flow

L = length of the flow

The mean free path (λ) in the above equation (2) can be denoted by:

$$\lambda = \frac{kT}{\sqrt{2}\pi d^2 p} \qquad (3)$$

k= Boltzmann constant (1.38×10^{-23} J/K)

T= gas temperature (K)

d = molecular diameter (pm)

p = gas pressure (1×10^{-5} Pa)

3.3   Method and setting the physical conditions

The diagram illustrates the horizontal chemical vapour deposition process within quartz tubes (figure 3.1 a). The model is a 100 mm width x 20 mm height gas channel, with the gas inlet and the gas outlet. An UL-CNT of 1 nm diameter is tethered to a 30 mm length x 2 mm width silicon wafer located at the middle of the gas domain. The volume flow rates (1, 10, 30, 100, 1000 sccm) were simulated with the applied temperature of (1123 K, 1223 K & 1285 K) on the wall boundaries and in the gas domain at the same temperature in an isothermal condition. The feeding gases are hydrogen (H_2) and methane (CH_4) in the system, however given the complexity of modelling the interaction of two gases in the system, the ratio of the gas (H_2/ CH_4) is assumed homogenous, in 2:1 ratio. The growth of ultra-long carbon nanotubes (UL-SWCNTs) implies that the SWCNTs are subjected to the nanofluid around the carbon nanotube. The experimental diagram (figure 3.1 a) illustrates the one end of SWCNT is anchored on the substrate and the free end is airborne. The catalytic growth of carbon nanotube, either by tip growth or base growth, must be maintained to become a centimetre long during the participation phase of carbon nanotube. The termination of carbon nanotube growth can be attributed to the tip of the carbon nanotube contacting the surface of a substrate. The image is

a carbon nanotube in 10 μm length under scanning electron microscope (SEM) (figure 3.1 b), it shows that the nanotube grows from a catalyst (base growth). Finally, the images at the bottom are the illustration of the generated meshes of the gas domain, a substrate, and a carbon nanotube geometry (figure 3.1 c) and the magnified geometry of carbon nanotube in 1 nm width and ~3 mm length (figure 3.1 d). The meshes were refined at the tip of the nanotube geometry to capture the flow behaviours more precisely. The scalability to overcome geometry differences of 1nm (width of nanotube) and 3mm (length of nanotube) in this simulation was described by the work by Ho (2019) showing the restrictions of scalability due to the requirements of computational viability for more complex geometries[10]. The restricted structural physical space grids can be scaled to multiple cores, the scale-up mesh size with a smaller number of grids can be compensated by parallisation – in which the computing carries out the processes simultaneously. The scalability of the grid is important to ensure the condition to match the corresponding grids, with the specific aim to reduce the computational resources for measuring each set of conditions.
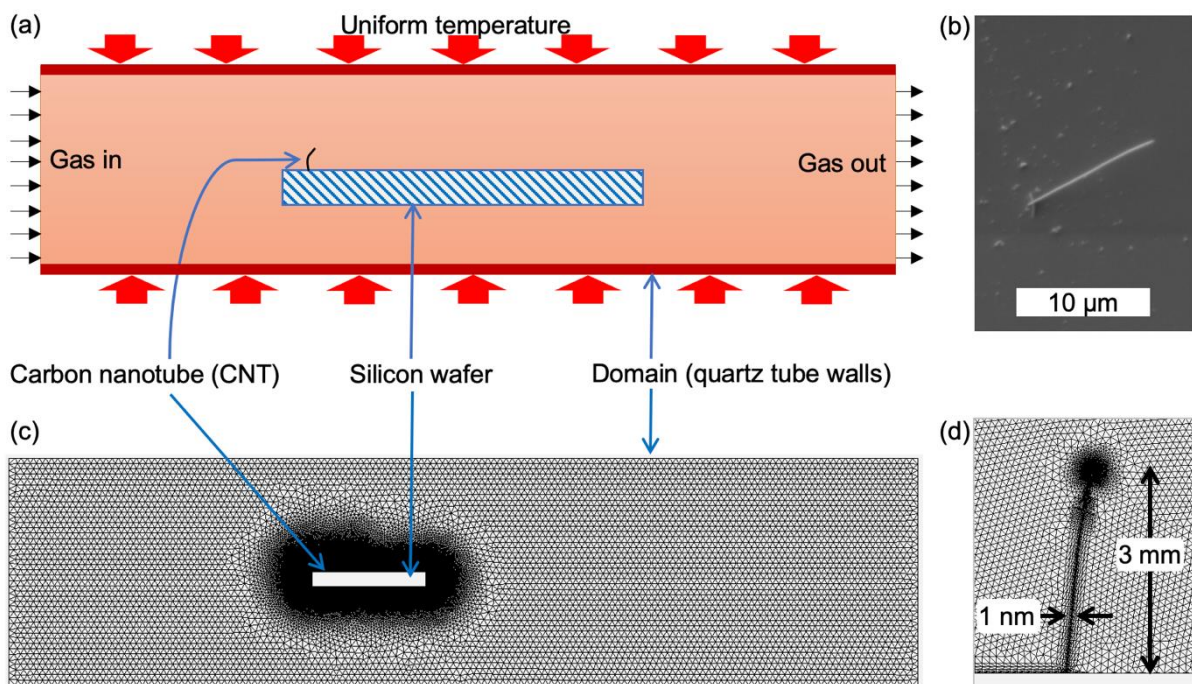
Figure 3.1. (a) Schematic illustration depicting an ultralong carbon nanotube growing from the surface of a silicon substrate in a uniform temperature gas domain, (b) the physical experiment of a UL-CNT growing from the surface under SEM, (c) the generated meshes in the computational simulation (d) the enlarge image of carbon nanotube geometry with meshes

The wall absorption fraction (α) describes the molecules absorption of the wall and then remitted from the wall in an equilibrium state. The remaining fraction, (1-α), is not absorbed by the wall and remits to the fluid domain, which is called "specular reflection". In this simulation, the wall parameter was set to 0.9, which indicates that some level of gas molecules would bounce back from the wall. This is the emission of the particle from the wall after absorption which the parameter is based on the recommendation by J.C. Maxwell [11], The boundary condition of the domains including inflow, outflow & wall have been defined for the conditional parameters. The inflow is assumed that in thermodynamic equilibrium, outflow is zero perpendicular to the boundary and the wall absorption of the wall and remit the particle in the domain[12]. The classic Naiver-stokes equation only focuses on the velocity, pressure, temperature & density with "no slip" condition[12]. The BGK equation, the particle would bounce back from the wall (absorption). The fluid-wall interactions. By the wall values (f) – molecular wall absorption parameters. These boundaries are described below:

1) Inflow: the inflow of gas entre from surroundings to the domain of physical space remain thermodynamic equilibrium described by Maxwellian distribution with the equation

$$F_{n,c}^{m+\frac{1}{2}} = c.n\left(\frac{\beta^2}{\pi}\right)\exp\left(-\beta^2(c-c_0)\right) \tag{4}$$

$F_{n,c}^{m+\frac{1}{2}}$ denotes the normal component of the upstream flux at the physical space element edges for a velocity $\left(\frac{\beta^2}{\pi}\right)\exp\left(-\beta^2(c-c_0)\right)$ is the two-dimensional Maxwellian distribution function, and the equation can be rearranged to the inter-element flux if the molecular velocity is directed out of the element:

$$F_{n,c}^{m+\frac{1}{2}} = \frac{1}{2}c.n((nf)_1^{m+\frac{1}{2}} + (nf)_2^{m+\frac{1}{2}}) \tag{5}$$

2) Outflow: the outflow is the gradient of the molecules and perpendicular to the boundary in zero if the outflow is based on the bulk flow at boundary, and can also written as:

$$F_{n,c}^{m+\frac{1}{2}} = \frac{1}{2}c.n((nf)_1^{m+\frac{1}{2}} + (nf)_2^{m+\frac{1}{2}}) \tag{6}$$

3) Wall: the collision with the wall is assumed that the absorption of the wall and remittance from the wall in equilibrium with zero mass flux in kinetic

$$\int_{\tau_r} \int_{-\infty}^{+\infty} F_{n,c} \, dc \, d\tau_r = 0 \tag{7}$$

In the equation, the $F_{n,c} = (c \cdot n) f(r \cdot c \cdot t)$ and τ_r are the boundary domains of physical space (p-space). It ensures that the molecular collisions with the wall are described by appropriate parameters.

The definition of parameters for equation (5), (6) & (7):

f = distribution function defined over physical space and velocity space (and time)

r = position vector in physical space

c = position vector in velocity space

c_0 = bulk velocity of the flow

n = molecular number density of gas

m = molecular mass

$\beta = (2RT)^{-\frac{1}{2}} = \sqrt{\frac{m}{2kT}}$. R is the universal gas constant. T is the gas temperature measured in Kelvin, m is molecular mass and k is the Boltzmann constant (1.38×10^{-23} J/K)

3.4 Creating and scaling the dimensional framework

The chemical reaction ($CH_4 \rightarrow C + 2H_2$), methane produces additional hydrogen and carbon atoms then form carbon nanotubes which activated by the catalytic particles at the leading edge of the substrate. The Knudsen number (Kn) (table 3.2) and Reynold's number (Re) (table 3.3) for this study were calculated using the parameters from the properties of homogenous gas of Hydrogen (H_2) & Methane (CH_4) in 2:1 ratio (table 3.1). Given the complexity of simulating two species of gas molecules collisions, the average density by ratio of both gases in this simulation. The diameter, density at standard atmosphere pressure (atm) & average dynamic viscosity of the Hydrogen (H_2) & Methane (CH_4) in a 2:1 ratio are 319 (pm), 0.27367 (kg/m^3) & 2.07 x 10^{-5} (kg/m.s) respectively as shown in table 3.1, which obtained from the data of properties of methane (CH_4) and hydrogen (H_2).

Table 3.1. Physical Properties of reaction gasses

Physical Property	Gas species		
	H_2	CH_4	$H_2:CH_4$
Molecular diameter (pm)	289	380	319
Density at standard atmospheric pressure (kg/m^3)	0.2143	0.02693	0.27367
Average dynamic viscosity (kg/m.s)	2.53×10^{-5}	1.84×10^{-5}	2.07×10^{-5}
Gas constant	4124	518.3	n/a

In figure 3.2, the Boltzmann equation/ collisionless Boltzmann cover a wider range of local Knudsen number from 0 to infinite (∞) for the discrete particle/ molecular model. Compared to the scale to the Euler & Navier-stokes equation, it only covers a narrow range of numbers (from 0 to ~1) in the continuum model. As compared to the Navier-Stoke equation, the Boltzmann equation provides more details description of the gas behaviour from continuum to rarefied state. A full range of Knudsen number include from continuum flow (0.0001 < Kn < 0.001), Slip flow (0.0001 < Kn < 0.1), Transition flow (0.1 < Kn < 10) to Free-molecular flow (Kn > 10)[9]. Regarding the Knudsen number (Kn) and simulation of carbon nanotube geometry in the work, the gas molecules are the average diameter ratio of H_2/ CH_4 (2:1) particles (319 nm) and the physical reference length is the width of the nanotube (in 1 nm). The Knudsen numbers (Kn) are 343 (at 1123K), 373 (at 1223 K) & 392 (at 1285 K) in table 3.2, which are in the collisionless region (from 100 to ∞).
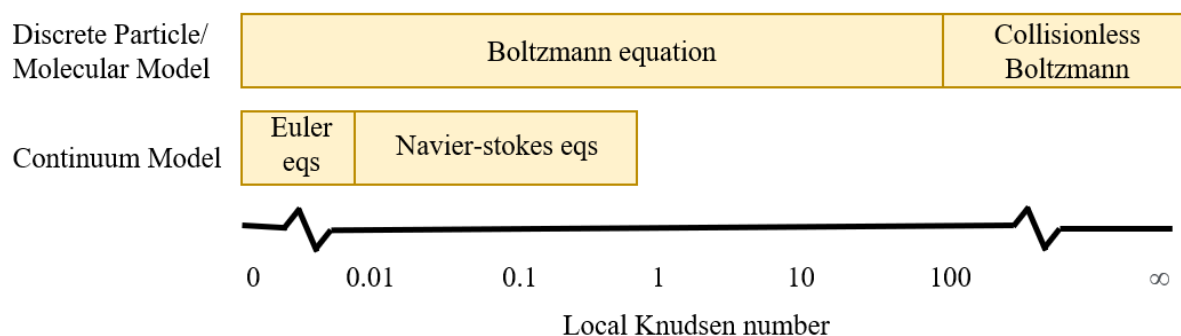
Figure 3.2. Illustration of local Knudsen number (Kn) by Boltzmann equation (discrete particle/ molecular model) and Navier-stokes equation (continuum model)

Table 3.2. Knudsen number (Kn) for 1123 K, 1223 K & 1285 K using nanotube diameter as the reference length

	Temperature (K)		
	1123	1223	1285
Knudsen number (Kn)	343	373	392

The Reynold's numbers (Re) are ranged from 6.55×10^{-11} to 7.85×10^{-8} (for 1, 10, 30, 100, 1000 sccm) listed in table 3.3. These ultra-low values indicate a highly laminar flow around the carbon nanotube geometry, yet a relatively small scale of vortexes may generate from the boundary layer can cause instability of the flow patterns under an ultra-low Reynold's number region (Re $< 1 \times 10^{-4}$).

Table 3.3. Reynolds' number (Re) at different gas velocities using nanotube diameter as the reference length

	Reynolds' number		
	1123 K	1223 K	1285 K
1	7.50×10^{-11}	6.88×10^{-11}	6.55×10^{-11}
10	7.79×10^{-10}	7.16×10^{-10}	6.81×10^{-10}
30	2.35×10^{-9}	2.16×10^{-9}	2.06×10^{-9}
100	7.86×10^{-9}	7.21×10^{-9}	6.87×10^{-9}
1000	7.85×10^{-8}	7.21×10^{-8}	6.89×10^{-8}

A typical simulation power in this study requires at least 6 cores and approximately 72 hours in total to handle the complex computing tasks in this study, using the Boltzmann-BGK equation and a High-Performance Computer (HPC) cluster was employed. In the computational modelling, the wall and domain temperature are assumed equivalent in a thermal equilibrium condition. The setup temperatures in the model are based on the common values for UL-SWCNTs growth. The characteristic pressures and flow patterns at the tip of the UL-SWCNTs can be viewed by comparing the upstream and the downstream of the CNT, subsequently the resulting velocity, pressure fields and net forces acting on the nanotube can be calculated.

3.5 BGK Boltzmann solver system

The Boltzmann-BGK solver file system consisted of 4 stages (refer to section 3.11 Supporting information - Boltzmann-BGK solver file system): (1) Mesh generation, (2) Pre-processing, (3) Solver and (4) post-processing. It is the commands to instruct the cluster system to process numerical data. The "PSPACEMESHGEN" stands for 'mesh generation of the physical space', which is a programme that converts the geometry and mesh spacing files to the readable data in the code, based on Delaunay triangulation[13]. The PSPACEMESHGEN, METIS, BGK & ENSEG_BOLTZMANN are assigned in each stage. In mesh generation, .dat (geometry definition) and. bac (mesh spacing) are generated from the MATLAB file. The plt. (Mesh file) &. con (connectivity) files were then created subsequently. In the second stage of pre-processing, the METIS is to convert the connectivity to physical spaces, which is the nodal partition. Then, the BGK solver, with the solver inputs, these input parameters include the wall reflection parameter, domain & inflow temperature, pressure & velocity. Before summiting the files to the cluster system. After the reached calculation time, the result files contain the data of overall residual values (RESIDUAL.RES), residual lift force (RESULTS1.RES) and drag force (RESULTS2.RES). The RESULTS1.RES and RESULTS2.RES contain the information of the actual lift and drag force value. And at the final stage of ENGEN_BOLTZMANN, the result files will be converted to the virtualisation of Ensight file. Ensight is the software that gives the virtualisation of the simulation results. The BGK Boltzmann solver system id shown in the additional information.

3.6 Mesh convergence studies

The velocity space (v-space) & physical space (p-space) are the main parameters that define the discretisation of Boltzmann-BGK solution[14]. The two-dimensional velocity space (v-space), the p-space domain (Ω_r), provides the constrain of the molecules at s maximum velocity within the radius (r_v) in the domain in the partition (in figure 3.3 a). The physical space (p-space), which forms with unstructured discontinues triangular elements (in figure 3.3 b), providing a straight-forward parallelisation that can be naturally capture the solution discontinuities such as shock waves from the molecular collisions by the discretisation approach. The METIS is a tool that is used for parallelisation and the communication requirements can be reduced between each edge of the element for p-space mesh[15]. The number of meshes have been classified as coarse, medium, fine & superfine for physical space (p-

space), based on the number of elements defined. The numbers of elements to be 14808, 23324, 55628 & 81375 (with 29047, 45840, 109930, 161018 for discontinuous nodes accordingly) for coarse, medium, fine, and super fine grids, respectively. Lobatto quadrature is a refinement algorithm for parallelisation which described by Evan[14], which is a weighting function that transforming continuous variables or models into a discrete form. The combinations of velocity space (v-space) and physical space (p-space) form the Lobatto quadrature of 10×10, 20×20, 30×30, 40×40, 80×80, 120×120 & 160×160 have been established. A higher Lobatto quadrature can capture flow field more precisely but with higher computational power; nevertheless, a lower Lobatto quadrature may not be enough to provide enough resolution power. Hence, it is a balance to find the optimal Lobatto quadrature for the data visualisation. The following matrix of Lobatto quadrature in terms of lift force, drag force, computational requirements, and accuracy/ core hour required will be explained (from table 3.5 - 3.7). It is found that with no solution across the 10 x 10 across all sizes of meshes and for the coarse meshes of 20 x 20 for the lift force and drag force, the values in the brackets indicate the error of the percentage of lift force and drag force. The error percentage for lift force are from 0 % – 6750 % (table 3.5) and the drag force from 0 % – 49 % (table 3.6). For example: the 6750% for Lobatto 20×20 (superfine) indicates that this condition is not suitable for use due to its large absolute error. The computational requirements for velocity space (v-space) and physical space (p-space) are shown (table 3.7), which is truth a higher Lobatto quadrature orders with denser meshes will take longer core hours for the convergence. The convergence solutions indicate the direction towards zero with predicable results. In conclusion, the accuracy/ core hours required combined with the study from each parameter above. There were divergences (with no stable solutions) across the first row of Lobatto 10 x 10 and the Lobatto 20 x 20 at coarse mesh.
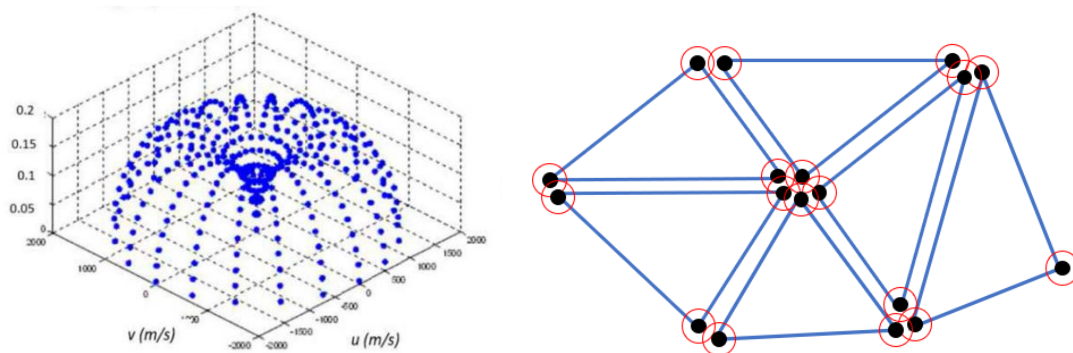
Figure 3.3. (a) velocity space (v-space) and (b) physical space (p-space) represents in the meshes

In conclusion, the four conditions of Lobatto 80 x 80 & 120 x 120 (which highlighted with *) are the best settings in terms of the errors and the computational time required. From the results above shown that less errors of lift and drag force completed with the higher order of Lobatto quadrature and mesh size, in contrast it will require a higher computational power. In summary, with all the considerations with computational requirements and percentage of errors, the 80 x 80 (fine meshes) were chosen for the following simulations.

Table 3.4. Lift force (in Newton) in velocity space (v-space) and physical space (p-space) and the percentage error (%) in bracket

Lobatto	Coarse (NP: 27555)	Medium (NP: 72690)	Fine (NP: 109930)	Super fine (NP: 174804)
10 x 10	No solution	No solution	No solution	No solution
20 x 20	No solution	-8.1e-5 (523 %)	-5.5e-4 (4130 %)	-8.9e-4 (6750 %)
40 x 40	-5.4e-5 (315 %)	2.4e-5 (285 %)	-5.5e-5 (4130 %)	1.6e-4 (1330 %)
80 x 80	-2.7e-5 (108 %)	-1.1e-5 (15 %)	-1.3e-5 (0 %)	4.9e-5 (477 %)
120 x 120	-2.7e-5 (108 %)	-1.2e-5 (8 %)	-1.3e-5 (0 %)	-1.3e-5 (0 %)
160 x 160	-2.5e-5 (92 %)	-1.2e-5 (8 %)	-1.3e-5 (0 %)	-1.3e-5 (0 %)

Table 3.5. Drag force (in Newton) in velocity space (v-space) and physical space (p-space) and the percentage error (%) in bracket

Drag force (N)	Coarse (NP: 27555)	Medium (NP: 72690)	Fine (NP: 109930)	Super fine (NP: 174804)
10 x 10	No solution	No solution	No solution	No solution
20 x 20	No solution	9.8e-4 (49 %)	1.35e-3 (30 %)	1.5e3 (22 %)
40 x 40	1.88e-3 (3 %)	1.89e-3 (2 %)	1.91e-3 (1 %)	1.89e-3 (2 %)
80 x 80	1.91e-3 (1 %)	1.91e-3 (1 %)	1.92e-3 (0.5 %)	1.89e-3 (2 %)

120 x 120	1.92e-3 (0.5 %)	1.92e-3 (0.5 %)	1.93e-3 (0 %)	1.93e-3 (0 %)
160 x 160	1.92e-3 (0.5 %)	1.92e-3 (0.5 %)	1.93e-3 (0 %)	1.93e-3 (0 %)

The computational requirements for velocity space (v-space) and physical space (p-space) are listed in table 3.7. The solutions labelled with "†" imply no solution was reached or the instability of simulation. The convergence of solution requires from minimum 400 core hours (40×40, coarse) to the maximum 44,800 core hours (160×160, super fine).

Table 3.6. Computational requirements for velocity space (v-space) and physical space (p-space)

Core hours	Coarse (NP: 27555)	Medium (NP: 72690)	Fine (NP: 109930)	Super fine (NP: 174804)
10 x 10	†	†	†	†
20 x 20	†	800 core hours	960 core hours	2,560 core hours
40 x 40	400 core hours	1,120 core hours	1,920 core hours	3,840 core hours
80 x 80	1,000 core hours	4,000 core hours	8,960 core hours	11,840 core hours
120 x 120	1,000 core hours	7,600 core hours	11,520 core hours	23,040 core hours
160 x 160	1,000 core hours	12,500 core hours	15,500 core hours	44,800 core hours

† - implies no solution reached or the simulation was unstable

The accuracy/ error in percentage (%) for velocity space (v-space) and physical space (p-space) shows the accuracy of the solutions for each Lobatto setting in different mesh sizes (coarse, medium, fine & super fine) in table 3.8. The settings labelled with * are the four of the preferred settings can be used for the simulation.

Table 3.7. Accuracy/ error in percentage for velocity space (v-space) and physical space (p-space).

Accuracy/ core hours required	Coarse (NP: 27555)	Medium (NP: 72690)	Fine (NP: 109930)	Super fine (NP: 174804)
10 x 10	No solution	No solution	No solution	No solution
20 x 20	No solution	0	0	0
40 x 40	0	0	0	0
80 x 80	0	0.021*	0.011105*	0
120 x 120	0	0.012039*	0.008681*	0.00434
160 x 160	0.001953	0.00732	0.006431	0.002232

(* Preferred settings)

3.7   Results and discussion

The results for the matrix of flow sccm (1,10, 30, 100 & 1000 sccm) and temperature (1123, 1223 & 1285 K) were calculated and visualised using the Ensight software (version 2020 R2). The visualization of the results is examined (velocity, pressure) and the measurement of the value net forces, the pressure plot is the 1000 sccm in 1223 K in figure 3.4 a. It is shown that the upstream drastically push CNTs to the right along the gas flow. The close-up of carbon nanotube tip in comparison to the flow patterns for 1 sccm and 1000 sccm. At a lower flow sccm case (1 sccm, figure 3.4 b), the flows toward the centre of the tip and at a higher flow sccm (1000, figure 3.4 c) are streamlines pass the tip of the geometry with a greater value of
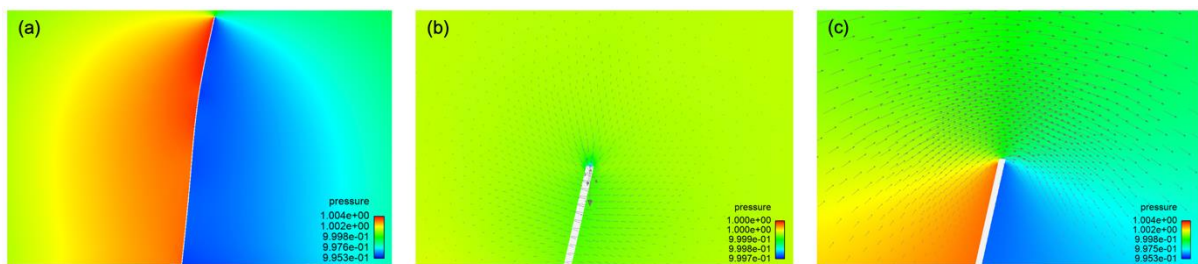

Figure 3.4. Representative pressure plot around the tip of a carbon nanotube under (a) flow velocity of 1000 sccm and temperature of 1123 K based on the model pressure (bar) that is the normalised the free stream pressure (bar), $P = P/P_0$ (P_0 is equal to 1 bar). Flow arrows comparing flow around the tip of a carbon nanotube under flow velocity of (b) 1 sccm and (c) 1000 sccm at 1123 K.

pressure and more streamlines. A comparison of these results reveals that a smooth flow is moving at a high flow velocity and more tending towards and around the CNT tip at a low flow velocity. It indicated that high flow sccm is more streamlined denoting flow of a fluid in which the velocity at any point fluctuates irregularly and there is continual mixing rather than a steady or laminar flow pattern.

3.8   Temperature effects

The diagrams (figure 3.5) below illustrate the pressure changes with the increase of flow sccm from 1, 10, 30, 100 to 1000 sccm in different temperatures from low to high temperature (1123, 1223, 1285K). From observation, most of the temperature cases are almost identical to each other. It demonstrates that little or no temperature effects on the orientation of CNT. The temperature effects for 1285K seems to be unique at lower flow rates of 10, 30, 100 sccm (figure 3.5 c, 3.5 f & 3.5 i respectively) when compared to the results of 1123K & 1223K. At 1285K, a low-pressure boundary (in blue) on above the silicon surface is presented (figure 3.5 a, b, d & e), and no longer exist and replaced by a higher-pressure boundary (in green).

Provided the negligible of pressure variables with respect to the temperature gradient (1123, 1223 & 1285K). It can be concluded that temperature has insignificant effect on the nanotube geometry. It is important to note that there is no thermal gradient throughout the entire geometry domain (wall boundary, silicon wafer & nanotube geometry). Therefore, the thermal buoyancy force with temperature variance is discarded in this study, which is commonly associated with the mechanisms of lifting the CNT from the silicon surface, and also the thermal absorption values of different materials were omitted.

3.9   Volumetric flow rate and pressure change

The figures show that from 1 sccm to 10 sccm, the nodes. The pressure changes have been observed along the wall of the nanotube, which are perpendicular to the flow direction whilst the flow velocity increase in these temperature cases. The changes in pressure intensity across different flow sccm for 1123 K are almost equivalent to the same trend for 1223 K, with differences to the 1285 K. At 1 sccm of 1123 K & 1223 K (figure 3.5 a & 3.5 b), the background pressure is green (the middle at the pressure bar) and there are 3 nodes (2 red nodes – which higher than the background pressure and 1 blue node – which lower than the background pressure and all the nodes located at the centre line of the tube geometry. The 1 sccm at 1285

K (figure 3.5 c) has several more nodes (6 nodes) than the ones in previous temperature cases. The background pressure is orange, and the nodes alternate with high (red) and low-pressure (yellow) nodes. From 10 sccm to 30 sccm for 1123 K & 1223 K cases (figure 3.5 d, e & 4 g, h), the three nodes begin drifting from their original position to the sides. The first two higher pressure nodes (red) move slightly towards the left-hand side from the tube geometry (to the leading edge), and the lower pressure node (blue) to the trailing edge. The only difference is that both high pressure nodes have merged into one with larger area coverage at 30 sccm. For 1285 K, the 10 sccm and 30 sccm cases (figure 3.5 f & 3.5 i), the pressure distributions experienced a different behaviour than the same cases to 1123 K & 1223 K, with a larger area of pressure coverage at the leading edge for 10 sccm and more at the 30 sccm at 1285 K. For all the 100 and 1,000 sccm across the 1123 K, 1223 K and 1285 K cases (figure 3.5 j – l & m-o), they have experienced a similar pressure distribution, in which the 100 sccm has a higher pressure at the top of the tube at the leading edge with lower pressure at the trailing edge. At 1000 sccm, both pressure differences become more evenly.

To establish the pressure difference in a static state model, the first and last of 15 measure points (total: 30 measure points) from upstream and downstream along the nanotube geometry were recorded. After the deduction of pressure differences between the upstream and downstream, the net pressure exerts on the forward face of CNT can be calculated. The graph shows that there has been a gradual increase in the pressure exerted on the forward face of the nanotube, for 1, 10, 30, 100 & 1000 sccm at 1123K, 1223K & 1285K. In figure 3.6, the x axis represents the flow velocity (sccm) and y axis is the pressure in mbar, both axes are in logarithmic scale. From the results, there are some similar trends across all parameters at 1123 K, 1223 K & 1285 K). Temperature has no differences on the pressure changes across all the flow sccm (1, 10, 30, 100 & 1000 sccm). The information about the density, temperature and pressure indicate that these parameters have not change dramatically and have a similar trend. Though the velocity values at 1,000 sccm have a higher pressure when compared to the other flow sccm (1, 10, 30 & 100 sccm). This indicated that the nanotube would be pushed toward the substrate and then potentially picked up by the buoyancy force even at a higher flow velocity. Further evidence of growing aligned millimetre-long carbon nanotubes at 1000 sccm (a high flow regime) from the experimental work has been proven by Zhang[16] and Quinson [17]. However, in their work, thermal buoyancy has been neglected due to the isothermal condition settings and the stationary geometry in this study, which assumes no temperature differences exists between the gas domain and substrate domain. It is also assumed that this model has

reached a thermal equilibrium state with a static heating speed, with the conventional "fast heating" with a shorter heating time as contradictory. At all flow sccm (1, 10, 30, 100 & 1000 sccm), the thermal buoyancy force in the laboratory experiments may lift the carbon nanotubes. More work to prove the case using experimental results and literature reviews could close the computational and experimental results gap.
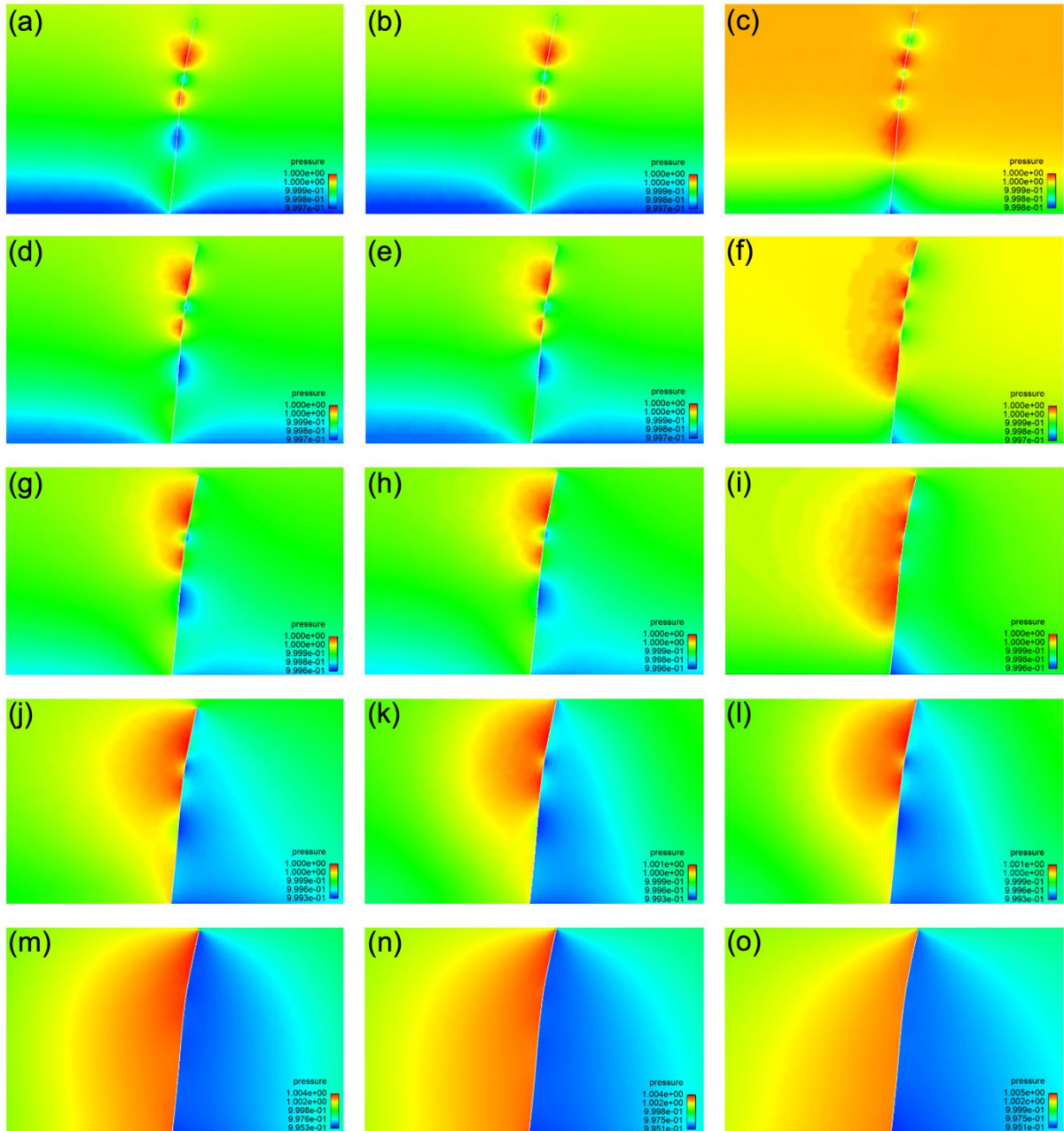
Figure 465. Pressure plot for 1123 K, 1223 K & 1285 K (in horizontal columns) and flow velocities 1 sccm, 10 sccm, 30 sccm, 100 sccm & 1000 sccm (in rows). This is the model pressure (bar) normalised to the free stream pressure (bar), P = P/ P0

It is important to note that all the simulations are static in which the nanotube geometry is stationary throughout the simulation, and the pressure differences indicate the magnitude of the flow as a reference. It can therefore be concluded that growing carbon nanotube at a higher flow sccm (1000 sccm) is preferable than at lower flow sccm (1, 10, 30 & 100 sccm) as high flow sccm promoting longer carbon nanotube growth. Compared to the number of nodes, the low flow sccm (1, 10, 30, 100 sccm, the multiple nodes) and the high flow sccm (1000 sccm, even distribution). The uneven pressure distribution along the nanotube geometry may be due to the impact of flow disturbances at a lower flow rate, and regardless of the temperature differences (1123, 1223, 1285K). From the experimental work, it was proved that a successful growth of ultra-long carbon nanotube at 1000 sccm[18]. Up to a 5.7 mm (0.57 cm) long CNT using the mixture of H_2: CH_4 (1:1 ratio) at 1000 sccm at 900 °C (1173 K) was reported. At 30 sccm, the longest carbon nanotube (1.32 cm) was produced at 950 °C with H_2: CH_4 (2:1 ratio). And finally, at ultra-low sccm (6 sccm), which between 1 – 10 sccm, the carbon nanotube was grown up to 2 cm[19].
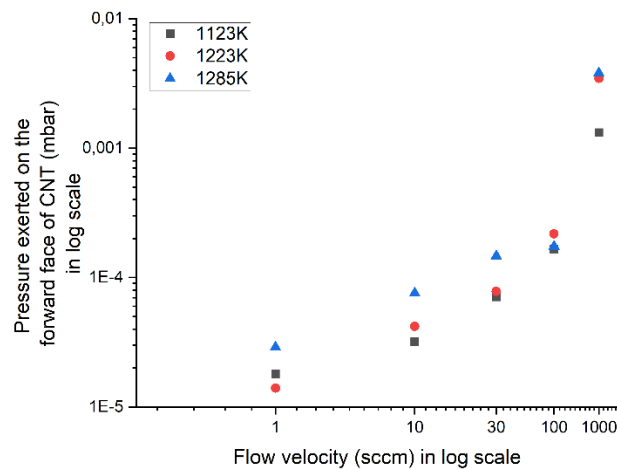
Figure 3.6. Positive pressure exerted on forward face of CNT with respect to gas velocity for 1, 10, 30, 100 & 1000 sccm at 1123 K, 1223 K & 1285 K

3.10   Conclusion

Given delivered a comparison of experimental work and nanofluids modelling on nanotube geometry, this computational work provides an illustration of velocity magnitudes and temperature differences on the pressure changes along the walls of nanotubes. This conceptual theory may help understanding the growth of ultra-long carbon nanotubes. From

the simulation, the results have shown that at high flow sccm such as 1000 sccm, more uniform pressure distributions along the sides of the nanotube. This may imply that some steady growth of carbon nanotube at a high flow rate. In opposite, at low flow sccm, such as at 1 sccm, the irregular node distributions of pressure along the wall of carbon nanotubes may result in shorter carbon nanotubes growth. The assumption made in this study is that higher flow sccm may facilitate the UL-CNTs growth, which is opposite to some literatures found suggested that the same benefits would occur by buoyancy force at low flow sccm[20,21]. In this study, however, it is assumed that a thermal equilibrium is reached in this model (which has no temperature differences between the substrate and the walls). It is suggested that the best conditions for CNT growth are at the high flow sccm (1000 sccm). A setup on the temperature differences between the carbon nanotubes and silicon substrate needs to be undertaken in the future work. This is more similar to the actual experimental setups with the additional chemical force to be added in. The contradictory results reflect that the buoyancy force is present at both high and low flow sccm –due to thermal density difference in actual cases, whilst at the high flow sccm the nanotube alignment and subsequent growth is more desirable than at the lower flow sccm.

3.11   Supporting information

BOLTZMANN-BGK Solver File System

Mesh generation

example.dat – geometry definition
example.bac – mesh spacing

PSPACEMESHGEN

Pre-processing

example.plt
mesh file

example.con
connectivity

METIS

example.npart
nodal partition

Solver

run.inp
contains filename
example.con
solver inputs
(conditions)
lobatto.inp
v-space quadrature

BGK

restart.res
If restarting

RESULTS1.RES contains ND, UVEL, VVEL
RESULTS2.RES contains RHO, PS, TEMP
RESIDUAL.RES residual output
RESTART.RES restart file
GIDMESH.RES plotting file for GID

Post-processing

ENGEN_BOLTZMANN

ENSIGHT visualisation files

3.12   References

(1) Thabet, S.; Thabit, T. H. Computational fluid dynamics: science of the future. *International Journal of Research and Engineering* **2018**, *5* (6), 430-433.

(2) Tang, W.; Advani, S. G. Drag on a nanotube in uniform liquid argon flow. *The Journal of chemical physics* **2006**, *125* (17), 174706.

(3) Amara, H.; Bichara, C. Modeling the growth of single-wall carbon nanotubes. *Single-Walled Carbon Nanotubes* **2019**, 1-23.

(4) Page, A. J.; Ohta, Y.; Irle, S.; Morokuma, K. Mechanisms of single-walled carbon nanotube nucleation, growth, and healing determined using QM/MD methods. *Accounts of chemical research* **2010**, *43* (10), 1375-1385.

(5) Zhu, Z.; Bai, Y.; Wei, N.; Gao, J.; Sun, S.; Zhang, C.; Wei, F. Controlled growth of crossed ultralong carbon nanotubes by gas flow. *Nano Research* **2020**, *13* (7), 1988-1995.

(6) Pieraccini, S.; Puppo, G. Implicit–explicit schemes for BGK kinetic equations. *Journal of Scientific Computing* **2007**, *32* (1), 1-28.

(7) Su, W.; Alexeenko, A. A.; Cai, G. A parallel Runge–Kutta discontinuous Galerkin solver for rarefied gas flows based on 2D Boltzmann kinetic equations. *Computers & Fluids* **2015**, *109*, 123-136.

(8) Evans, B. Nano-particle drag prediction at low Reynolds number using a direct Boltzmann–BGK solution approach. *Journal of Computational Physics* **2018**, *352*, 123-141.

(9) Kuznetsov, M. Analytical solution of the Boltzmann equation in a Knudsen layer. *Journal of Applied Mechanics and Technical Physics* **1971**, *12* (4), 604-607.

(10) Ho, M. T.; Zhu, L.; Wu, L.; Wang, P.; Guo, Z.; Li, Z.-H.; Zhang, Y. A multi-level parallel solver for rarefied gas flows in porous media. Computer Physics Communications 2019, 234, 14-25.

(11) Maxwell JC. On the dynamical theory of gases. InThe kinetic theory of gases: an anthology of classic papers with historical commentary, **2003**, 197-261

(12) Kandlikar, S. G.; Grande, W. J. Evolution of microchannel flow passages-- thermohydraulic performance and fabrication technology. *Heat transfer engineering* **2003**, *24* (1), 3-17.

(13) Lee, D.-T.; Schachter, B. J. Two algorithms for constructing a Delaunay triangulation. International Journal of Computer & Information Sciences 1980, 9 (3), 219-242.

(14) Evans, B.; Morgan, K.; Hassan, O. A discontinuous finite element solution of the Boltzmann kinetic equation in collisionless and BGK forms for macroscopic gas flows. *Applied Mathematical Modelling* **2011**, *35* (3), 996-1015.

(15) Karypis, G. METIS: Unstructured graph partitioning and sparse matrix ordering system. *Technical report* **1997**.

(16) Zhang, C., Pisana, S., Wirth, C. T., Parvez, A., Ducati, C., Hofmann, S., & Robertson, J. Growth of aligned millimeter-long carbon nanotube by chemical vapor deposition. *Diamondand Related Materials,* **2008** , 17 (7-10), 1447-1451

(17) Quinson, J., Bottein, T., Dillon, F., Shayan Meysami, S., & Grobert, N. Carbon nanotube columns for flow systems: influence of synthesis parameters. *Nanoscale Advances*, **2020**, 2(12), 5874–5882. https://doi.org/10.1039/D0NA00247J

(18) Huang, S.; Woodson, M.; Smalley, R.; Liu, J. Growth mechanism of oriented long single walled carbon nanotubes using "fast-heating" chemical vapor deposition process. Nano Letters **2004**, 4 (6), 1025-1028.

(19) Jin, Z.; Chu, H.; Wang, J.; Hong, J.; Tan, W.; Li, Y. Ultralow feeding gas flow guiding growth of large-scale horizontally aligned single-walled carbon nanotube arrays. Nano letters **2007**, 7 (7), 2073-2079.

(20) Jiang, Q.; Wang, F.; Li, R.; Wu, X.; Zhang, W.; Zhao, S.; Huang, Y.; Wang, B.; Zhang, S.; Zhao, Y. The Inherent Thermal Effect of Substrates on the Growth of Ultralong Carbon Nanotubes. Advanced Functional Materials 2022, 2212665.

(21) Hofmann, M.; Nezich, D.; Reina, A.; Kong, J. In-situ sample rotation as a tool to understand chemical vapor deposition growth of long aligned carbon nanotubes. Nano letters **2008**, 8 (12), 4122-4127.

Chapter 4

Physical preparation of CNT wires and presentations for impact

Sections of this chapter are reproduced with permission from:

(1) Orbaek White A, Hedayati A, Yick T, Gangoli VS, Niu Y, Lethbridge S, Tsampanakis I, Swan G, Pointeaux L, Crane A, Charles R, On the use of carbon cables from plastic solvent combinations of polystyrene and toluene in carbon nanotube synthesis; Nanomaterials; published by MDPI, 2021.

(2) Gangoli, V.S., Yick, T., Bian, F. and Orbaek White, A; From Waste Plastics to Carbon Nanotube Audio Cables; C; published by MDPI, 2022; at the end of the caption of the table, figure or scheme.

4.1   Carbon nanotube devices from plastics

Plastic waste has become an urgent topic in modern society and is a global environmental issue nowadays. A circular economy system would help ease plastic pollution. According to the data from Local Authority Municipal Waste Management, 2018 - 19 by the Welsh government [1], the recycling rate steadily from 62.7 % in 2017 - 18 increased to 62.8% in 2018 – 19. However, from another published data on waste collected for reuse, recycling or composting in Wales by material, the 2018 – 2019 report has shown that only 3% of plastic has been recycled or reused. It reported that plastic is the most neglected recycled waste among other categories like Inorganic (32 %) and paper & cardboard (8%), and most of the plastic waste would be sent to landfill. Plastics are made of high molecular weight polymers composed of various elements such as carbon, nitrogen, hydrogen, oxygen, chloride & sulphur[2]. An alternative method to upcycle and reuse plastic has started at the Energy Safety Research Institute (ESRI), Swansea University to turn waste plastic into high-value carbon products. This involves using the plastic waste as a carbon source to produce carbon nanotubes (CNTs).

The carbon nanotube (CNTs) powders were produced by the colleagues from Energy Safety Research Institute (ESRI) by a two-zoned horizontal liquid injection reactor (LIR) furnace[3], then the samples were used as received. In our recent published paper, the injection of 1 mL toluene (98% ($C_6H_5CH_3$), Sigma Aldrich, Gillingham, UK) is the main carbon source and at the speed of 5 mL/h, and a mixture of hydrogen/ argon (H_2/ Ar) (BOC, Guildford, UK)

in 5 vol % blended with the toluene in the furnace for carbon nanotubes growth. To make the plastic dissolution, which includes the shredded plastics which collected as received with heated toluene to dissolve plastics. Before the experiment, polystyrene $(C_8H_8)_n$ were dissolved in the organic toluene solution: in 1 – 4 wt % with the PS masses of 8.75, 17.5 & 35.0 mg accordingly. The final products were made into carbon nanotubes wire used in ethernet and audio cables, and we have previously displayed these devices at the National Waterfront Museum in Swansea and at the Welsh Government Office for Science for British Science Week at Cardiff. The carbon nanotube product is a promising material for future applications, replacing copper in the future[4]. In this work, the carbon nanotubes made from polystyrene (PS) have been demonstrated for waste plastic recycling. More plastic types, such as the commercial black plastic such as polypropylene (PP), polyethylene (PE) and polyethylene terephthalate (PET) can be expanded in the future.

4.2   Testing and CNT cable making

The carbon nanotube cables are made from waste plastics that can be used for the transmission of electricity. The patent, "Cables and methods thereof" has been filed for the United States Patent Application (20210158995) for our carbon nanotube cable in 2021[5]. To make a carbon nanotube cable, the raw materials include carbon nanotube powders, heat shrink tubing, and copper cables. Firstly, the carbon nanotube powders were transferred by a spatula from the storage vials into shrink wrap and are packed in the interior volume until the powders firmly filled the shrink wrap. Then both ends were connected to partially stripped copper wires to have good contact and inserted with more black shrink wraps at both ends that were then tightened and secured using a heat gun. The two ends were connected to a digital multi-meter and tested to be electrically conductive.

The buckypapers are formed from fragments of carbon nanotubes in a circular shape on a membrane by filtering CNT solution and they are highly conductive[6]. Similarly, the buckypaper thin film can be manufactured by folding and overlapping the individual buckypapers. The weight of the carbon nanotubes here was 0.03 g compared to the same length of copper cable at 0.21 g. It shows the CNT cables weigh 1/7th that of the copper cable for the equivalent sections, thus making use of the lightweight nature of the carbon nanotubes.

Figure 4.1. Carbon nanotubes ethernet cable, from figure 6. Photograph showing the CNT ethernet cable made using polystyrene-toluene feedstock (A), Orbaek White A, Hedayati A, Yick T, Gangoli VS, Niu Y, Lethbridge S, Tsampanakis I, Swan G, Pointeaux L, Crane A, Charles R. On the use of carbon cables from plastic solvent combinations of polystyrene and toluene in carbon nanotube synthesis. Nanomaterials. 2021 Dec 21;12(1):9.
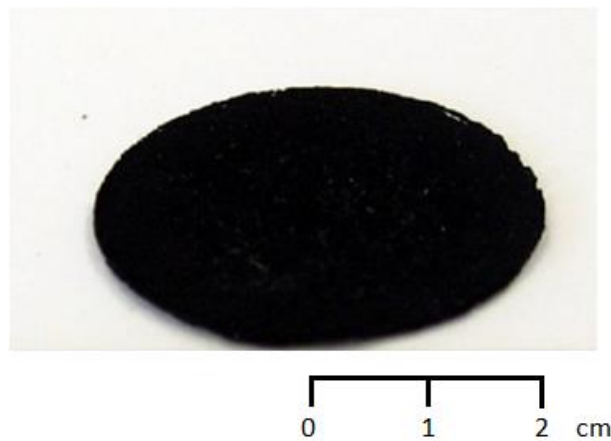
Figure 4.2. Image of a carbon nanotube buckypaper

The patent application of "cables and methods thereof" (Orbaek White, A and Yick, T) outlined the procedure for making carbon nanotube cables in a large industrial scale[5]. The work includes the method of inserting carbon-based nanomaterials into a heat-shrink material. The advantages of using carbon nanotubes as electric cables, for example instead of optical fibres is that the optical fibres are made from quartz or glass materials are fragile and prone to break and be bent under an external force. Carbon nanotubes are flexible and are ideal material for cable making due to their excellent mechanical strength and electrical. The diagram (figure 4.3) represents the illustration of constructing a carbon nanotube cable, by compressing the first part of sheet onto a second part of the sheet as one embodiment in s large-scale production line.

Figure 4.3. diagram of the assembly carbon nanotube cable[5]

100 – Conveyor (An apparatus)

102 - Configured to receive a heat-shrink material source (Conveyor)

104 - Heat-shrink material sources

106 - Compress the heat-shrink materials into a sheet; stable spool (extruder) – spool

108 - Conductive material sources

110 - Compressor – or hot-pressed rolls/ heat gun to become a closed-ended sheath

112 - Heat source

114 - Sheath cutter

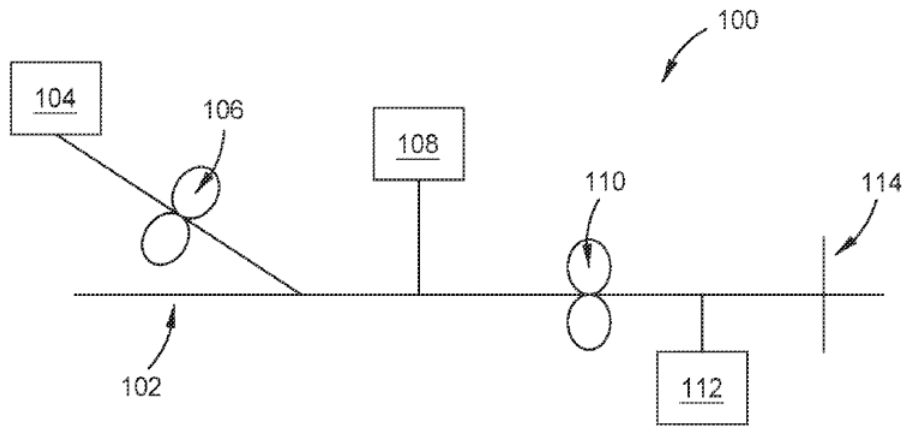The above schematic diagram illustrates a continues industrial manufacturing process of carbon nanotube cable production in an industrial scale. The apparatus (100) presents the assembly line of the carbon nanotube production. The feeding of the heat-shrink material (104) was transferred by the conveyor (106) which has a concave shape (V-shape or U-shape). This can be the includes a spool (104) in between which compress the heat-shrink material in shape. The conductive material sources (108) indicate the deposition of conductive materials onto the heat-shrink material. The compressor (110) is then compressing the sheet to form a closed-ended sheet as a sheath with low pressure. A low-pressure compression (0.1 to 1 N) can maintain the overall integrity of the conductive materials structure. The weight percentage of 75 wt % - 100 wt% of the conductive materials were filled into the interior volume of the sheath. The heat source (112) in the temperature range of between 50 - 200 °C, promotes the shrinkage of sheath around the conductive materials, which further provides conductivity into the cable.

The sheath cutter (114) is used to separate the filled material sheaths be individual cable with a suitable length. Above shown the rapid low-cost production of carbon nanotubes, which can be used for the mass production. The initial testing demonstration for the potential applications of the carbon nanotubes cables as below and will be discussed in the below individual section:

1) RJ45 plug – speeds testing for ethernet cables

2) 3.5 mm headphone jack – signals transmission to sounds

The components for making Ethernet cables include retail RJ45 connectors, electric terminals and shrink wrap filled with carbon nanotubes and copper contacts. There are eight pins for various purposes (transmit +, transmit -, received +, received -, and the rest unused). A simple method of improving the conductivity of carbon nanotubes has been mentioned by using a coffee grinder to increase the contact area by refining finer particles[7]. If the large flaky pieces were found from the deposition on inner wall of quartz tube, using a plastic bag to break them into smaller particles can prevent carbon nanotube dusts formation followed by using a mortar and pestle to create finer powders to pack into the heat shrink. Both ends of copper wires were stripped into 1 cm to attach the cables into the terminal blocks and to the sockets inside the RJ45 terminals (RS Components, Corby, UK). A crimp was used to clip all the wires into the RJ45 socket.

In the collaboration work, the ethernet cables were tested by a network speed test software, iPerf3 (ESnet/ Lawrence Berkeley National Laboratory, USA) which connected to two computers. The transfer speeds were measured from the server and ten runs were performed to ensure accuracy, which conducted by Gangoli VS. There were three types of Ethernet cable devices used: (I) category 6 cable (CAT 6), (II) copper cable, (III) carbon nanotube (CNT) cables in testing. The uplink speed (Mbps) & downlink speed (Mbps) were measured and shown in table 4.1. The carbon nanotube cables were measured to have a maximum uplink speed of 94.9 Mbps and a maximum downlink speed of 97 Mbps compared to the same parameters of 92.7 Mbps (maximum uplink speed) and 94.7 Mbps (maximum downlink speed) for the copper cable from the paper. The tested CNT cable was shown to meet the speed of CAT 5 standard owing to the ~100 Mbps maximum uplink & downlink speed[8]. Therefore, it exceeds the requirements of UK Government regulator for adoption and broadband classification[9]. The goal of this project is to create a CNT Ethernet cable that meets the CAT 6 standard speed of 1,000 Mbps[10], which has the maximum uplink speed (998 Mbps) & maximum downlink speed (995 Mbps) as tested for the CAT 6 cable.

Table 4.1. The uplink speed and downlink speed for the CAT 6, Copper & CNT cable, from Figure 6. the ethernet speed results using three devices, one (Cat6) commercial device and two lab made devices using CNTs or CU wire as active transmission component (B), Orbaek White A, Hedayati A, Yick T, Gangoli VS, Niu Y, Lethbridge S, Tsampanakis I, Swan G, Pointeaux L, Crane A, Charles R. On the use of carbon cables from plastic solvent combinations of polystyrene and toluene in carbon nanotube synthesis. Nanomaterials. 2021 Dec 21;12(1):9.

	Maximum uplink speed (Mbps)	Maximum downlink speed (Mbps)
CAT 6 cable	998	995
Copper cable	92.7	94.7
CNT cable	94.9	97

Polystyrene CNT cables were also demonstrated for the audio cables for sound transmission[11], in addition to the hybrid CNT-copper ethernet cable that was shown the ability of data transmission in the previous section. Using the same carbon nanotube cables, the cables were extended from the terminal blocked from both ends, attached to the commercial three-pole 3.5 mm stereo jack plugs (RS components, Corby, UK), and be plugged into a speaker or headphones in this study. In the experimental part, the CNT-Cu audio cables were attached to the HiFiMAN Arya headphone (HiFiMAN Electronics, Tianjin, China) and a pair of occluded ear simulators (IEC711) with a frequency measurement sensor used for measuring the frequency response of the headphone. The CNT-Cu audio cable was tested along with the commercial Cu cable for measurement. In figure 4.4, the logarithmic scale diagram shows that the CNT-Cu was closely matched to the commercial headphone cable as a headphone cable in frequency hearing range for humans, from 20 to 20 kHz[12].
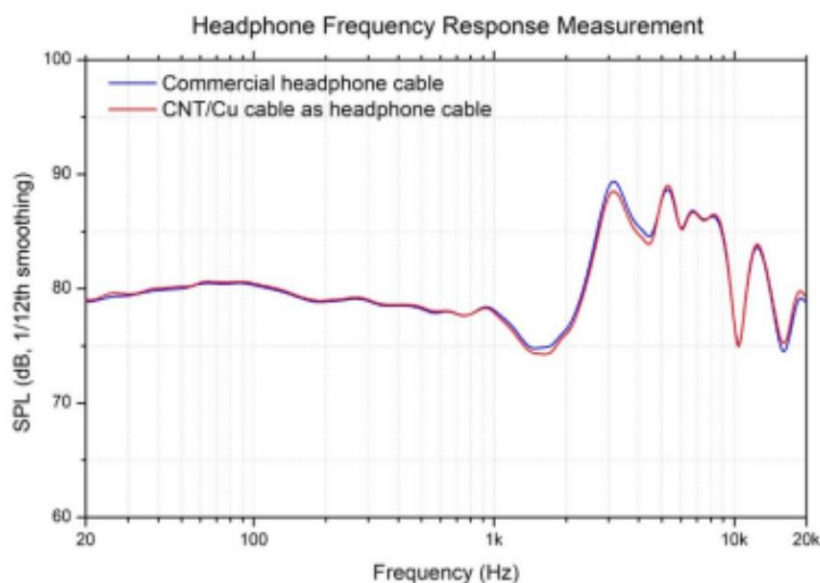
Figure 4.4. Frequency response for commercial headphone cable & CNT-Cu cable as headphone cable, from Figure 6. The frequency response of the HiFiMAN Arya headphones (right channel, averaged over three measurements) using a commercial headphone cable compared to the CNT/Cu cable as the headphone cable. Both are within error margins once the volume is matched, Gangoli VS, Yick T, Bian F, Orbaek White A. From Waste Plastics to Carbon Nanotube Audio Cables. C. 2022 Jan 25;8(1):9.

4.3   Welsh Government showcase & Welsh Circular Economy fund

A poster presentation was held at the Welsh government office for science for the British Science Week events in March 2020 and the academic poster was titled "How the plastic waste would change the well-being future generation act". The demonstration has shown that music can play through a carbon nanotube device whereby an audio speaker was connected using carbon nanotube cables (figure 4.5).

The Well-being of Future Generations (Wales) Act 2015 is a law that requires public bodies to think about the impacts on long-term decisions[13]. The generation act has highlighted 7 elements, (1) a prosperous Wales, (2) a resilient Wales, (3) a healthier Wales, (4) a more equal Wales, (5) a Wales of more cohesive communities, (6) a Wales of vibrant culture and thriving Welsh language & (7) a globally responsible Wales. The research aims to imply the future generation act, such as "a healthier Wales" and "a globally responsible Wales". For sustainable materials used, such as waste plastics to carbon nanotubes, prevent plastics entering into landfills and oceans that may potentially become microplastics. This circular economy

model provides an illustration of the renewal of materials in a closed loop, and the explanation of a circular economy: there are seven key elements in the cycle which include raw materials, design, production, distribution, consumption, collection, and recycling[14]. Taking our project from plastic to carbon nanotube as an example, the raw plastics were made and turned into consumer products such as plastic films and single use plastic bags. These plastic wastes are recycled and collected. At this point, the collected plastics can be transformed into carbon nanotubes and be other useful products, which benefits businesses, society, and the environment.

Figure 4.5. Carbon nanotubes audio cable display of the Welsh Government building on 13th March 2020

4.4 Waterfront Museum display (Carbon nanotubes cables)

A public engagement exhibition "from Bin to Bulb" was held at the National Waterfront Museum from October 2019 to June 2020. It is part of a public engagement event which explores innovation and science in Wales. Based on the statistical data from plastic recycling in UK 2021[15], over two million metric tons of plastic waste are produced each year and around 34 kg produced by each person in the UK. There was only 43.8% of plastic be recycled in 2021. Our recent work has demonstrated the recovery of plastic wastes to carbon nanotubes using polystyrene (PS)[3]. Previously, an outreach activity for the hydrogen bike exhibition from the Dunhill group at the Energy Safety Research Institute (ESRI) has shown a successful impact of public engagement [16]. The interactive display here included lightbulbs with buttons made from different materials, highlighting the carbon nanotube cable is conductive without the need for metal. Alongside the interactive display, a screen played the video "Plastic to carbon

nanotube" and briefly narrated the method for making carbon nanotube using the chemical vapour deposition (CVD) process. A poster was placed near the interactive device and the screen which contained a few paragraphs describing the process of turning the waste plastics into other useful carbon materials such as carbon nanotubes, graphene, and carbon fibre, thus showing that the project could save the country 8% of its total energy production. A large diagram at the centre of the poster described that the black plastics were chemically recycled and that carbon materials helped light up a bulb. The bilingual English and Welsh labels and breadboard jumper wires are connected to corresponding ports for buttons and bulbs for both English and Welsh speakers. Two instructions were titled "From Bin to Bulb" and "The carbon nanotubes act as electrical components without the need for metal. Try turning the light on and off to see how well it works.". There are a few goals for this project including (1) to inform the general public about the latest scientific discoveries, (2) manufacture an interactive device that shows the carbon nanotube cables from our lab which can tried on in a public space, and (3) to promote the thinking that plastic waste can be transformed into useful products such as carbon nanotubes for various applications. The targeted audience includes school pupils, the general youth, and family members.

A Raspberry Pi 4 Model B with four electric wires (copper, carbon nanotubes, nickel & plastic) with terminal blocks connected to lightbulbs and buttons were connected to a 5 V DC power source. All the parts were soldered on breadboards. The GPIO with outputs had another three questions with sets of Yes/ No buttons. The entire assembly was protected with acrylic plastic that was transparent to help show the components inside. A programmed Raspberry Pi computer recorded the date & time, and how many times each button was pressed. These were the corresponding questions to the buttons:

(1) Were you aware just 40% of the collected plastics is typically recycled?
(2) Were you aware that plastic could be chemically recycled into electricity cables before seeing this exhibit?
(3) Now that you've seen this exhibit, are you interested to learn more about chemical recycling of plastics?
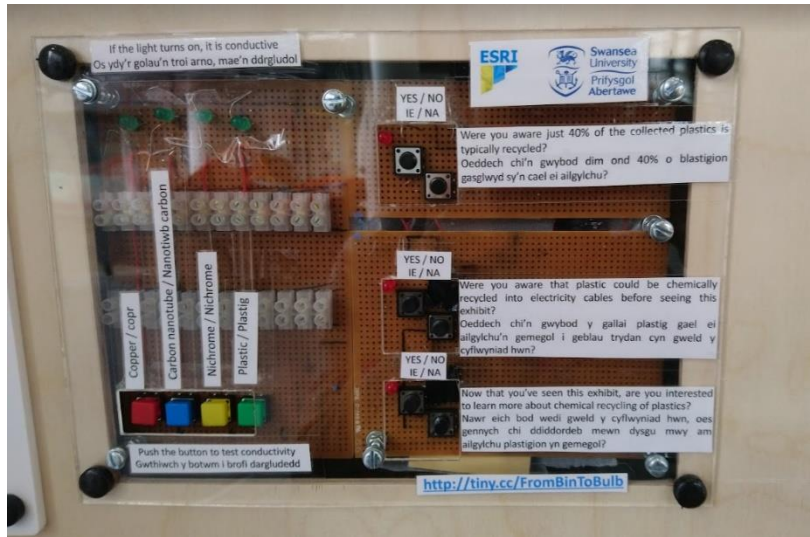
Figure 4.6. Carbon nanotubes power cables display of the Swansea National Waterfront Museum

Figure 4.7. Display at the National Waterfront Museum

The device had been pressed 4,858 times in total with peaks in mid-October (325 times per day) and mid-January (340 times per day). After the post-processing of the data, we concluded that there were 664 respondents who participated and 72,000 total visitors during that time. From the results, the plastics (474 times, 33.5%), nickel (83 times, 5.9%), carbon nanotubes (403 times, 28.5%), copper (455 times, 32.2%) being pressed are seen in figure 4.8.

Figure 4.8. The percentage of different cables (plastic, nickel, carbon nanotubes & copper) pressed

Table 4.2. The distributions of Question 1 (Were you aware just 40% of the collected plastics is typically recycled?), Question 2 (Were you aware that plastic could be chemically recycled into electricity cables before seeing this exhibit?) & Question 3 (Now that you've seen this exhibit, are you interested to learn more about chemical recycling of plastics?)
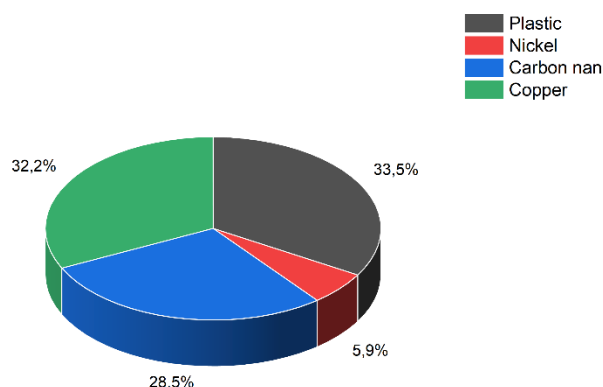
Questions	Number of respondents
Q1-Yes	120 (31.4 %)
Q1 - No	262 (68.6 %)
Q2 -Yes	203 (46.7 %)
Q2 - No	232 (53.3 %)
Q3 -Yes	250 (58.5 %)
Q3 - No	177 (41.5 %)

More than two-thirds of the respondents stated that they were unaware that just 40% of the collected plastics are typically recycled. 53.3 % of the respondents stated that they were unaware that plastic could be chemically recycled into electricity cables before seeing this exhibit. Slightly less than half of the people (46.7%) responded that they knew. More than half of the respondents (58.4 %) responded that they would be interested in learning more about plastics' chemical recycling.

4.5   Results

We have demonstrated that plastic waste can successfully be converted to carbon nanotubes. It is making a positive impact on society and bringing awareness to plastic waste

and the use of nanotechnology. Carbon nanotubes can replace copper in terms of weight and thermal resistance and carry more electricity over the same mass of copper wire. Due to the impacts of COVID-19, the exhibition was closed for visits due to a lockdown. The data was mostly recorded from October 2019 to March 2020 for 6 months, and the data after these months were absent. Given the timeframe and the smaller scale of visitors, the study may not fully reflect the visitors' awareness of plastic recycling into carbon nanotubes. Although the museum data has shown that copper and plastic has more popularity among the visitors, the subsequent material of interest is the carbon nanotube cable. From the data, we can see that people were unaware just 40% of the collected plastics are typically recycled. More than half of the respondents would like to learn more about chemical recycling. They are aware of the plastic pollution problems and do not know about the low recycling rate. This suggests that the exhibition has made a strong, positive impact on the awareness of chemical recycling and environmental impacts from plastic waste.

For the economic and societal impacts, this exhibition has undoubtedly increased the awareness of plastic wastes and the future development of nanotechnology as part of public engagement events. Also, this project provides a significant impact on environmental sustainability, improving health and well-being in the society by removing the waste plastic from the environment, and turn them into useful materials such as carbon nanotubes as a long-term solution. Finally, the project influences the public policies and informs the policy makers of where research funding is to be allocated. Indeed, this project has been awarded the Circular Economy fund from the Welsh government in 2020, which indicates that the policy makers understand this project could positively improve our society.

4.6   Conclusion and future work

The evidence from our research has suggested that the carbon nanotube ethernet cable and audio cable have outstanding performance, which have proved that the CNTs can be used for electricity transmission. The CNT Ethernet cable has an uplink and downlink speed of ~99 Mbps. The audio cable has shown the same audio frequency response as the commercial audio cables. These data are encouraging as they indicate the potential applications and improvement of the carbon nanotube cables. As revealed in the published papers, these CNT cables were made from polystyrene plastic (PS). The public engagement events, such as the exhibition at waterfront museum of this one, can help the public understand that waste plastic can be

chemically recycled. We would like to make more such products using carbon nanotube cables, such as an audio device, for display at the Oriel Science exhibition in Swansea. The CNT products produced from waste plastics in the liquid injection CVD reactor have been generally short in length, and it is expected that the previous work on growing UL-CNTs would bring some insights on producing longer CNTs in bulk amounts.

4.7   References

(1) Local Authority Municipal Waste Management, 2018-19. *Welsh Government* **2019**.

(2) Perkins, S. *Explainer: What are polymers?* Science news for students, 2017. https://www.sciencenewsforstudents.org/article/explainer-what-are-polymers#:~:text=polymer%20A%20substance%20made%20from,make%20paper%2C%20for%20example). (accessed 12/6/2022).

(3) Orbaek White, A.; Hedayati, A.; Yick, T.; Gangoli, V. S.; Niu, Y.; Lethbridge, S.; Tsampanakis, I.; Swan, G.; Pointeaux, L.; Crane, A. On the use of carbon cables from plastic solvent combinations of polystyrene and toluene in carbon nanotube synthesis. *Nanomaterials* **2021**, *12* (1), 9.

(4) Zhang, S.; Nguyen, N.; Leonhardt, B.; Jolowsky, C.; Hao, A.; Park, J. G.; Liang, R. Carbon-nanotube-based electrical conductors: fabrication, optimization, and applications. *Advanced Electronic Materials* **2019**, *5* (6), 1800811.

(5) Yick, A. O. W. K. C. Cables and methods thereof. 2021.

(6) Endo, M.; Muramatsu, H.; Hayashi, T.; Kim, Y.; Terrones, M.; Dresselhaus, M. 'Buckypaper'from coaxial nanotubes. *Nature* **2005**, *433* (7025), 476-476.

(7) Kumanek, B.; Wasiak, T.; Stando, G.; Stando, P.; Łukowiec, D.; Janas, D. Simple method to improve electrical conductivity of films made from single-walled carbon nanotubes. *Nanomaterials* **2019**, *9* (8), 1113.

(8) Kavehrad, M.; Doherty, J. F.; Jeong, J.-H.; Roy, A.; Malhotra, G. 10 Gbps transmission over standard category-5 copper cable. In *GLOBECOM'03. IEEE Global Telecommunications Conference (IEEE Cat. No. 03CH37489)*, 2003; IEEE: Vol. 7, pp 4106-4110.

(9) Hutton, G. Gigabit-Broadband in the UK: Government Targets and Policy. *London: UK Parliament* **2021**, *30*.

(10) Azadet, K.; Yu, M.-L.; Larsson, P.; Inglis, D. A gigabit transceiver chip set for UTP CAT-6 cables in digital CMOS technology. In *2000 IEEE International Solid-State Circuits Conference. Digest of Technical Papers (Cat. No. 00CH37056)*, 2000; IEEE: pp 306-307.

(11) Gangoli, V. S.; Yick, T.; Bian, F.; Orbaek White, A. From Waste Plastics to Carbon Nanotube Audio Cables. *C* **2022**, *8* (1), 9.

(12) Self, D. *Audio engineering explained*; Routledge, 2012.

(13) Government, W. Well-being of future generations (Wales) act 2015. Welsh Government Cardiff: 2015.

(14) Geissdoerfer, M.; Pieroni, M. P.; Pigosso, D. C.; Soufani, K. Circular business models: A review. *Journal of Cleaner Production* **2020**, *277*, 123741.

(15) Government, W. *Local authority municipal waste management: July to September 2021*. https://gov.wales/local-authority-municipal-waste-management-july-september-2021 (accessed 17-8-2022).

(16) Glover, K.; Rudd, J. A.; Jones, D. R.; Forde, E.; Warwick, M. E.; Gannon, W. J.; Dunnill, C. W. The hydrogen bike: communicating the production and safety of green hydrogen. *Frontiers in Communication* **2021**, *5*, 540635.

Chapter 5

Concluding chapter and recommendations

This work has provided valuable experimental and theoretical resources towards understanding and controlling the growth of ultra-long carbon nanotubes (UL-CNTs). It has shown that a gas mixture of H_2/CH_4 in a 2:1 ratio at 950 °C with iron (III) chloride catalyst ($FeCl_3$) has been capable of growing UL-CNTs longer than a centimetre (cm). Moreover, this study has provided evidence that using DI-water over ethanol as a solvent can limit the spread of the catalyst on the silicon substrate, and this helps provide an optimal catalyst concentration for carbon nanotube growth across the substrate surface. The monometallic catalyst, iron, has produced the longest carbon nanotube (1.32 cm), followed by the bimetallic catalysts of iron-copper (Fe-Cu, 0.85 cm), iron-cobalt (Fe-Co, 0.7 cm), iron-nickel (Fe-Ni, 0.6 cm), iron-magnesium (Fe-Mg, 0.29 cm) & iron-aluminium (Fe-Al, 0.13 cm). In the simulation work of modelling gas flow exerts on carbon nanotube geometry, an average ratio of H_2/CH_4 with different flow rate scenarios (1, 10, 30, 100 & 1000 sccm) in three temperature settings (1123, 1223 & 1285 K) have been simulated. The results of this study indicate that a high flow rate is preferable than a low flow rate for ultra-long carbon nanotube growth. A faster flow rate provides a more uniform distribution pressure along both walls of the nanotube than at a low flow rate with inconsistent pressure distributions. In the final chapter, the carbon nanotube Ethernet and audio made from waste plastic have been introduced. The Ethernet cable has a remarkable uplink/ downlink speed of ~100 Mbps and the CNT audio cable matches the performance of commercial audio cables in the human audible range of 20 – 20,000 Hz. In addition, a previous exhibition at the National Waterfront Museum in Swansea has shown positive impact on the public awareness of the chemical recycling of waste plastics.

In the theoretical part of the project, the concentration of the DI-water catalyst solution should be low to produce long individual carbon nanotubes by reducing the CNT-CNT interactions when the nanotubes escape the catalyst droplet. The ratio of the bimetallic catalysts for the iron-based catalyst is also a factor affecting the activation rate of the carbon nanotubes, which may result in shorter carbon nanotubes for a 1:1 ratio of catalysts used in this work. Expanding to the other types of metallic catalysts such as iron-molybdenum (Fe-Mo) and varying the ratio of bi-metallic catalyst to iron, such as 2:1 or 3:1 ratio, may help define the best parameters to grow ultra-long carbon nanotubes and are recommended for future work.

The significant limitations of this study are the expenses incurred for the computational fluid simulations, and the study of microfluidics has remained in infancy. Due to the complexity and computational costs, this work has been limited to a 2-dimensional geometry. Also, it is assumed that the parameters of H_2/CH_4 are on the CNT average diameter, and the wall & domain temperature influences are in an isothermal environment by cause of the same reason. In the observation of SEM images, there are thousands of carbon nanotubes that may tangle together in experimentally grown samples. However, in this simulation study, only a single carbon nanotube on the substrate was simulated. Furthermore, in this project, a single and straightforward carbon nanotube geometry was set up in the simulation. The setup does provide a preliminary understanding of how fluid flow affects a single carbon nanotube growth, but there remains a barrier between the theoretical and experimental work. Also, the reality is that a nanotube is not rigid and has some form of flexibility on the growth structure. In this simulation, only two physical forces (mechanical and thermal) were explored. Another possible area of future research would be to investigate the chemical force, such as the catalytic reactions, all together with the additional multiple and three-dimensional carbon nanotubes geometry with two or more species of gases in the simulation that is only possible with increased computational resources. More practice work should be done to close the gap between computational modelling/theory and experimental results, such as performing physical experiments in different flow rates (1, 10, 30, 100 & 1000 sccm) with different temperatures (1123, 1223 & 1285 K), and comparing the results to computational parameters and simulations.

The CNT ethernet cables and audio cables have shown an outstanding performance in terms of the transmission speeds (uplink & downlink of ~100 Mbps) and the audio frequency response compared to commercial copper cables. Further research should be done to investigate the improvement of the transmission data rate from CAT 5 to CAT 6 standard (uplink speed ~998 Mbps & downlink speed ~995 Mbps). It might be possible to use some longer and more continuous/aligned carbon nanotube fibres to construct the ethernet cables with better electrical properties in the future.